Ultrafast ultrasound imaging for simultaneous extraction of flow and arterial wall motion with linear array probe

Vincent Perrot

To cite this version:

Vincent Perrot. Ultrafast ultrasound imaging for simultaneous extraction of flow and arterial wall motion with linear array probe. Medical Imaging. Université de Lyon, 2019. English. NNT : 2019LYSE1177 . tel-02447041

HAL Id: tel-02447041
https://theses.hal.science/tel-02447041
Submitted on 21 Jan 2020

N° d'ordre NNT : 2019LYSE1177

PhD Thesis of The Université de Lyon

prepared at
l'Université Claude Bernard Lyon 1

Doctoral school N° 162
MEGA
Mécanique - Energétique - Génie Civil - Acoustique
Doctoral speciality: Acoustics and signal/image processing

Publicly defended on October 23rd, 2019, by:

Vincent Perrot

Ultrafast Ultrasound Imaging for Simultaneous Extraction of Flow and Arterial Wall Motion with Linear Array Probe

---

In the presence of the jury composed of:

Patrick Clarysse	Research Director, CREATIS, CNRS, President
Jørgen Arendt Jensen	Professor, DTU Elektro, Reviewer
Adrian Basarab	Associate Professor, IRIT, UT3, Reviewer
Odile Bonnefous	Principal Scientist, Philips Research Paris, Examiner
Ingvild Kinn Ekroll	Researcher, ISB, NTNU, Examiner
Aline Bel-Brunon	Associate Professor, LaMCoS, INSA, Examiner
Anne Long	Professor-Hospital Practitioner, CREATIS, HCL, UCBL, Examiner
Hervé Liebgott	Professor, CREATIS, UCBL, Director
Didier Vray	Professor, CREATIS, INSA, Co-Director (invited)
Damien Garcia	Researcher, CREATIS, INSERM, Invited

Acknowledgments

My first thoughts go to Hervé and Didier, my supervisors. Including my internship before this thesis, it has been three and a half years under your supervision as well as working together. You have always been able to give me confidence, have listened to me, and have given me good advice. Also, you were there, even in stressful situations. No matter what happens, I would always remember you both on a personal and professional level.

My warmest thanks to Damien who, although he is not one of my supervisors, provided me with great advice and guidance. Thank you for all these discussions that have enormously contributed to my thesis.

I am very grateful to Lasse that made it possible for me to come to his lab in Norway. A significant part of this work has been possible thanks to this collaboration. Also, a special thanks to Ingvild and Jørgen who helped me during my stays, answered my questions, and always remained available.

A heartfelt thanks to my colleagues and friends from CREATIS: Maxime, Emeline, Nina, Valentin, Paolo, Matthieu, Tom, Goulven, Bingqing, Pei, and Sami. A special thanks to those who preceded me in the laboratory: Yanis, Sébastien, Aneline, Denis, and Emilia. Thank you all for making this experience even more enjoyable than I thought it would be; I was able to find colleagues, but also friends and confidants.

I cannot thank everyone, the list is too long; thanks to all those with whom I have worked and exchanged during this thesis.

Last but not least, a very special thanks, from the bottom of my heart to my family and friends whom I did not have much opportunity to see and visit during the very last years.

Abstract

This thesis is focused on ultrasound imaging for clinical applications. The main goal of this work is to provide clinicians an ultrasound mode to simultaneously extract wall motion and flow at high frame rates in arteries that can be imaged with a linear probe. Cardiovascular pathologies are a major cause of death and disability worldwide. Although the formation of such diseases is still not fully understood, it appears that some parameters, related to flow velocity and wall motion during the cardiac cycle, could be markers of some pathologies and allow for their early detection. Because tissues are subject to fast and complex phenomena in the arteries, a high frame rate modality seems highly relevant to extract as much information as possible on the condition of the cardiovascular system. Unfortunately, no technique is currently clinically used or even approved for the extraction of both flow and wall pathological markers at high frame rates. Therefore, in this thesis, I propose to design an ultrasound sequence and algorithm permitting to extract both aspects, at high frame rates on arteries, for a potential clinical application.

There are three main scientific contributions in this thesis: *i*) the design of the ultrasound sequence with a 2D motion estimator, *ii*) a new adaptive clutter filtering approach, and *iii*) a clinical proof of concept.

The ultrasound sequence is based on plane wave acquisition permitting to yield frame rates up to 10 000 images per second in the carotid. The pipeline used an approach introducing a virtual lateral oscillation in ultrasound imaging which, coupled with a 2D phase-based estimator, allows to extract vectorial velocity fields. Validations for both flow and wall motion estimation were performed on a commercial Doppler flow phantom and an in-house realistic carotid phantom designed for the experiments. The adaptive clutter filtering was developed and validated on volunteers based on tissue estimates, which permit to precisely remove tissue clutter from flow signals. Finally, the clinical proof of concept was performed at the hospital with a group of volunteers and a group of patients.

The ultrasound sequence, motion estimation algorithm, and adaptive clutter filtering approaches have been validated in the thesis. The method can provide both wall motion and flow estimates at high frame rates, with low errors and standard deviations. Indeed, errors are typically lower than 10% on magnitudes and less than 10 degrees on angles. The adaptive clutter filtering approach permits to better extract the flow compared to other standard approaches. This improvement is especially noticeable close to the wall, which would allow accurate flow and wall shear rate (representing the stress) measurements along arterial walls where plaques can form and develop. To conclude, the clinical proof of concept has demonstrated the feasibility in a clinical environment with the extraction of wall motion, flow, and arterial parameters that showed differences between and within groups. This thesis is a step toward clinical use of high frame rate ultrasound imaging for quantification of both wall motion and flow in patients with cardiovascular pathologies.

Contents

List of Figures

List of Tables

List of Abbreviations

1D	One-Dimensional
2D	Two-Dimensional
AIC	Akaike Information Criterion
BIC	Bayesian Information Criterion
CCA	Common Carotid Artery
CFD	Computational Fluid Dynamics
CW	Continuous Wave (Doppler)
DAS	Delay-And-Sum
ECA	External Carotid Artery
ECG	ElectroCardioGram
EDV	End-Diastolic Velocity
EVD	EigenValue Decomposition
FFT	Fast Fourier transform
FIR	Finite Impulse Response
FWHM	Full Width at Half Maximum
ICA	Internal Carotid Artery
IIR	Infinite Impulse Response
MI	Mechanical Index
NCC	Normalized Cross-Correlation
PIV	Particle Image Velocimetry
PRF	Pulse Repetition Frequency
PSF	Point Spread Function
PSV	Peak Systolic Velocity
PVA	PolyVinyl Alcohol
PW	Pulsed Wave (Doppler)
PWV	Pulse Wave Velocity
SNR	Signal-to-Noise Ratio
SVD	Singular Value Decomposition
TGC	Time Gain Compensation
TI	Thermal Index
TO	Transverse Oscillation

WSR	Wall Shear Rate
WSS	Wall Shear Stress

Outline

The first chapter is a general background acting as an introduction to the thesis. The overall cardiovascular system is described with the anatomy of the heart and arteries. Therefore, the possible arterial disorders are listed with their consequences on the health of the patient and potential clinical complications. Ultrasound imaging is then briefly introduced with the clinical context, and the principle of this imaging modality is described. The standard focused imaging is compared to ultrafast plane wave imaging, and the image formation permitting to get exploitable images from received signals is then briefly introduced. Then different markers of cardiovascular diseases that can be calculated from flow and wall motion are presented along with their use in clinical practice. The first chapter concludes with the importance and potential applications of the simultaneous assessment of flow and wall characteristics.

The second chapter is an overview of the standard motion estimation techniques presenting the techniques that are commonly used in vascular ultrasound imaging. The Doppler-based techniques are first described, starting with a described chronological timeline of Doppler ultrasound. Therefore, both frequency-based and phase-based approaches are presented. Then, non-Doppler-based techniques are described, including the so-called speckle-tracking and optical flow approaches. After presenting the standard techniques, state of the art of the specific subject of simultaneous measurement of tissue movement and flow is conducted. This state of the art includes previous works from several groups around the world in the last 20 years. The second chapter concludes with the goals and the selected approach during the thesis for the simultaneous measurement.

The third chapter is the description of the methodology for the simultaneous measurement of flow and tissue motion at high frame rates. Transverse oscillation, which is the main technique used in the thesis, is first described. Then, two different approaches are described for the implementation of the technique. The first one is a time-domain approach which is common in the literature and, the second one is a Fourier filtering approach used in the thesis. A 2D phase-based estimator for assessment of motion, slightly different from classical estimators and adapted to our approach, is then reported. The pipeline of the algorithm is presented and described step by step, including image acquisition and beamforming, tissue motion estimation, and flow estimation. Then, advanced parameters used for validation of the methods are listed and explained. After this methodological part, the estimator is validated based on *in vitro* experiments. A first validation is performed on a commercial flow phantom with a research scanner, and a second validation is done on an in-house tissue and flow phantom specifically created for the validation. The third chapter concludes with a discussion on the *in vitro* experiments and the limits for an application on *in vivo* carotids.

The fourth chapter is the description of the methodology for adaptive clutter filtering techniques that are based on the tissue velocity estimates. First, clutter filtering is introduced with a description of clutter and flow signals. Conventional convolution-based filters (finite and infinite impulse responses) are depicted with regression-based (polynomial), and eigen-based filters (principal component analysis and singular value decomposition); automatic data-driven clutter filters are also described. After listing the standard categories of filters, the motivations for a clutter filtering technique based on tissue estimates are reported. Then, the conventional approaches for comparison are described with details on the temporal adaptive and spatial and temporal adaptive clutter filtering methods. Finally, *in vivo* experiments are reported on volunteers with the description of the material and methods, presentation of the results, and a comparison with a data-driven approach based on singular value decomposition. The fourth chapter concludes with the potential application of adaptive clutter filtering in clinical practice.

The fifth and last chapter is a step towards clinical use of the simultaneous tissue and flow measurements, which is a clinical proof of concept on carotids with both healthy volunteers and patients. Material and methods are first described, patient and volunteer populations are presented with the corresponding approach for tissue motion and flow estimation; however, the majority of the methods are depicted in the previous chapters. Then, the metrics extracted during the clinical proof of concept are detailed. Finally, results are reported through qualitative inspection, values of the metrics, and a presentation of an additional case, which is internal carotid stenosis. The chapter concludes with the limitation, opportunities, and future works to go further in clinical usability.

Chapter 1

General Background

The first chapter is a general background acting as an introduction to the thesis. The overall cardiovascular system is described with the anatomy of the heart and arteries. Therefore, the possible arterial disorders are listed with their consequences on the health of the patient and potential clinical complications. Ultrasound imaging is then briefly introduced with the clinical context, and the principles of this imaging modality are described. The standard focused imaging is compared to ultrafast plane wave imaging, and the image formation permitting to get exploitable images from received signals is then explained. After introducing both the medical aspect and ultrasound imaging modality, the pathological markers for both wall and flow and their potential clinical utilities are described. The first chapter concludes with the importance and the potential applications of the simultaneous assessment of flow and wall characteristics.

There is no scientific contribution in this chapter, which is based on a medical literature review and several meetings and discussions with clinicians.

1.1 Cardiovascular system

The first section of the first chapter presents the cardiovascular system. This section is broken down into three subsections: heart, arteries, and arterial disorders. In the following, the inner structure and functioning of the cardiovascular system are described with the effects of arterial disorders on health.

1.1.1 Heart

The heart is the central organ of the cardiovascular system localized in the middle of the upper chest between the lungs. It is in charge of blood distribution to provide oxygen and nutrients to the body, but also to transport metabolic wastes

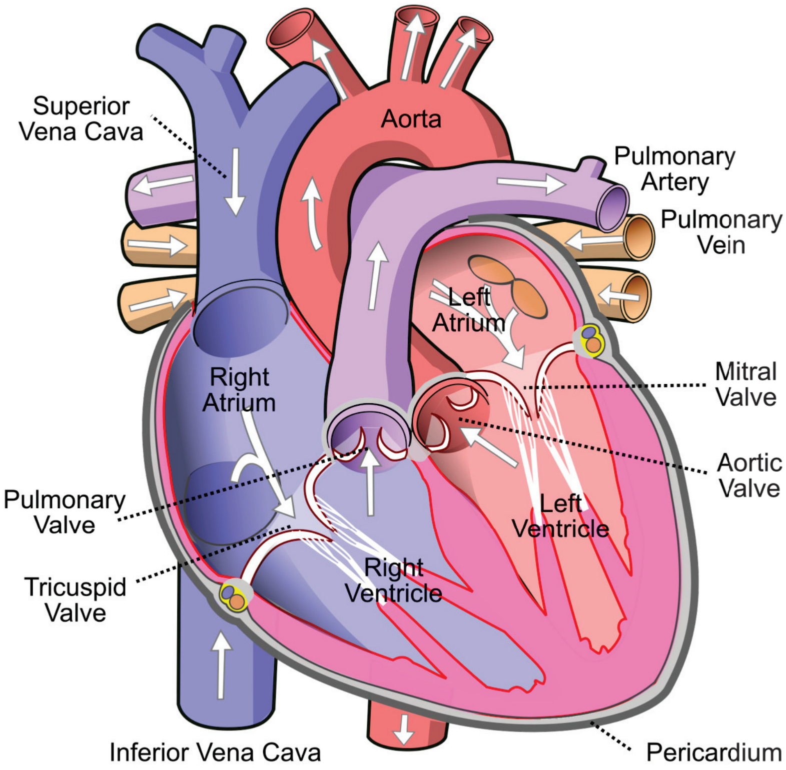

Figure 1.1: Diagram of the human heart. The image depicts the different cavities and the overall structure of the heart, which permits to ensure its function. [*Diagram of the human heart, Wikimedia Commons - Wapcaplet, CC BY-SA*].

for evacuation. A typical adult heart is cone-shaped, with its base positioned upwards. It weighs about 250 grams with a typical size of 12 centimeters in length, 8 centimeters in width, and 6 centimeters in thickness [1]. The heart has four intern chambers, two atria through which blood enters the heart, and two lower ventricles, which collect and eject blood received from the atria [1].

With its action, deoxygenated blood is sent to the lungs, then pumped back into the heart to be distributed into all the body through the arteries. This important, but complex action, can be accomplished through its internal structure (Fig. 1.1). The human heart is composed of the right and left atria in charge of pumping the blood through the vena cava and pulmonary vein, respectively. The right and left ventricles are separated from the atria by the tricuspid and mitral valves, respectively. The right ventricle sends the blood to the pulmonary artery after the opening of the pulmonary valve, while the left ventricle sends it to the aorta through the aortic valve. The myocardium (heart muscle) is wrapped by the pericardium, composed of several layers, facilitating its contraction and containing several vessel roots. The tricuspid and mitral valves (separating the atria from the ventricles) are named atrioventricular valves while the pulmonary and aortic valves (separating the ventricles from the arteries) are named semilunar valves. This inner structure permits the completion of the cardiac cycle, repeating itself over time, that can be roughly divided into four steps (Fig. 1.2) with the systolic phases (contraction) and diastolic phases (relaxation) [2]:

a. **Atrial diastole** (Fig. 1.2a): Relaxation and filling with the deoxygenated blood coming from the vena cava and the oxygenated blood from the pulmonary vein, all the valves are closed.

b. **Ventricular diastole** (Fig. 1.2b): Blood is passively transferred into the ventricles, the atrioventricular valves are opened.

c. **Atrial systole** (Fig. 1.2c): Both atria contract and force the blood from the atria to the ventricles, the atrioventricular valves are opened.

d. **Ventricular systole** (Fig. 1.2d): Both ventricles contract and force the deoxygenated blood to the pulmonary artery and the oxygenated blood to the aorta, the semilunar valves are opened.

This four-step cycle is repeated over time to oxygenate the blood and distribute it to the organs continuously. The rhythm of the heart is determined by an electric signal, propagating in the heart, given by a group of pacemaking cells; for a healthy heart, this current generates the contraction of the myocardium and control the cardiac cycles at a given frequency, depending on the body's nutrient needs.

The movements of the cardiac muscles and phases of the heart have unquestionably an influence on the flow pattern in the lumen of the arteries, but also on the movement of the arterial wall. Indeed, arteries are connected to the heart, directly or indirectly through the aorta, and should reflect cardiac cycles [3].

1.1.2 Arteries

The heart is the central point of a complex and widespread circulatory system (Fig. 1.3a). In this system, the arteries are in charge of transporting blood from the heart to all the other organs. The main artery is the aorta, directly connected to the heart to which both left and right carotid arteries are connected. The carotid artery is often imaged and studied in ultrasound because it is superficial and therefore easily accessible for clinical research. Moreover, it is still an information source on the overall cardiovascular health, as it is relatively close to the heart, and as a part of the cardiovascular system.

Carotid artery (Fig. 1.3b) is a general word. In reality, the main artery in each side

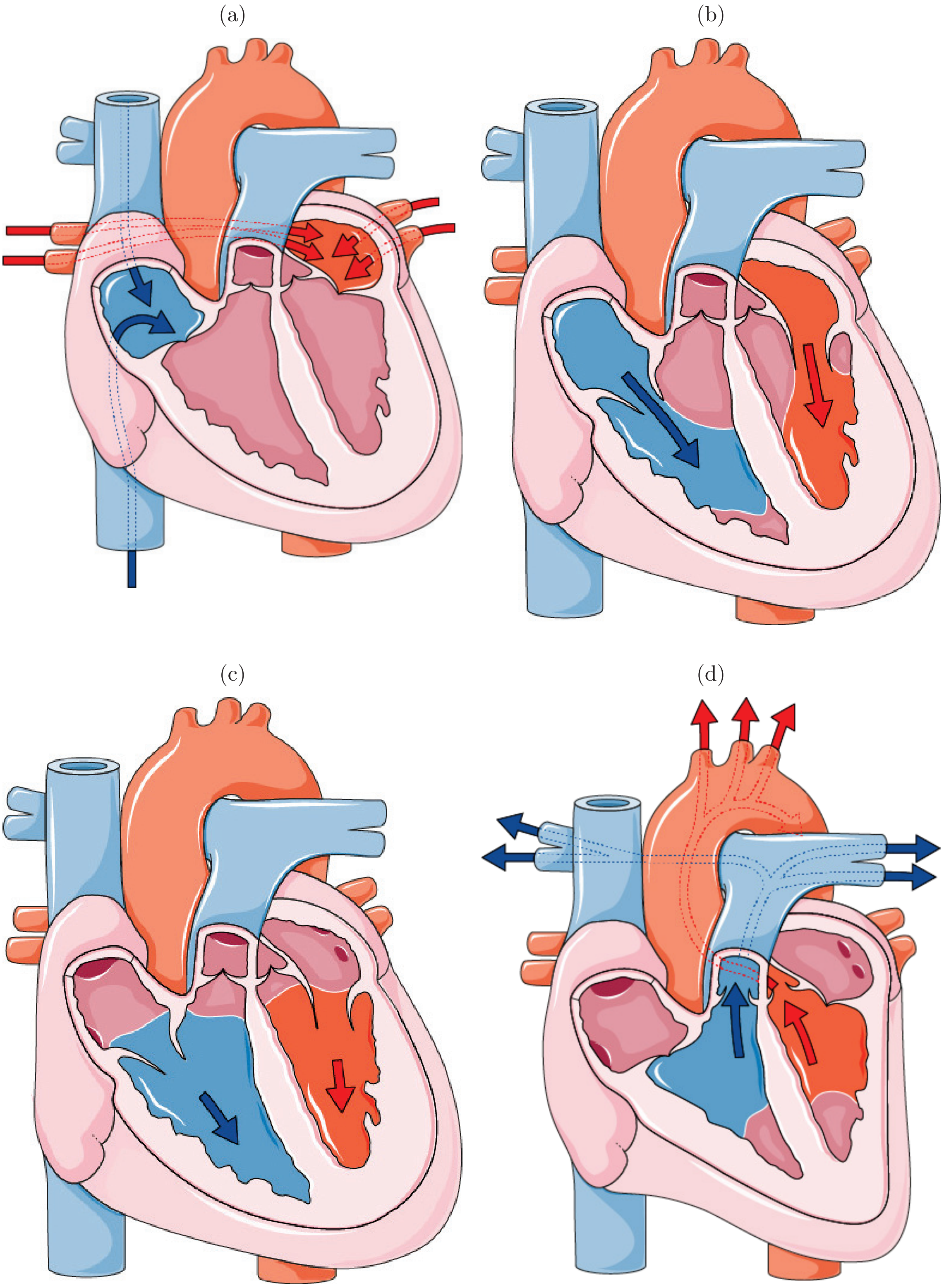

Figure 1.2: Diagram of the cardiac cycle in four steps: (a) atrial diastole, (b) ventricular diastole, (c) atrial systole, and (d) ventricular systole. [(a)-(d): *The cardiac cycle, Servier Medical Art, CC BY*].

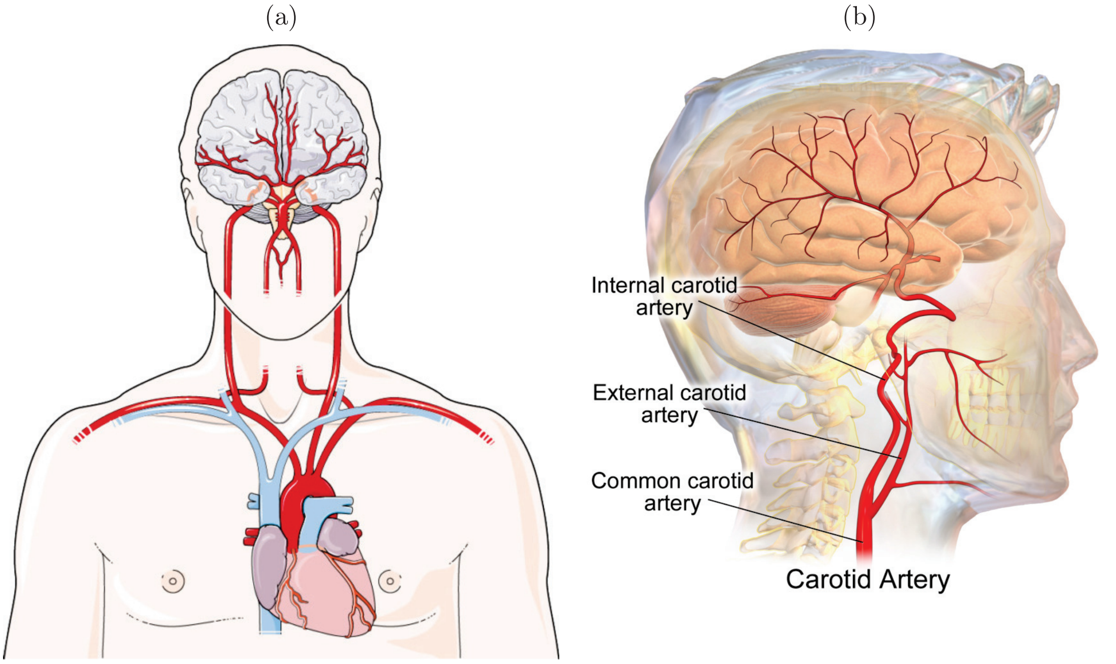

Figure 1.3: Upper circulatory system: (a) the heart with the main upper vessels, and (b) the common carotid artery and its main branches. [(a): *Brain arteries, Servier Medical Art, CC BY*], [(b): *Carotid, Wikimedia Commons - BruceBlaus, CC BY*].

of the neck is the common carotid artery (CCA) starting directly from the aorta for the left CCA and connected to the brachiocephalic artery which is connected to the aorta for the right CCA. Then, each CCA splits into the external carotid artery (ECA) irrigating the superficial tissues of the face, and the internal carotid artery (ICA) that oxygenates the brain. Arteries are vessels carrying blood away from the heart (except for the pulmonary and umbilical arteries) toward the organs. Often, arteries are described as tubes (Fig. 1.4), at the macroscopic level, composed of several layers (Fig. 1.5) [4]. Those layers ensure the different functions of the arteries [4]. The external layer of the artery, which is rigid compared to the others

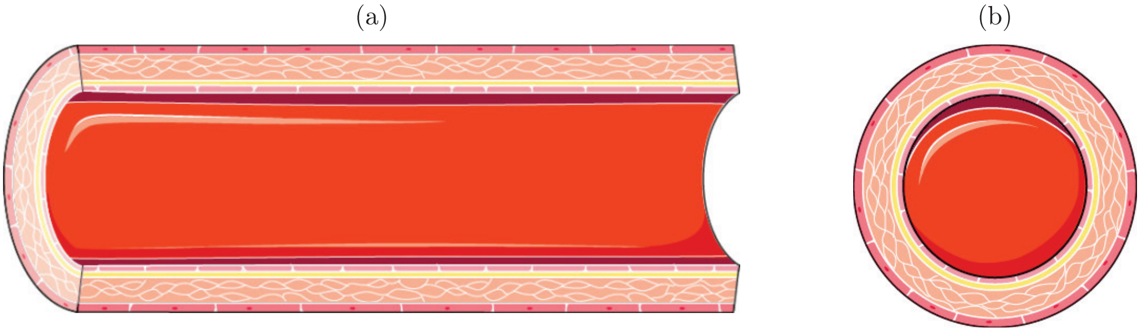

Figure 1.4: Diagrams of an artery: (a) longitudinal, and (b) axial views of an artery. [(a)-(b): *Arteries, Servier Medical Art, CC BY*].

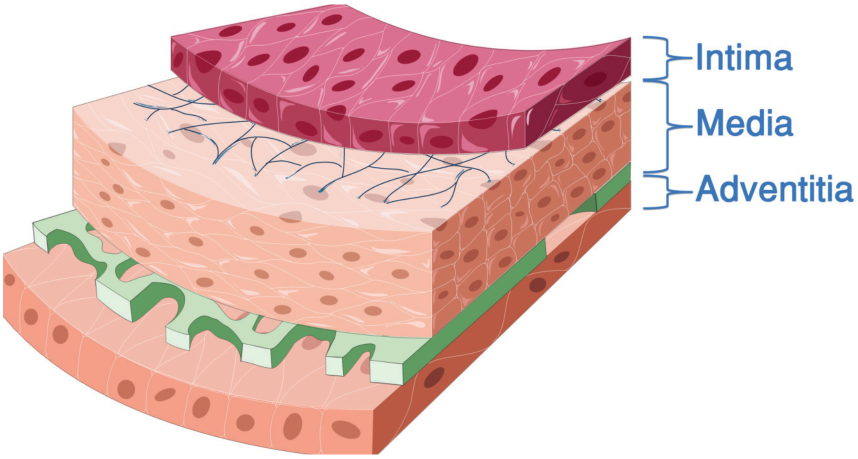

Figure 1.5: Composition of the arterial wall. The artery wall is composed of three main layers: the intima (internal), the media (middle), and the adventitia (external). [*Arterial tunics, Servier Medical Art, CC BY*].

is the adventitia and is mainly composed of elastic tissue, and collagen; this layer is responsible for the stability of the artery. Then comes the media made of muscle cells, elastic tissue and collagen; this layer ties the two surrounding layers together. The last layer is the intima, highly elastic, and directly in contact with the blood. The internal cavity, containing the blood, is referred to as the lumen.

Globally, all arteries have the same structure with the same cellular composition but in different proportions; indeed, depending on their locations and roles, they have more or less elastic cells. The size of the artery is also related to the location and the blood flow rate, the closer to the heart the larger.

1.1.3 Arterial disorders

As previously stated, the circulatory system is a complex vascular network composed of the heart and various vessels. The activity of the heart affects the condition of the arteries [5]. Indeed, heart weakness can induce poor oxygenation of the organs and can facilitate or worsen the deposition of agglomerates in the arteries and the formations of plaques. Inversely, plaques can induce a constraint on the heart by restraining the diameter of the artery and can evolve into different sicknesses [6].

The formation of a plaque is called atherosclerosis and is generally a slow process that takes decades to evolve into a pathological case. This disease is probably one of the most common ones since it affects almost all people after 60, at different severity levels, and generally starts during childhood [7] and worsens with age. This disease develops through different stages (Fig. 1.6). The first step is the presence

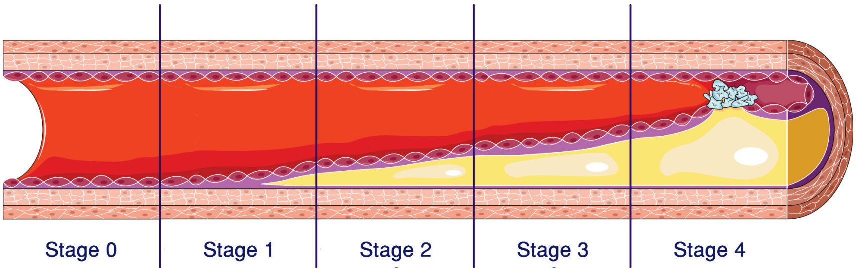

Figure 1.6: Progression of atherosclerosis: (0) healthy/fatty streak, (1) lesion, (2) atheroma, (3) fibrous plaque, and (4) advanced plaque/rupture. [*From atheroma to thrombosis, Servier Medical Art, CC BY*].

of a fatty streak that cannot be distinguished from a healthy artery. The lesion is the first stage that can be visible using histology. Then comes the formation of an atheromatous plaque. The disease becomes clinically apparent with the formation of the fibrous plaque, which is the third stage. The last stage will depend on the patient, localization of the artery, and different external and still unknown parameters. The last stage can be critical stenosis that drastically reduces the diameter of the artery. Another possibility if the formation of a thrombus, a blood clot, that clogs the artery. The last option is the formation of an aneurysm, a local distortion of the artery, that can lead to the rupture. In all cases, the last stage can be deadly since the arteries oxygenate the organs with a significant flow rate. The mortality rate is high for ruptures due to the significant bleeding; as an example, the blood flow rate in the descending aorta is around 4.3 L/min [5]. Even without evolving at the last stage, a rupture of the fibrous plaque (Fig. 1.7) can occur and creates a clot downstream of the original location. Depending on the size and localization of this rupture, the clot can block an artery and stop the oxygenation of a part of the body. More critical, it can block a brain vessel and cause irreparable brain damage causing dead, psychological, or motor difficulties. Indeed, 80% of patients hospitalized for stroke experience hemiparesis (paresis of one entire side of the body) of which 40% chronically [8]. Moreover, one-third of patients who had a stroke recover, either entirely or with a very minimal residual disability, one-third recover with a residual disability, and about one-third die [9].

Even nowadays, the causes of plaques and how they form remain unclear. It has been shown that there are several risk factors such as family history, high blood pressure, tobacco, cholesterol, or obesity, for instance [6]. When a severe plaque is detected, there is no proper treatment except surgery to deploy a stent that will dilate the artery or reopen the artery or derive the blood flow [10]. Preventive measures are mainly preferred if the disease is detected at an early stage and include a healthy lifestyle and medications (such as aspirin) to prevent clots [10], [11]. Therefore, the earliest detection of this disease remains a priority.

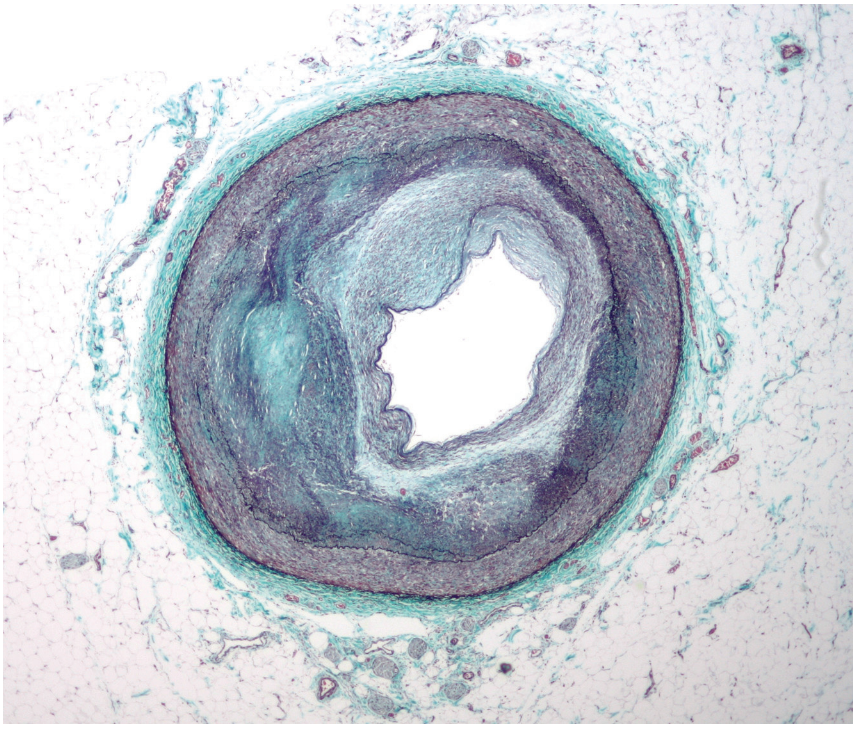

Figure 1.7: Micrograph of an artery slice with significant atherosclerosis. The fibrous plaque significantly reduces the diameter of the lumen. [*RCA atherosclerosis, Wikimedia Commons - Nephron, CC BY-SA*].

1.2 Ultrasound imaging

The second section of the first chapter presents ultrasound imaging. This section is broken down into five subsections: in a clinical context, principles of ultrasound, focused imaging, plane wave imaging, and image formation. In the following, the use of ultrasound imaging in clinics and principles are described with the techniques permitting to get exploitable ultrasound images at high frame rates.

1.2.1 Clinical context

Ultrasound imaging has been used for assessment of cardiovascular properties since the 50s [12], and since the 70s with Doppler for flow imaging [13]. Nowadays, it is widely used along with Doppler in routine check-ups and for the evaluation of the severity of pathologies. Indeed, ultrasound imaging brings a qualitative and quantitative diagnostic imaging technique in clinics; it is generally used to create an image of the organ of interest coupled with measurements based on both grayscale images and Doppler velocities.

Ultrasound referred to the sound waves sent into the medium in a frequency range,

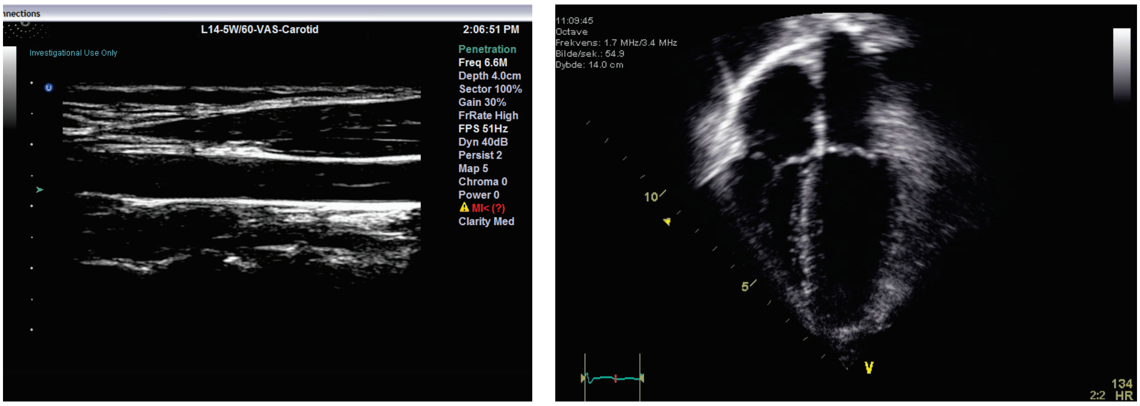
(a) (b)

Figure 1.8: Two conventional ultrasound images: (a) a common carotid artery, and (b) an echocardiogram. [(b): *Echocardiogram four chambers, PD*].

in clinics, from 1 MHz to 25 MHz depending on the application and the acquisition depth. This method of medical imaging is nowadays widely used and has the advantages, unlike other imaging methods, to provide images in real-time, and can be portable. Moreover, it is relatively low cost compared to other imaging modalities, painless for the patient, and does not use any ionizing radiation. Drawbacks include the limited field of view, image variability depending on patients and clinicians, and difficulties to image structure behind bone or air. Despite those limitations, the benefits of ultrasound make it widely used in angiology, cardiology, gynecology, obstetrics, and urology, for instance. In cardiology, ultrasound is commonly used as an investigation tool for the vessels (Fig. 1.8a) and heart (Fig. 1.8b). The interpretation is based on a visual inspection of the grayscale images. A diagnosis can be made depending on the aspect of the images, strongly based on the experience of the clinician, coupled with anatomic and functional measurements like quantitative flow estimates.

1.2.2 Principle

Ultrasound imaging is based on the propagation of ultrasound waves into the medium of interest. Each medium can be decomposed into multiple scatterers that backscatter ultrasound after insonification [14]. For academic purposes let us consider a punctual source (Fig. 1.9a) transmitting a pressure wave at time t_1 with a scatterer point at a distance z_0 of the initial source. After propagation, the wave will reach the scatterer at time t_2 (Fig. 1.9b); the initial wave will still propagate while being also backscattered by the scatterer. The speed of sound through the medium will determine the time required for the wave to reach the scatterer at the

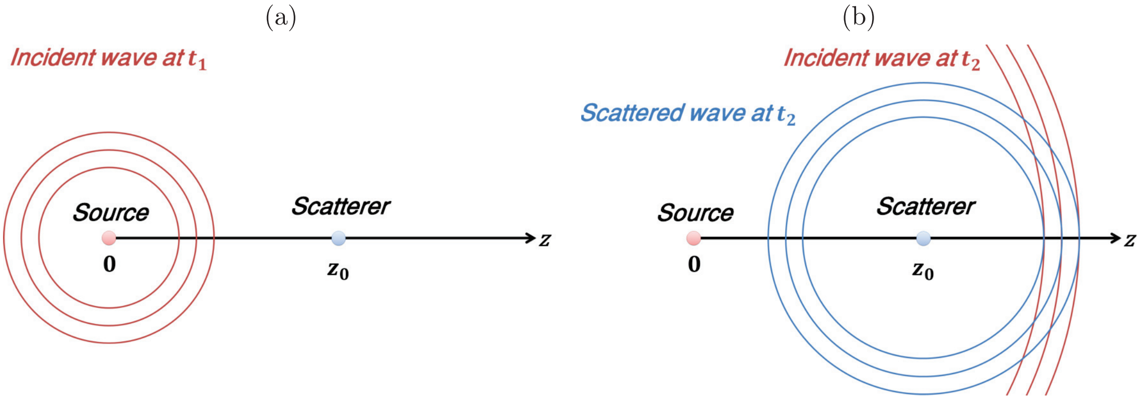

Figure 1.9: Principle of backscattering: (a) incident wave at t_1, and (b) incident wave and scattered wave at t_2.

position z_0; there is a time-distance duality. This wave can be described into a medium, assuming that the pressure and density variations are small compared to the initial state, based on a linear wave equation (Eq. (1.1)) [14], [15] for a point at the position $\vec{r}$ and at t:

$$\nabla^2 p\left(\vec{r}, t\right) - \frac{1}{c_r^2}\frac{\partial^2 p\left(\vec{r}, t\right)}{\partial t^2} = \frac{-2\Delta c\left(\vec{r}\right)}{c_r^3}\frac{\partial^2 p\left(\vec{r}, t\right)}{\partial t^2} + \frac{1}{\rho_r}\nabla[\Delta\rho\left(\vec{r}\right)]\cdot\nabla p\left(\vec{r}, t\right) \tag{1.1}$$

where p and ρ are the slight ripples inside the pressure and density fields respectively, c_r is the speed of sound in the tissue at rest while ρ_r is the density of the tissue at rest, and Δc and $\Delta\rho$ are the local variations of the speed of sound and density, respectively. This equation (Eq. (1.1)) represents the evolution of the pressure wave (left side) as a function of space and time against the wave behavior due to heterogeneities in the medium (right side). In case of a perfect homogeneous medium, the right term is equal to zero since there is no variation in the density or speed of sound (Eq. (1.2)) [14]:

$$\nabla^2 p\left(\vec{r}, t\right) - \frac{1}{c_r^2}\frac{\partial^2 p\left(\vec{r}, t\right)}{\partial t^2} = 0 \tag{1.2}$$

Those equations describe the wave propagation (Eqs. (1.1) and (1.2)) in heterogeneous and homogeneous media, respectively. In clinics, tissues are composed of different layers that do not have the same speed of sound and attenuation (Tab. 1.1) [16]–[18]. However, this effect can be minimized from a global perspective by choosing an averaged speed of sound (Tab. 1.1). In the end, the pressure wave is also dependent on the attenuation, which is a function of the distance and the frequency (Eq. (1.3)) [16]:

$$p\left(\vec{r}, t\right) = p_0\left(\vec{r}, t\right)\exp^{-\alpha(\vec{r}, f)} \tag{1.3}$$

Table 1.1: Speed of sound and attenuation depending upon the medium

Medium	**Speed of sound** (m/s)	**Attenuation coefficient** (dB/MHz/cm)
Water	1 480	0.002
Blood	1 575	0.15
Fat	1 450	0.6
Soft tissue	1 540	0.75
Muscle	1 585	1.5
Bone	4 080	10

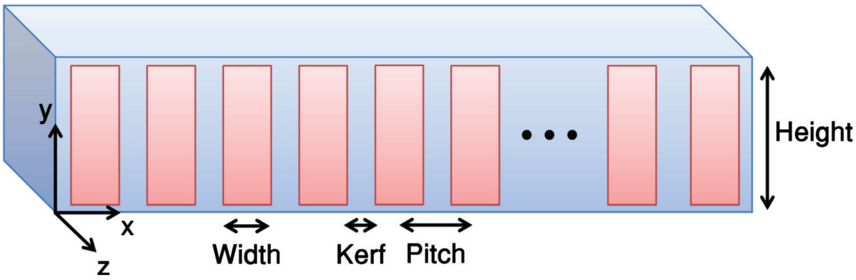

Figure 1.10: Diagram of a linear array probe. Several elements are aligned on the probe's head to create the actual full transducer.

where α is the attenuation coefficient and is a function of the distance to the initial source and the frequency, and p_0 is the pressure wave without attenuation. This attenuation effect can be corrected using the time gain compensation (TGC) in reception if the signal-to-noise ratio (SNR) is adequate. In clinics, the values for the soft tissue (average of fat, muscle, and water) are chosen by general consent.

The speckle and grayscale level that can be observed in ultrasound images (Fig. 1.8) is due to scatterers and so to heterogeneities in tissue. Indeed, each scatterer creates, if insonified by a pressure wave, a scattered pressure wave that will be interpreted as an electric signal by the transducer to render the final ultrasound image. The energy of this echo is dependent on the amplitude and density of scatterers, for instance, echoes coming back from flow have less energy than the ones from tissues. Each pressure wave interferes with others, and they sum up to create a more complex pressure field than the initial spherical pressure wave generated by every single source. In the medium, each scatterer becomes the source of a spherical wave, so the sum of these secondary waves determines the form of the pressure field at any subsequent time; this principle can be used to transmit any desired waveform. Indeed, the ultrasonic probe (Fig. 1.10) is made of several elements (typically 64 to 256 elements for a linear array probe) that can convert an electric signal to a pressure wave, and vice versa, to create any waveform into the medium. In theory, to obtain the desired waveform, the elements must have an infinitesimal size. In practice, the elements have a determined width and are distant from each other; this distance is called kerf while the width plus the kerf is the pitch. The limited aperture and element spacing in the ultrasonic probe create unintended lobes that are local maxima in the radiation pattern of the pressure field and which do not correspond to the main lobe (desired maximum) [16]. An element spacing which does not respect the Nyquist–Shannon sampling theorem in space (half of the wavelength) will create grating lobes at specific angle positions of the main lobe. The limited aperture creates side lobes in the pressure fields. Side lobes are undesired local maxima around the main beam. Generally, the power density of the side lobes is lower than the main beam pattern [16]. In practice, those effects are both due to the limited aperture and the Nyquist–Shannon sampling theorem. However, those effects can be minimized using an adequate ultrasonic transmit strategy [16], [19].

In summary, the probe, composed of piezoelectric elements, can transform an electric signal to a pressure wave. This wave propagates through the medium, after attenuation and backscattering, the echoes are converted into electric signals by the probe. In the end, the radio-frequency signals recorded by the probe take into account the attenuated echoes which include artifacts such as side and grating lobes; those signals also include the two-way impulse response (transmit and receive) of the probe.

1.2.3 Focused imaging

As explained in the previous section, the elements can be used with different delays to focus an ultrasound beam into the medium. In clinics, due to the legacy of the past since it was inspired by sonar, ultrasound imaging is mainly based on a scan line mode which used a focused transmit (Fig. 1.11) [20]. The waveform in Fig. 1.11 was simulated using the Field II software [21], [22] with MATLAB (The MathWorks, Natick, Massachusetts, United States); simulation parameters are described in Tab. 1.2. The propagation of the waveform (Figs. 1.11a to 1.11c) shows that the thinnest lateral resolution is at the focal depth (Fig. 1.11b). Before (Fig. 1.11a) and after (Fig. 1.11b) the focal depth the lateral resolution decreases. This technique as the advantage to concentrate the energy at a specific depth and line of interest in the medium (Fig. 1.11d). Afterward, the echoes from the focal point can be received by the probe. However, to fully scan the medium, the focal point needs to be swept along the lateral position axis. It is also possible to repeat the focalization at several depths. Consequently, the frame rate is directly related to the number of focal points used to sweep the region to be imaged.

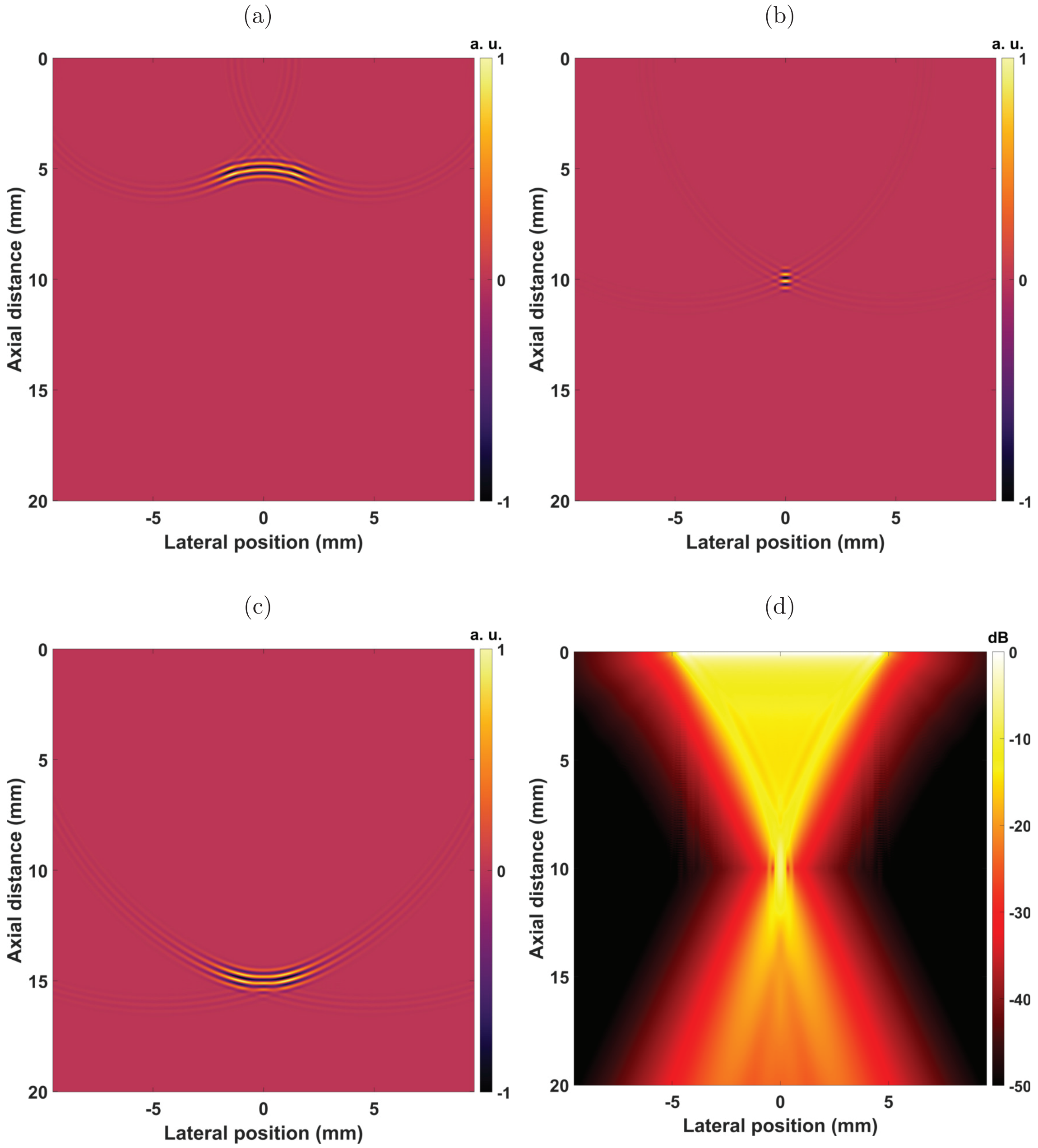

Figure 1.11: Simulated propagation of a waveform to a focal point: (a) waveform at 5 mm depth, (b) waveform at 10 mm depth, (c) waveform at 15 mm depth, and (d) maximum pressure in the medium. The waveforms are normalized while the maximum pressure is in normalized dB.

Table 1.2: Parameters of the simulated waveform propagation

Parameter	**Value**
Number of elements	64
Pitch	150 μm ($\lambda/2$)
Aperture	Full aperture
Excitation pulse	5-cycle sinusoidal
Pulse apodization	Hann
Central frequency	5 MHz
Sampling frequency	100 MHz
Speed of sound	1 500 m/s
Focal depth	10 mm
Receive and transmit apodization	Rectangular

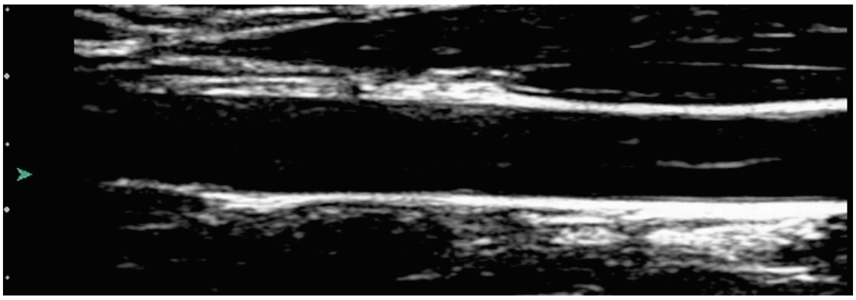

Figure 1.12: Common carotid artery from a medical scanner. The image quality permits to distinguish thin structure such as the intima-media complex at the lower wall.

Typically, in clinics, the maximum reachable frame rate with this imaging technique is around a hundred of images per second. A positive note is that the image quality is good in both resolution and contrast (Fig. 1.12), it is possible to distinguish very thin structures in images such as, for the carotid, the intima-media complex.

1.2.4 Plane wave imaging

To overcome the relatively low frame rate, which is not always sufficient to capture the fastest phenomena happening in the tissues, the use of broad wave imaging has been proposed as an alternative. Plane wave is a broad wave that can be used for high frame rate imaging (Fig. 1.13) [23]–[26]. The simulation in Fig. 1.13 was performed using the same settings as the propagation of a focused waveform (Fig. 1.11 and Tab. 1.2) except for the focal point. Indeed, a plane wave is sent into the medium (Figs. 1.13a to 1.13c) without any focal point. This technique has the advantage to insonify a larger region in just one transmit (Fig. 1.13d) compared to the focused mode (Fig. 1.11d). Afterward, the echoes from all the

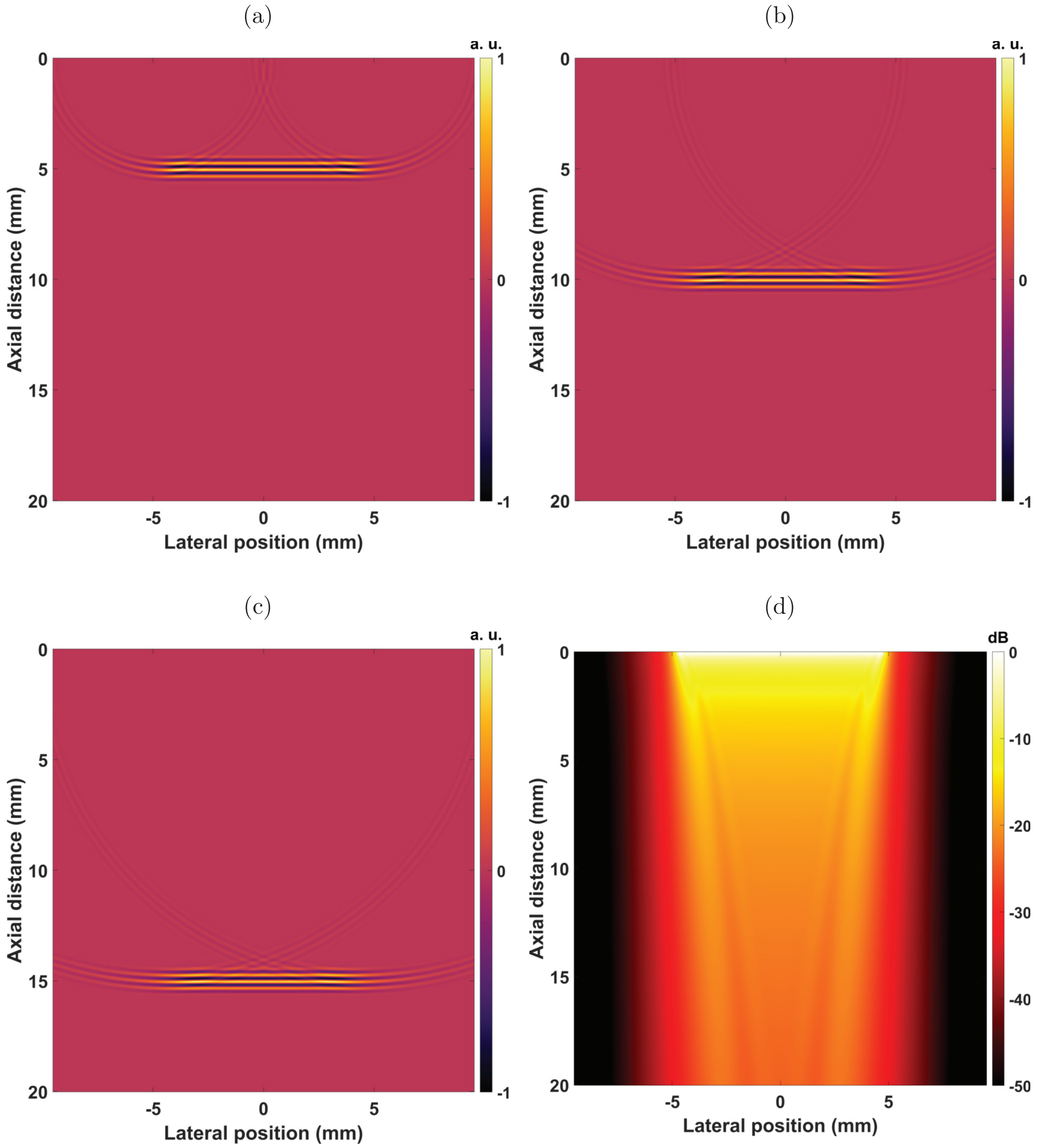

Figure 1.13: Simulated propagation of a plane wave: (a) waveform at 5 mm depth, (b) waveform at 10 mm depth, (c) waveform at 15 mm depth, and (d) maximum pressure in the medium. The waveforms are normalized while the maximum pressure is in normalized dB.

medium are received by the probe. Due to the lack of transmitting focus, the quality of an image of such a broad insonification is not as good as in focused mode in terms of resolution, contrast, and noise level. To recover a high image quality, it is also possible to do the insonification several times using different steering angles to increase the image quality [25]; such compounding synthetically creates a transmit focus.

Other approaches have been proposed for ultrafast ultrasound imaging. Before plane wave imaging was developed synthetic imaging where each element is used in transmit while the reception is achieved with all the elements [27]. This results in sending spherical waves into the medium; at each receive, a low-resolution image is created. All the images are then summed up to get a high-quality image. However, the frame rate is then directly reduced by the number of elements used in the sequence. Diverging waves can also be used, they are a variant of plane waves where the waves diverge into the medium permitting to get a larger field of view at a cost of greater energy dispersion. Such approaches have been used with phased arrays, which are quite small for cardiac imaging, to estimate velocities in a larger field of view [28]. Lately, multi-line transmit has been proposed as an intermediate solution between plane/diverging wave imaging and focused imaging [29]. It consists of sending a series of several beams at the same time into the medium, permitting to get a higher frame rate compared to focused imaging but at a cost of the creation of cross-talks artifacts. They occur because of the interactions between the different beams on both transmit and receive.

Consequently, the frame rate is limited by the maximum acquired depth and the number of steering angles. Typically the frame rate can be up to 10 000 images per second in superficial vessels without any compounding. The image quality is not always as good as the focused mode (Fig. 1.14), but with the improved temporal resolution, it is possible to capture fast phenomena that can occur in organic tissue.

1.2.5 Image formation

Regardless of the transmit mode, when receiving the echoes coming from the medium, it is needed to transform single-element signals into an actual image. This step is called receive beamforming and compensates for the spherical propagation of scattered waves produced in the medium.

Let us consider the raw signals (Fig. 1.15a), received by the probe after insonification, and the corresponding image after beamforming (Fig. 1.15b). The simulation

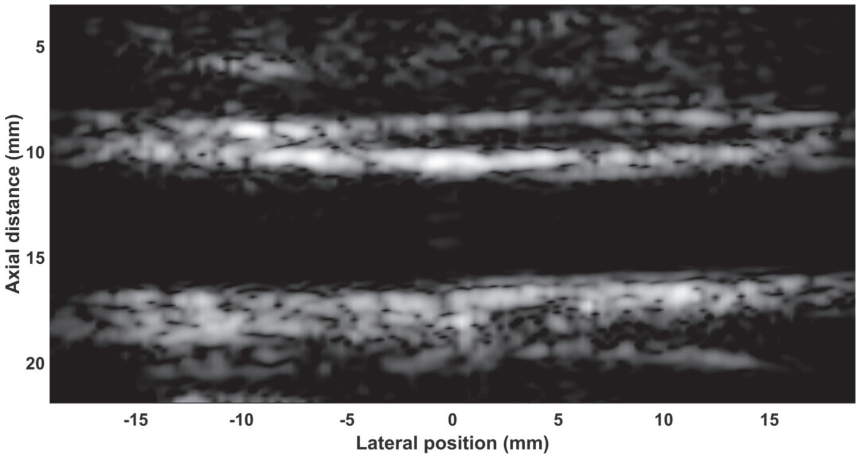

Figure 1.14: Carotid artery from a research scanner using plane wave imaging. Only one horizontal plane wave was used to insonify the artery.

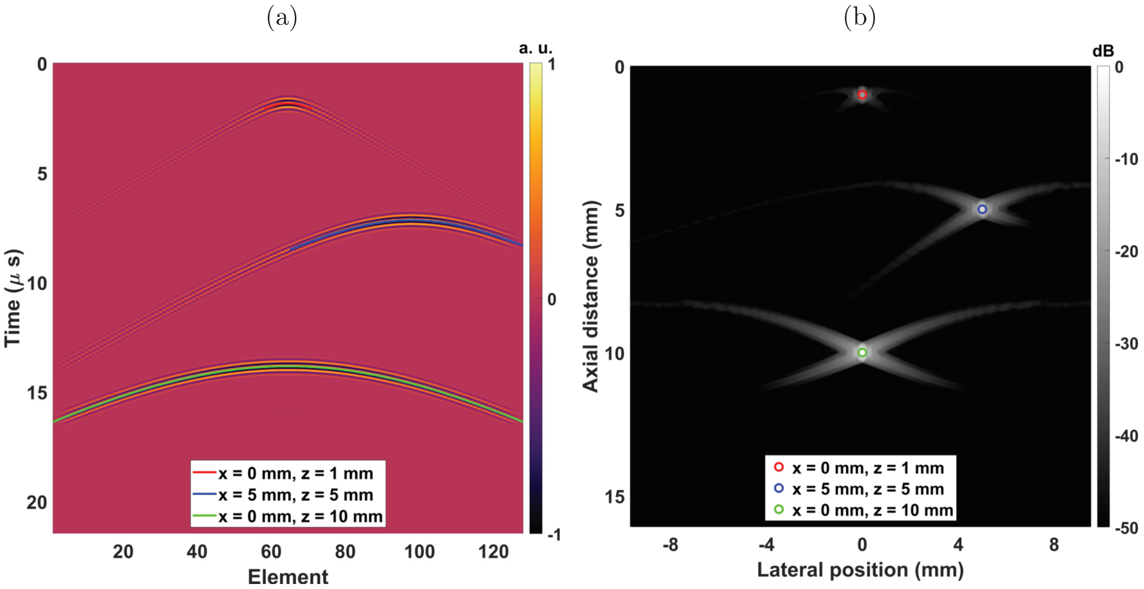
(a)

(b)

Figure 1.15: From raw signals to B-mode image: (a) raw signals from 3 scatterers with the corresponding delays (colored lines) for beamforming, and (b) log-compressed envelope of the beamformed radio-frequency signals with the true positions of the scatterers.

in Fig. 1.15 was performed using the same settings as the propagation of a plane wave (Fig. 1.13 and Tab. 1.2) except this simulation used a 128 element linear probe array and received echoes were saved instead of the wave propagation. In this example, three scatterers were considered in this simulation (Fig. 1.15), because of the limited geometry of the probe and the propagation, each scatterer is recorded as a hyperbola (Fig. 1.15a) by the probe. In Fig. 1.15a the red, blue, and green curves are the hyperbolic laws, to compensate for the time of flight, computed for the scatterers with the same colors in Fig. 1.15b. To obtain the image in Fig. 1.15b this hyperbolic law is computed for each point of the medium, and the signals along this curve are summed to give one single value at this specific point. However, in Fig. 1.15a only a part of the hyperbolas are taken into account. Indeed, because of the directivity of the elements, the signals fade with the distance from the center. Consequently, too far from the center of the hyperbola, the signal is only due to noise and other scatterers. Generally, beamforming is performed with an aperture dependent on the depth which is fixed by the f-number (Eq. (1.4)):

$$F_{\#} = \frac{D}{L} \tag{1.4}$$

where L is the total width of the active aperture, and D is the distance to the focus; $F_{\#}$ is often kept constant. In Fig. 1.15a the f-number is fixed to 1. Conventionally, the medium is considered to be homogeneous for reconstruction, and the medium is assumed to be made of soft tissue only having a speed of sound of 1 540 m/s to compute the delays for the beamforming algorithm; this algorithm is referred to DAS for Delay-And-Sum [30]. A weighting function (also called apodization) can also be used in reception, like it can be used in transmission, to reduce artifacts that can occur in ultrasound images [16]. Received echoes are radio-frequency signals, for visualization with a grayscale map an envelope detection (demodulation at the carrier frequency) is performed after beamforming with a log-compression (B-mode) to adapt the wide dynamics of the ultrasound images to the human vision capabilities.

1.3 Pathological markers

The third section of the first chapter presents the pathological markers. This section is broken down into two subsections: wall, and flow. In the following, both wall and flow markers are described with their usefulness for clinical pathology detection.

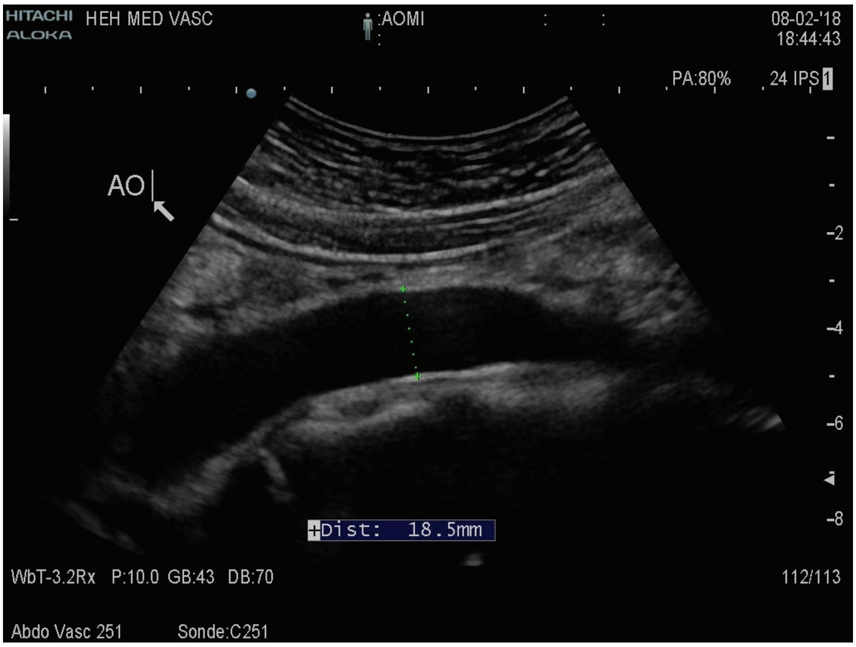

Figure 1.16: Measurement of the aorta diameter using a clinical scanner. The measurement is based on the grayscale level of the B-mode image; the aorta is from a healthy volunteer. [*Courtesy of Pr. Anne Long, Hôpital Edouard Herriot, Lyon, France*].

1.3.1 Wall

Ultrasound imaging is not only used for qualitative inspection but also for quantitative measurements [31]. In clinics, cardiologists use grayscale images to evaluate different tissue characteristics. A standard tissue measurement is the evaluation of the vessel diameter (Fig. 1.16) [31]. Indeed, artery remodeling can occur because of age or due to a pathology [32]. Such measurements also permit to evaluate the severity of stenosis by measuring the inner diameter before, after, and in the middle of the stenosis (flow is also studied to better distinguish the wall limits). The severity of the stenosis is quantified by a measure in percent, which is the shrinking of the vessel. The occlusion occurs at 100%, and stenosis with a shrinking higher than 50% (75% of the initial section of the artery) is considered to be of concern [33].

Tissue motion can be extracted to give quantitative values to evaluate the behavior of the arterial wall in the presence or before pathology development [34]. It becomes possible to evaluate the distensibility [35], which is the relative radius variation in percent, which should be related to the compliance of the artery [31]. Therefore, aging and pathology should influence tissue motion [36]. A more complex measurement, based on tissue movement, is the estimation on the pulse wave velocity [37]–[40]. Indeed, as illustrated previously in Fig. 1.2, the heart is subject to cycles which generate mechanical waves due to the opening and closing of the valves. Some of those mechanical waves propagate along the arteries in the body. However, the velocity of a mechanical wave is related to the stiffness of the propagation medium. Each mechanical wave induces a propagation along the vessel of a radial motion which is called pulse wave. If we consider an artery as a perfect cylinder, the pulse wave velocity (PWV) can be linked to the stiffness using the modified Moens-Korteweg equation (Eq. (1.5)) [41], [42]:

$$PWV = \sqrt{\frac{Eh}{2R\rho\,(1-\nu^2)}} \tag{1.5}$$

where E is the stiffness of the wall, h and R are the thickness and radius of the vessels respectively, and ρ and ν are the density and the Poisson's ratio. Even if in practice it is very difficult (even impossible) to accurately estimate all the vessel characteristics to obtain the stiffness directly, the PWV should reflect, and be an indirect measurement, of the rigidity. The PWV is useful to evaluate changes in stiffness due to sickness [43], for instance, in the presence of rigid atherosclerosis or diabetes. This metric is a good risk marker of the overall arterial health [43]–[45]. In clinics to estimate this propagation, clinician use the tonometry technique with two pressure sensors placed over the carotid artery in the neck and the femoral artery, the distance from one sensor to another is roughly measured, and the PWV is determined by the time shift estimated from both pressure waveforms; this technique gives a global value using an imprecisely estimated distance. However, this measurement is still in good correlation with PWV estimated by ultrasound [44].

1.3.2 Flow

Qualitative and quantitative inspections are also used in clinics for flow with ultrasound based on Doppler imaging [46]. Such measurements can be used to evaluate if an artery is occluded or if any backflow is present (Fig. 1.17) [47], [48]. For instance, in Fig. 1.17, the clinician uses the color Doppler for qualitative inspection. The green pointer is placed in the internal carotid artery, and the Doppler spectrum is evaluated at this position. At the top of the artery is the internal jugular vein. In the case of stenosis or plaque, the color Doppler is useful to detect the limit of the lumen and the actual size of the stenosis [48]. In the Doppler spectrum, no backflow Fig. 1.15 is present; some pathologies such as heart dysfunction can create a backflow in such an artery [49].

Moreover, clinicians also evaluate the peak systolic and end-diastolic velocities; the

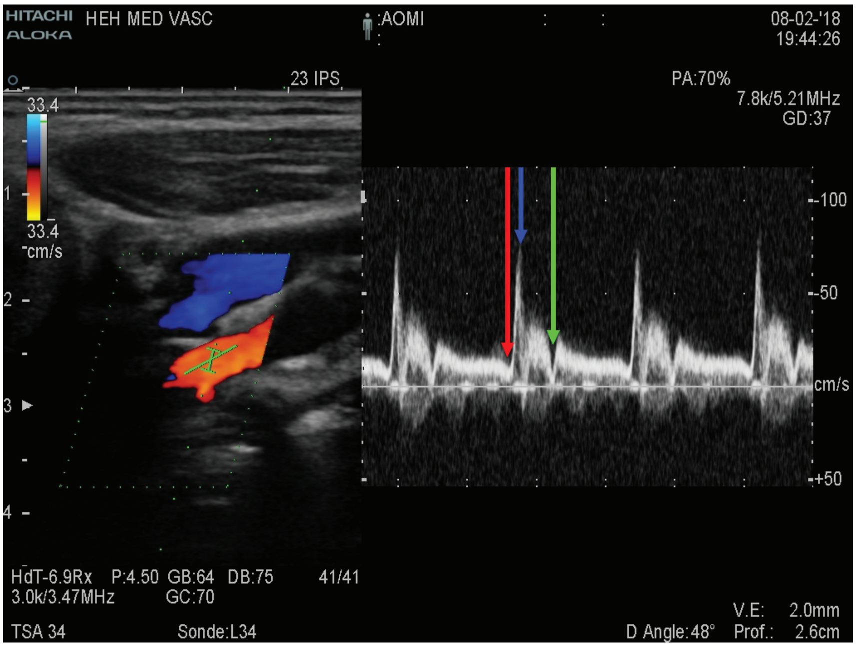

Figure 1.17: Measurement of the flow in an external carotid artery using a clinical scanner: (left) B-mode image superimposed with color Doppler, and (right) Doppler spectrum at the position of the green pointer in the image. In the spectrum, the arrows indicate the beginning of the systole (red), the systolic peak (blue), and the dicrotic notch (green). The data are from a healthy volunteer. [*Courtesy of Pr. Anne Long, Hôpital Edouard Herriot, Lyon, France*].

resistivity index, which is the ratio between those two values, is related to the vascular resistance of the vessel and is a marker of atherosclerosis risk in renal arteries [50]. In the case of stenosis, the flow is evaluated before, after, and in the middle of the stenosis for diagnostic purposes [51]. The turbulence of the flow is also evaluated, through both the color Doppler and Doppler spectrum, to identify the disruption risk in the presence of plaques.

More advanced properties can be accessed, such as the wall shear stress (Eq. (1.6)) [52]:

$$\begin{cases} WSS = & \mu WSR \\ WSR = & \left.\dfrac{\partial v}{\partial r}\right|_{r=R} \end{cases} \tag{1.6}$$

where WSS is the wall shear stress, μ is the blood viscosity, and WSR is the wall shear rate; WSR is also the spatial gradient parallel to the wall of velocity at the location of the vessel wall. The blood is a non-Newtonian fluid; the viscosity changes with shear stress and is also dependent on the artery. Consequently, the proper evaluation of the wall shear stress is difficult, because it is impossible to have access to the actual blood viscosity. However, like the pulse wave velocity, which is related to the stiffness, the wall shear rate is linked to the stress along the wall. This stress is often considered as one indication to evaluate the risk of plaque rupture or formation. Indeed, low stress has been supposed to facilitate the development of plaque while high stress after plaque development should increase the risk of inflammation and the rupture risk.

1.4 Interest of flow and wall analysis for pathology detection

Previously, it has been exposed that pathology, geometry, and aging influence both flow and wall motion in the arterial system. Even if nowadays ultrasound is widely used in clinics, both aspects are not fully studied together for inspecting and evaluating the severity of pathologies of arteries. However, because wall and flow patterns can be both affected, an imaging technique permitting to yield information from both media simultaneously could be highly relevant for pathology characterization. Indeed, such a technique could be able to provide pathological markers from the wall and flow independently, but also wall/flow markers due to the intimate connection between those two media.

It is well known that both flow and wall motion are strongly related to the properties of the vascular system. Consequently, a precise evaluation of their characteristics is essential for the detection and characterization of pathologies during their development or even at the earliest stage. Moreover, because the wall and flow are inherently linked, having both measurements simultaneously over a vast region of interest should be highly relevant for clinicians to quantify, for instance, the vulnerability of plaque. Indeed, a very rigid plaque coupled with a turbulent flow presents a huge disruption risk. By providing more information, with the simultaneous measurements, we could expect better detection, more precise diagnosis, and improved monitoring of artery pathologies. However, in clinical routine, only color Doppler coupled with Doppler spectrum at a relatively low frame rate are used as advised in the guidelines and do not give any vectorial flow information.

Consequently, most of the clinical studies are based on an incomplete flow information, and ultrasound acquisitions are realized at a relatively low frame rate (maximum 100 images per second using a scan line mode) while other techniques with plane mode imaging could provide wall motion, vectorial flow, and advanced pathological markers at high frame rates.

Chapter 2

Overview of Standard Motion Estimation Techniques in Vascular Ultrasound

The second chapter is an overview of the standard motion estimation techniques presenting the techniques that are commonly used in vascular ultrasound imaging. The Doppler-based techniques are first described, starting with a described chronological timeline of Doppler ultrasound. Therefore, both frequency-based and phase-based approaches are presented. Then, non-Doppler-based techniques are described, including the so-called speckle-tracking and optical flow approaches. After presenting the standard techniques, state of the art the specific subject of simultaneous measurement of tissue movement and flow is conducted. This state of the art includes previous works from several groups around the world in the last 20 years. The second chapter concludes with the goals and the selected approach during the thesis for the simultaneous measurement.

There is no scientific contribution in this chapter, which is based on a scientific literature review and book reading to understand and describe the signal processing methods.

2.1 Doppler-based techniques

The first section of the second chapter presents the Doppler-based techniques. This section is broken down into three subsections: a brief history of the development of Doppler ultrasound, frequency-based methods, and phase-based methods. In the following, Doppler methods are described with the description of the signal processing techniques and fundamental equations.

At this moment, clutter is not considered and will be more detailed in the chapter 4.

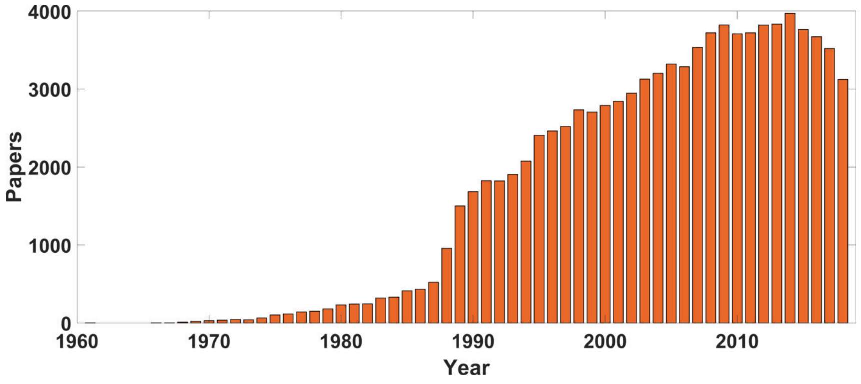

Figure 2.1: Number of citations over the years for the keyword "Doppler ultrasound". Data were extracted from PubMed.

Also, a vectorial flow method named transverse oscillation is widely described in the chapter 3.

2.1.1 Brief history of the development of Doppler ultrasound

As previously written, ultrasound imaging has been used in for the assessment of cardiovascular properties since the 50s [12], and since the 70s with Doppler for flow imaging [13]. By tracking the use of the keyword "Doppler ultrasound" in medical publications (Fig. 2.1) the first occurrence of this keyword appeared in 1961 in Science [53]. This first work, achieved by Franklin *et al.* [53] and indexed by PubMed, was about the measurement of blood velocity by estimating the Doppler shift with two crystal elements (one in transmit and one in receive) on the *in vivo* descending aorta of a dog.

In reality, applications of Doppler ultrasound began with a publication in The Journal of the Acoustical Society of America in 1957 by Satomura [12] with the first inspection of cardiac function using Doppler signals. However, the very first commercial ultrasound system for B-mode imaging was launched in 1963 in the United States by The James Picker company [54]. At this time, systems were using a single-element based on a mechanical scanning of the medium to obtain an image. Concerning flow measurement, the Doppler shift is estimated along the ultrasound beam, which gives only a projection of the true velocity and could lead to significant error if the beam-to-flow angle is below 60° [55].

To overcome this issue, from 1970 to 1980 several groups have proposed to use two single-element transmitters and/or two single-element receivers to solve this issue using a cross-beam approach [56]–[58]. Fahrbach [56] proposed to use two single-element transducer probes with an angle of 90° between them and both acting as transmitter and receiver. Hansen *et al.* [57] suggested using two single-element transmitters with one single-element receiver localized between the transmitters. Another interesting approach was developed by Uematsu [58] using one transmitter with two receivers.

As an alternative to single-elements, linear arrays for Doppler measurements started to be used in the late 70s by Pourcelot [59] permitting to obtain B-mode images without any mechanical scanning, coupled with flow information. The indexed papers in PubMed for Doppler ultrasound (Fig. 2.1) increases from 10 per year in 1968 to more than 200 per year in 1980 as a result of those technical and methodological innovations. In the same period, the first commercial duplex scanner (displaying both B-mode and Doppler information) was launched (®ATL MARK V, Advanced Technology Labs., Bellevue, Washington, United States) and allowed to begin clinical research using both B-mode and Doppler in the 80s [60]. This period is the actual entrance of Doppler ultrasound into clinical routine.

The establishment of duplex scanning as a means to detect and characterize the level of stenosis occurred in 1990s; the same year, the milestone of 1 000 citations per year has been reached for Doppler ultrasound (Fig. 2.1). A year after were published the first conclusions [61], [62] that patients with 70% stenosis or more should go under surgery. Those first conclusions led to the proposition of the first guidelines in 1995 [63]. In 1996, color Doppler providing flow information as a color map in vessels has been proved to be as accurate as magnetic resonance venography for peripheral vessels [64].

Those multiple innovations, based on new technologies coupled with innovative methods, have led to the widespread use of ultrasound in clinics for both surgery and examination routine. In 2000, the foundations on which Doppler ultrasound is based in clinics were laid. Nowadays, most of the medical scanner used in clinic routines are still based on those principles and technologies with some improvements.

In the previous paragraphs, several improvements in terms of instrumentation were discussed. However, the transmitting and receiving modes have not been discussed yet. Indeed, two methods are frequently used for Doppler ultrasound measurement called continuous wave (CW) Doppler, and pulsed wave (PW) Doppler; those methods differ in the type of transmission. For both of them, the principle is to send ultrasound towards a moving target (heart tissue or blood, for instance) and to receive the backscattered echoes. The velocity can be recovered using the frequency shift of the received signals (Eq. (2.1)):

$$f_d = 2f_0 \frac{v \; cos\,(\theta)}{c} \tag{2.1}$$

where f_d if the Doppler shift, f_0 is the transmit frequency, c is the speed of sound, v is the velocity of the scattered (red cell for blood), and θ is the beam-to-flow angle. Because the Doppler shift is proportional to $cos\left(\theta\right)$ the shift permits only to access the axial velocity component; in case of a normal angle to the ultrasound beam no Doppler shift is present in the received signals and the velocity cannot be estimated. Since the transmit frequency is known, the Doppler frequency can be recovered and is shifted in the audible range of frequencies (from 1 kHz to 20 KHz), which permits clinicians to both listen and watch the spectrum for diagnostics.

CW Doppler uses a continuous signal with a distinct transmitter and receiver, while PW Doppler transmits a short pulse into the medium and can use the same element for receiving the echoes. CW Doppler has the advantages not to be subject to any aliasing or limit on the maximum velocity that can be detected; a significant drawback is the lack of resolution of the method since it uses a continuous transmit. On the other hand, PW Doppler permits to obtain a resolution range because of the use of a short pulse; however, due to the time between transmit pulses the maximum Doppler shift that can be estimated is half the sampling frequency (inverse of the pulse repetition frequency, PRF). Because PW Doppler uses a short pulse, it is possible to extract both B-mode image and Doppler information from the same acquisition mode, while the CW Doppler cannot return a B-mode image due to the lack of resolution of the method. Even if, in clinics, the PW still uses quite a long pulse that gives a bad resolution; a dual-mode is often used in practice.

2.1.2 Frequency-based methods

In the beginning, Doppler systems were using only the CW Doppler mode. This technique is still used for quantitative measurement, as shown in the previous chapter, in Fig. 1.17, to estimate the velocity in the region of interest. Indeed, after demodulation at the transmit frequency any shift should be due to the moving targets if we consider the transmit as monochromatic and do not take into account frequency changes due to propagation into a non-linear and attenuating environment.

The Doppler spectrum is the power spectrum of the received signal after demodulation at the transmit frequency, which can be corrected of the angulation and acquisition parameters to yield accurate velocities in m/s. Depending on the mode and the settings used, the resolution cell can be more or less large; this cell is called gate or sample volume. While in clinics, the maximum velocity is often used with a gate covering all the diameter of the vessel, it is possible to use a smaller gate to yield a local mean velocity (Eq. (2.2)):

$$\bar{f} = \frac{\int_{-\infty}^{+\infty} f \, P\left(f\right) \, df}{\int_{-\infty}^{+\infty} P\left(f\right) \, df} \tag{2.2}$$

where $\bar{f}$ is the mean frequency, P is the power spectrum of the received signal, and f is the frequency range. The power spectrum can be digitally calculated in several ways, depending on the application. A common way to do it is based on the spectrum of the signal by computing the power spectral density, which is the Fourier transform of the autocorrelation function (Eq. (2.3)) [65]:

$$P_s\left(f\right) = \mathscr{F}\left\{R_s\left(\tau\right)\right\} \tag{2.3}$$

where P_s is the power density spectrum of the signal and R_s the autocorrelation of the signal itself. In practice, the signal has a limited observation time, which is equivalent to apply a rectangular window on the observation (Eq. (2.4)):

$$P_w\left(f\right) = \mathscr{F}\left\{R_w(\tau)\right\} \tag{2.4}$$

where P_w is the power density spectrum of the observation window (rectangular), and R_w is the autocorrelation of that window. Consequently, the observed spectrum is the convolution of those two spectra (Eq. (2.5), Fig. 2.2):

$$P\left(f\right) = P_w\left(f\right) \circledast P_s\left(f\right) \tag{2.5}$$

where P is the recorded spectrum for velocity estimation; $\circledast$ is the convolution operation. The power spectrum can be calculated at each time and display as a grayscale image to obtain what is called a Doppler spectrum (Fig. 2.3). From the mean frequency, the actual velocity can be recovered by knowing the speed of sound, transmit frequency, and beam-to-flow angle (Eq. (2.1)).

2.1.3 Phase-based methods

Another approach is to estimate the phase difference of the signal between successive insonifications of the medium. This approach is the one suggested by Kasai *et al.* [66], which is widely used nowadays. The received sampled signal can be written, after demodulation at the transmit frequency [67], as a complex signal (Eq. (2.6)):

$$s\left(t\right) = I\left(t\right) + jQ\left(t\right) \tag{2.6}$$

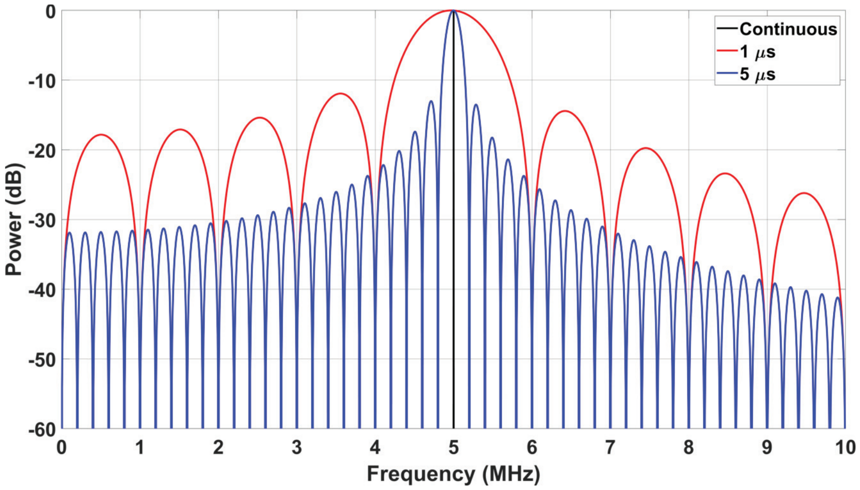

Figure 2.2: Power density spectra depending on the observation window: spectra of a continuous signal (black), a 1 μs signal (red), and a 5 μs signal (blue). Received signals are 5 MHz sinusoidal waves, and each spectrum is normalized with its maximum for better visualization and comparison of spectra. The limited observation window creates lobes in the spectrum and widens the main lobe due to the spectrum of the window (Eq. (2.5)).

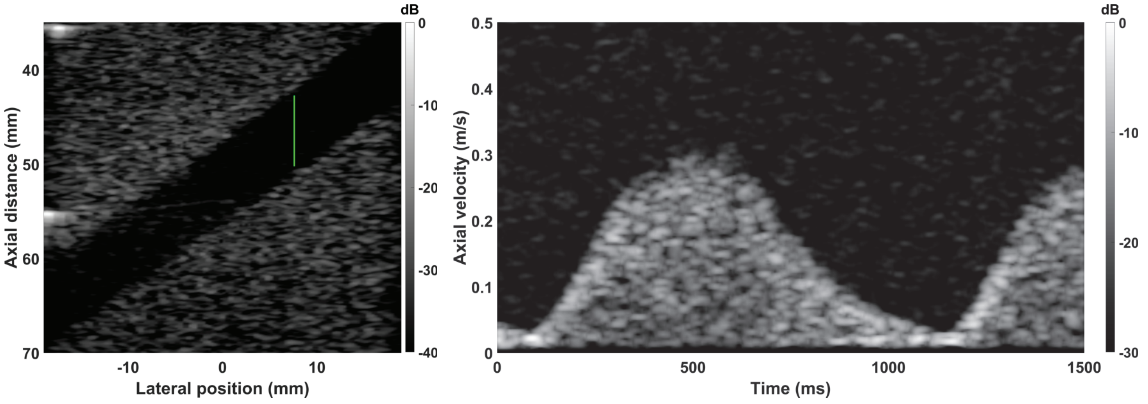
(a) (b)

Figure 2.3: Example of Doppler spectrum obtained with a research scanner: (a) B-mode image of a 40° vessel in a flow phantom (Gammex Doppler 403$^{\text{TM}}$, Gammex, Middleton, Wisconsin, United States) using a plane wave imaging mode with a Verasonics Vantage$^{\text{TM}}$ 256 system (Verasonics, Redmond, Washington, United States), and (b) corresponding Doppler spectrum along the green line in (a). The spectrum contains 512 velocity lines and is smoothed afterward using a window of 10 ms. The spectrum in (b) contains all the velocities along the green line in (a).

where s is the complex signal with I and Q are respectively the in-phase and quadrature components and j is the imaginary number. The mean complex autocorrelation function for the signal can be expressed as (Eq. (2.7)):

$$\hat{R}(\tau) = E\left\{s^{*}(t)\ s(t+\tau)\right\} \tag{2.7}$$

where $\hat{R}$ is the complex autocorrelation function, and τ is the lag for estimation; $*$ is the conjugate notation, and E is the expected operator. The phase can then be extracted using (Eq. (2.8)):

$$\Delta\hat{\Phi}(\tau) = atan\left(\frac{\mathscr{I}\left\{\hat{R}(\tau)\right\}}{\mathscr{R}\left\{\hat{R}(\tau)\right\}}\right) \tag{2.8}$$

where $\Delta\hat{\Phi}$ is the estimated phase shift; $\mathscr{I}$ and $\mathscr{R}$ are respectively the imaginary and real functions, and *atan* is the inverse tangent function[†]. The lag and the length for calculating the mean complex autocorrelation can be both chosen as a bias-variance trade-off but τ is also related to the Nyquist velocity limit due to phase wrapping. Finally, velocity can be recovered using the parameters of the acquisition (Eq. (2.9)):

$$v_z = \frac{PRF}{\tau}\frac{c}{4f_0}\frac{\Delta\hat{\Phi}(\tau)}{\pi} \tag{2.9}$$

where v_z is the axial component of the velocity, c is the speed of sound, PRF is the pulse repetition frequency, and f_0 is the center frequency. The left side of the equation no longer depends on the lag as long as there is no aliasing and assuming a constant velocity in the observation window. In practice, motion estimation is performed using spatial filtering onto the lag τ autocorrelation estimate in the complex domain to reduce variance in the estimates. By calculating the mean complex autocorrelation with a sliding window, velocity can be extracted as a function of time. This method permits to render a 2D color Doppler map where color represents the value of the axial component of the velocity (Fig. 2.4). Several other techniques were developed after Kasai *et al.* mainly based on the correlation of received signals [68], [69]. The phase shift estimation technique presented hereby has been modified by Loupas *et al.* [70] to compensate for the carrier frequency

---

[†] For implementation, the arctangent (atan) and 2-argument arctangent (atan2) functions can both be used. The atan function gives a result in the range $-\pi/2$ to $\pi/2$, while the atan2 function is in the range $-\pi$ to π. The atan function simply computes the inverse tangent, if the tangent is positive the angle is from the first or third quadrant, and if it is negative it could come from the second or fourth quadrant. By convention, atan returns an angle from the first or fourth quadrant. To get full information the atan2 function looks at the values of the sine and cosine separately to get rid of the ambiguity.

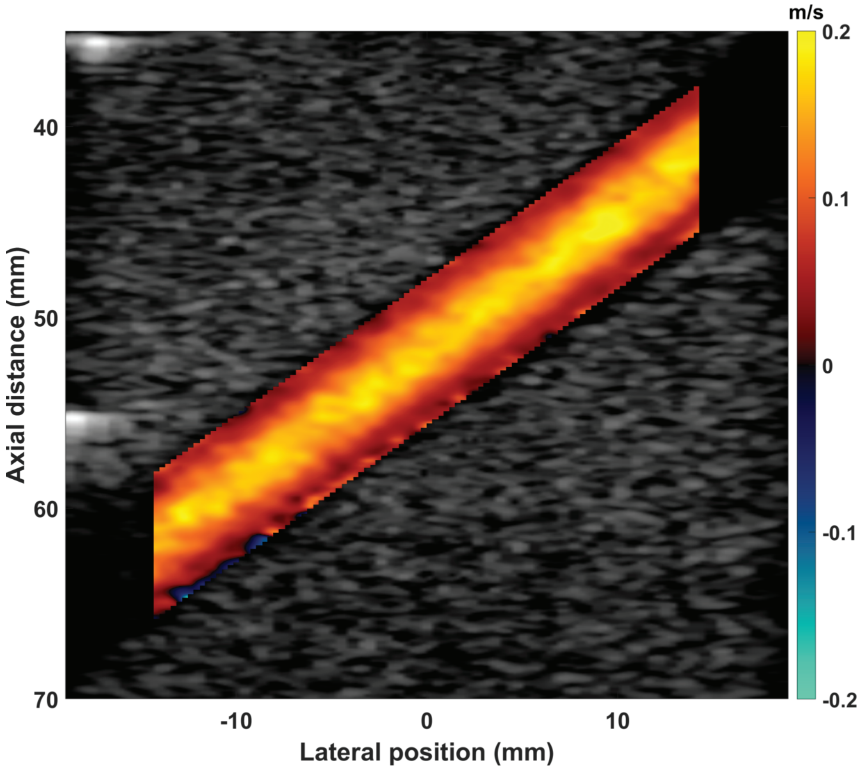

Figure 2.4: Example of color Doppler with a research scanner. Acquisitions were performed on a 40° vessel in a flow phantom (Gammex Doppler 403$^{\mathrm{TM}}$, Gammex, Middleton, Wisconsin, United States) using a plane wave imaging mode with a Verasonics Vantage$^{\mathrm{TM}}$ 256 system (Verasonics, Redmond, Washington, United States) superimposed over with the B-mode image. The algorithm described by Kasai *et al.* [66] is used with an ensemble length of 64 frames and through a window, for spatial filtering, of 1 mm × 1 mm. To mitigate stationary clutters, the beamformed signals were high-pass filtered by a 1^{st} order Butterworth with a cutoff velocity of 1 cm/s. The dynamic range is 40 dB.

shifts in Doppler ultrasound. Indeed, the frequency is supposed to be constant in the medium. In reality, the frequency can locally change due to local variations in the medium, attenuation, and artifacts.

2.2 Non-Doppler-based techniques

The second section of the second chapter presents non-Doppler-based techniques. This section is broken down into two subsections: block-matching and optical flow. In the following, non-Doppler techniques are described with the description of the signal processing techniques and fundamental equations.

2.2.1 Speckle-tracking

Block-matching is a generic word referring to techniques matching blocks in a first image to other blocks in a second image; and they have been adapted for ultrasound [71], [72]. Initially, particle imaging velocimetry (PIV) is an optical method of flow visualization that originated from laser speckle velocimetry in the 1980s [73]. This technique has been extended to ultrasound in the 1990s by Trahey *et al.* [74], [75] for velocity vector imaging of the blood circulation. It is generally called echo-PIV when blood is seeded with contrast agents [76]. If an appropriate wall filter is used, echo-PIV can be achieved by tracking the natural speckle patterns issued from the blood scatterers [77]. Echo-PIV has been used to investigate the intricate flow patterns that can occur in the cardiovascular system [77], [78].

Most of the echo-PIV algorithms use a cross-correlation approach; a standard technique is to use an FFT-based cross-correlation algorithm [79], [80] to track the speckles of the (not log-compressed) real envelopes. The technique is as follows: two successive real-envelope images #1 and #2 are subdivided into (m × n) subwindows (Fig. 2.5). If we consider w_1 and w_2 two consecutive subwindows and their respective Fourier transforms W_1 and W_2, the FFT-based normalized cross-correlation (NCC) can be written as follows (Eq. (2.10)):

$$NCC = \mathscr{F}^{-1}\left\{\frac{W_1 W_2^*}{|W_1 W_2^*|}\right\} \tag{2.10}$$

where the operator $\mathscr{F}^{-1}$ is the inverse Fourier transform; $*$ is the conjugate notation and $|\cdot|$ the absolute value. The relative displacements (Δ_i, Δ_j) onto a grid (i, j) from the 1^{st} to the 2^{nd} subwindows are given by the position of the NCC peak (Eq. (2.11)):

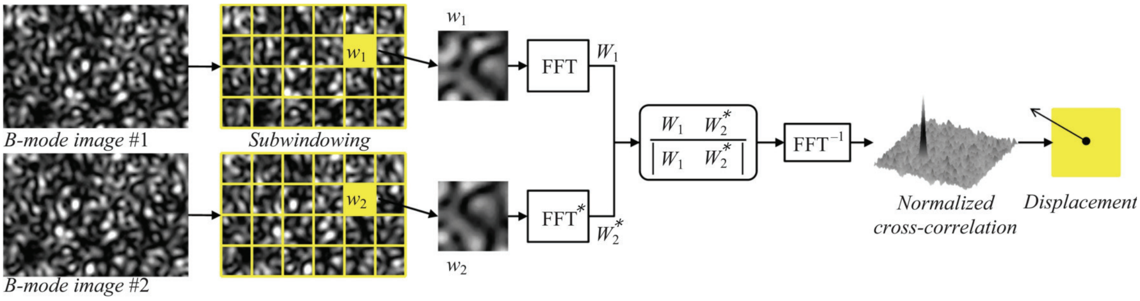

Figure 2.5: Block diagram of a speckle tracking algorithm. The implementation is phase-based and performed in the Fourier domain; two subwindows are used in a pair of images to compute the normalized cross-correlation. [*Adapted, ©2018, IET, from* [80]].

$$(\Delta_i, \Delta_j) = arg\left\{max_{(i,j)}\left\{NCC\right\}\right\} \tag{2.11}$$

where arg is the argument function, and max the maximum function. From (Δ_i, Δ_j) the displacement can be recovered in meters based on the pixel size.

To obtain subpixel estimates, the peak of the cross-correlation can be interpolated using a Gaussian or parabolic 2D fitting [79]. In the case of large displacement, a multiscale coarse-to-fine approach can be used to refine the estimates: the displacements are iteratively refined by decreasing the size of the subwindows. Also, post-processing has a major impact on the velocity field; the estimates can be smoothed under several smoothing constraints or based on a penalized least-squares approach [81], [82]. By combining all these approaches, this method can yield vector velocity fields even in the case of a complex flow pattern (Fig. 2.6).

2.2.2 Optical flow

Optical flow is another technique that can be seen as a block-matching algorithm, but with a different strategy. Optical flow is the analyze of the apparent velocities of movement of brightness in a set of images due to the actual motion. It is widely used in vision and machine vision application for tracking objects such as cars, bikes, or even a walking person on the street. Originally, the concept of optical flow was introduced in the 1950s by Gibson *et al.* [85] to describe visual stimulus to animals. This method became very popular in the 1980s thanks to Horn and Schunck [86], and Lucas and Kanade [87] who proposed a simple but effective approach to estimate the velocity field using the apparent brightness of images. It has started to be used and theorized in ultrasound in the late 1980s and mid 1990s [88], [89], and has been proven to be robust and reliable even for *in vivo* and

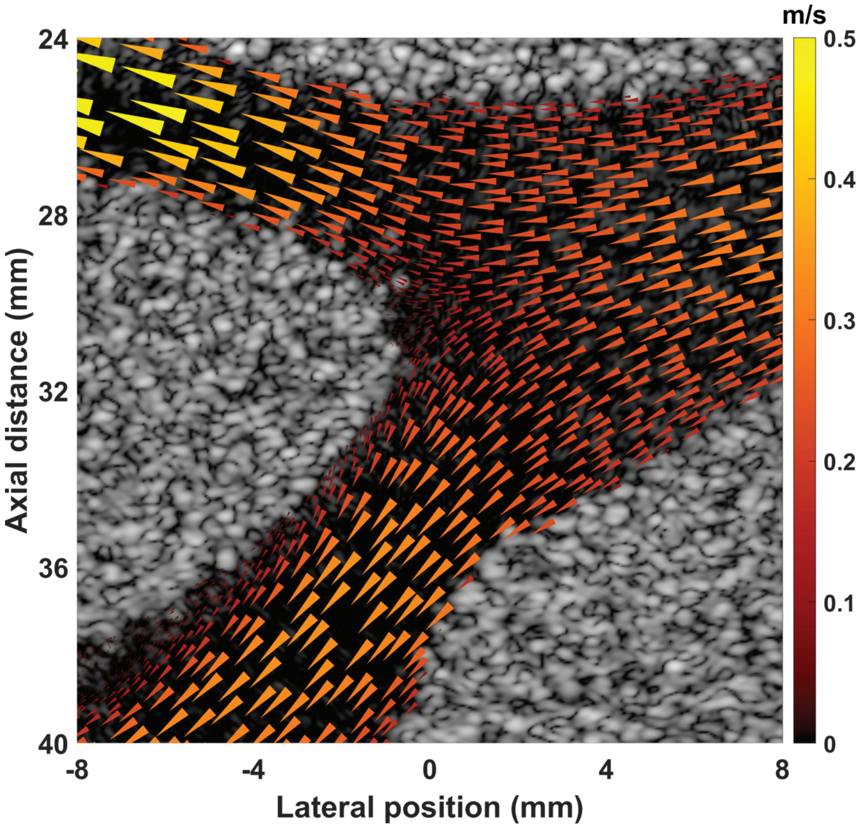

Figure 2.6: Vector flow imaging based on a speckle tracking algorithm in a simulated carotid bifurcation CFD model. Data were provided during the SA-VFI challenge [83], [84] organized by Jensen *et al.* [83], which was a part of the 2018 IEEE International Ultrasonics Symposium in Kobe, Japan. The dynamic range is 40 dB.

medical applications [88], [90].

Optical flow assumes that the brightness of an object is constant over time and its displacement. It means that the observed brightness of any point is constant over time; it is the brightness constraint (Eq. (2.12)):

$$I\left(x+\Delta x, y+\Delta y, t+\Delta t\right)=I\left(x, y, t\right) \tag{2.12}$$

where I is the brightness of the pixel, and Δx and Δy are the displacements of the pixel during Δt. If we assume that the displacement is small, the term can be developed with Taylor series (Eq. (2.13)):

$$I\left(x+\Delta x, y+\Delta y, t+\Delta t\right)=I\left(x, y, t\right)+\frac{\partial I}{\partial x}\Delta x+\frac{\partial I}{\partial y}\Delta y+\frac{\partial I}{\partial t}\Delta t+\sigma\left(\Delta^2\right) \tag{2.13}$$

where $\sigma\left(\Delta^2\right)$ are some high order terms that can be ignored. It appears from Eq. (2.12) that the first-order term in Eq. (2.13) must be zero (Eq. (2.14)):

$$\frac{\partial I}{\partial x}\Delta x+\frac{\partial I}{\partial y}\Delta y+\frac{\partial I}{\partial t}\Delta t=0 \tag{2.14}$$

which can be written in a more dense form (Eq. (2.15)):

$$\nabla I\cdot v=-\frac{\partial I}{\partial t} \tag{2.15}$$

where ∇I is the spatial gradient, v is the velocity components, and $\frac{\partial I}{\partial t}$ is the temporal gradient; both spatial and temporal gradients can be calculated from a set of images. This equation (Eq. (2.15)) is the optical flow constraint equation. However, this problem is not solvable like this since there are two unknowns for one equation; in optics, this problem is known as the aperture problem, and we need, to solve the problem, to use a more specific approach.

The solution proposed by Lucas and Kanade [87] consists of considering a local neighborhood making the assumption they move the same way to find the unknowns using a least-squares criterion. The pixels in the local neighborhood are listed (Eq. (2.16)):

$$\left\{\begin{array}{rcl}
\frac{\partial I\left(p_1\right)}{\partial x}v_x+\frac{\partial I\left(p_1\right)}{\partial y}v_y & = & -\frac{\partial I\left(p_1\right)}{\partial t}\\
\frac{\partial I\left(p_2\right)}{\partial x}v_x+\frac{\partial I\left(p_2\right)}{\partial y}v_y & = & -\frac{\partial I\left(p_2\right)}{\partial t}\\
 & \vdots & \\
\frac{\partial I\left(p_k\right)}{\partial x}v_x+\frac{\partial I\left(p_k\right)}{\partial y}v_y & = & -\frac{\partial I\left(p_k\right)}{\partial t}
\end{array}\right. \tag{2.16}$$

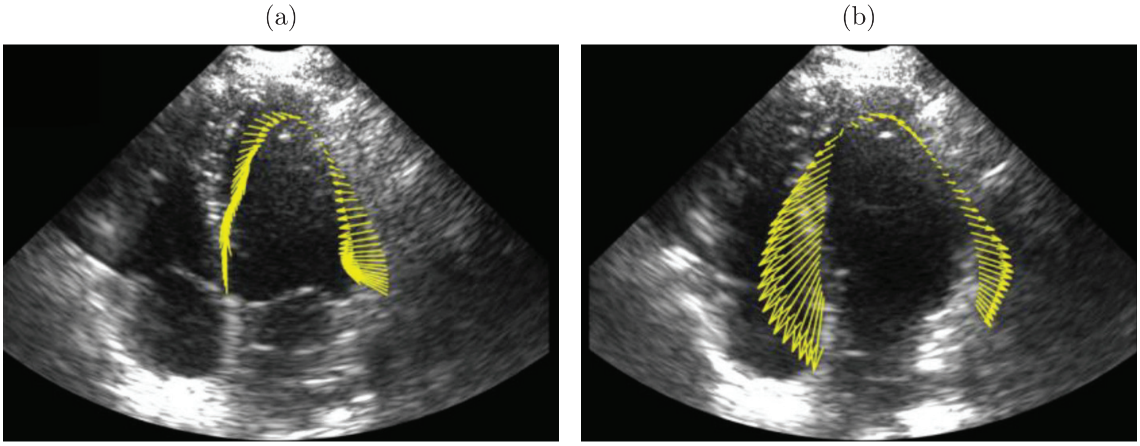

Figure 2.7: Optical flow for evaluation of the myocardium function: (a) systolic phase, and (b) diastolic phase. Optical flow permits here to evaluate the motion of the myocardium during the diastolic and systolic phases. Data were acquired on a healthy volunteer. [(a)-(b): *Adapted, ©2018, IEEE, from* [91]].

where p_k is the kth pixel, and $I(p_k)$ its intensity. The problem can be written in matrix form (Eq. (2.17)):

$$Av = b \tag{2.17}$$

where A is a two-row matrix of the spatial gradients, and b is a one-row matrix of minus the temporal gradient. This problem can be solved using the pseudoinverse approach (Eq. (2.18)):

$$v = \left(A^T A\right)^{-1} A^T b \tag{2.18}$$

where v is the estimate using the least-squares method; ^{T} is the transpose operation, and $^{-1}$ is the inverse operation. It is also possible to use a weighting window to give more importance to the center of the local neighborhood during estimation (Eq. (2.18)):

$$v = \left(A^T W A\right)^{-1} A^T W b \tag{2.19}$$

where W is the weighting function, common windows are Gaussian, Hann, and Hamming functions. This formulation permits to find the displacement from one frame to another to analyze tissue motion (Fig. 2.7).

They are still some possible improvements. For instance, in the case of large displacements, optical flow cannot be used because of the assumption (Eq. (2.13)) that the displacement is small; the most significant measurable displacement with good accuracy is often less than the pixel size in ultrasound imaging. To further improve the estimates and overcome this limit, an iterative refinement can be used where the resolution of the image is reduced to have a small displacement compared to the pixel size; the process is repeated with a thinner resolution until convergence or until the original resolution is reached. Also, affine models can be used to solve the problem instead of a simple translation [92]. In ultrasound, affine models permit to extract the shear and stress from the problem directly and not only the velocity components [93], [94]. One application is for detection and evaluation of atherosclerosis by directly accessing the strain in the plaques [95].

2.3 State of the art on simultaneous wall and flow measurement

As a reminder, in clinical routine, pathology assessments in the arteries are done only with flow imaging using Color Doppler and Doppler spectrum as recommended in the guidelines [96], [97] which are estimated at relatively low frame rates (100 images per second at best).

In the meantime, 2D vector flow measurement at high frame rates has been developed for years in research [24], [26] and has proved to be able to describe complex flow patterns that occur in the vascular system [98]. Moreover, tissue motion estimation has also been studied in research and has shown to be related to the mechanical and geometric properties of the vascular system [43]. Several years ago, a technique able to yield 2D vector flow, named transverse oscillation (TO), was developed by Jensen *et al.* [99]. This technique has been commercially implemented for flow estimation on a medical BK ProFocus UltraView ultrasound scanner (BK Medical Holding Company, Peabody, Massachusetts, United States) which is one of the rare medical systems to provide vector flow imaging [100]. More recently, this method has been extended for tissue motion estimation by Liebgott *et al.* [101]. In clinics, the simultaneous evaluation of wall motion and flow patterns may enable detection of early-stage pathology as well as better patient follow-up. Despite the interest, due to technical limitations, only a few groups have worked on this simultaneous assessment.

In the literature, in 2004 Bambi *et al.* [102] described a novel ultrasound instrument capable of extracting the flow and wall motion along an interrogating ultrasound beam using 128 gates in depth. The ultrasound beam was set to approximately 20°, in regard to the wall, to obtain suitable signals for Doppler analysis; echoes from both the walls and blood were independently processed to obtain in real-time, under some restrictions to allow real-time calculation, both blood flow and wall motion of the common carotid artery in a small population. In post-processing, the wall shear rate and distensibility were also extracted. In 2006, Tortoli *et*

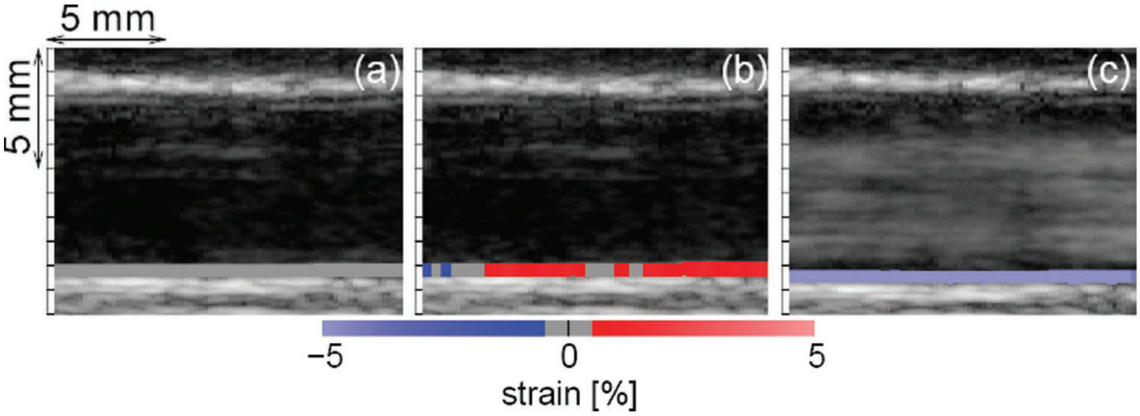

Figure 2.8: Simultaneous imaging of artery-wall strain and blood flow: (a) 0 s, (b) 0.075 s, and (c) 0.15 s after the R-wave of the electrocardiogram. The strain is in percent, and the grayscale level of the flow is enhanced in (c) based on the power of the received signals. The strain is maximum during mid systole (b) which is before the systolic peak of the flow (c). [(a)-(c): *Adapted, © 2008, IEEE, from* [104]].

al. [103] improved the previous system [102] by using a linear probe array to get rid of the unknown beam-to-flow angle. At this end, the probe was divided into two sub-apertures where one was parallel to the wall for a better wall motion estimation. The second sub-aperture was a different angle permitting to obtain Doppler measurements corrected by the real beam-to-flow angle thanks to the two sub-apertures. In 2008 Hasegawa and Kanai [104] proposed a phase-tracking method for a wall coupled with a power Doppler for flow enhancement. Indeed, in this work, the radial strain of a human carotid arterial wall and blood flow were simultaneously imaged *in vivo* at a high frame rate (3 500 images per second) using parallel beamforming (Fig. 2.8). In 2010, Balocco *et al.* [105] used both wall motion and flow information to extract the viscoelastic properties of vessels using a model. In this work, two ultrasound beams were used for estimation of the displacement based on the Doppler spectrum. The same year, Wan *et al.* [106] acquired RF data using a medical scanner at 111 images per second using a limited field of view to extract the blood flow, wall motion, and strain in phantoms and *in vivo* carotid. In 2011, Luo and Konofagou [107] have conducted a feasibility study, using speckle tracking, for both wall and flow estimations on the *in vivo* heart of the mice. By using an ECG gating, they were able to obtain a high frame rate (8 000 images per second) capable of imaging only periodic phenomena due to the long acquisition time (7 minutes in the case presented in the article). Wall and flow velocities were extracted in the heart, and both displayed onto the B-mode images (Fig. 2.9). Lately, Ekroll *et al.* [108] have evaluated a quantitative angle-independent 2D vector velocity estimator providing both vectorial flow and wall motion, but at a relatively low frame rate (63 images per second) due to the duplex mode and compounding.

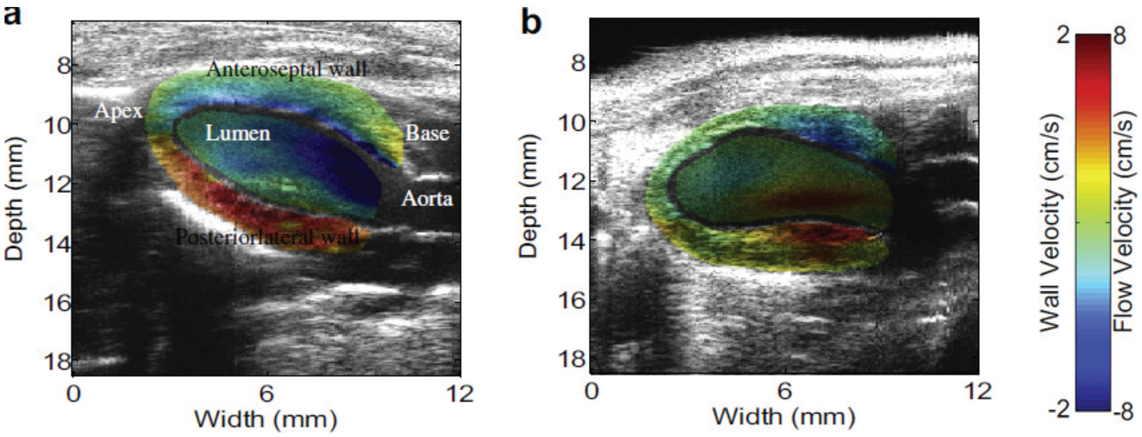

Figure 2.9: 2D images of wall velocity and blood velocity in the systolic phase: (a) of a healthy heart, and (b) of an infarcted heart. Wall velocities are in cm/s while flow velocities are in m/s. In case of the infarcted heart (b) the wall velocity is significantly lower, because of the apical infarction; the flow near the basal region is always positive for the infarcted case (b) while it is always negative in the normal case (a). [(a)-(b): *Adapted, ©2011, UMB, from* [107]].

The technique was evaluated on realistic carotid simulations and *in vivo* carotids. This technique allows the extraction and visualization of the velocity fields from both tissue and flow during cardiac cycles (Fig. 2.10). In 2019, Papadacci *et al.* [109] used a single heartbeat acquisition mode at a high frame rate (5 200 volumes per second) permitting to extract Color Doppler, tissue Doppler, and spectral Doppler. The acquisition scheme, coupled with the estimation algorithm, allowed to extract several Doppler indices using a semi-automatic evaluation approach in three volunteers.

In this state of the art, several studies have been described. A lot of improvements and progress have been made, during the very last years, in research. However, despite the clinical interests, none of these studies were able to provide both vectorial flow and wall motion information to extract potential pathological markers in the cardiovascular system at high frame rates.

2.4 Goals and methods for simultaneous measurement at high frame rates

As previously stated, there is currently no clinical ultrasound mode permitting to extract wall and flow velocity at high frame rates. Moreover, even in research, no studies have been conducted in a clinical environmental coupled with the extraction of pathological markers.

In the first chapter, it has been explained that accessing simultaneously wall motion

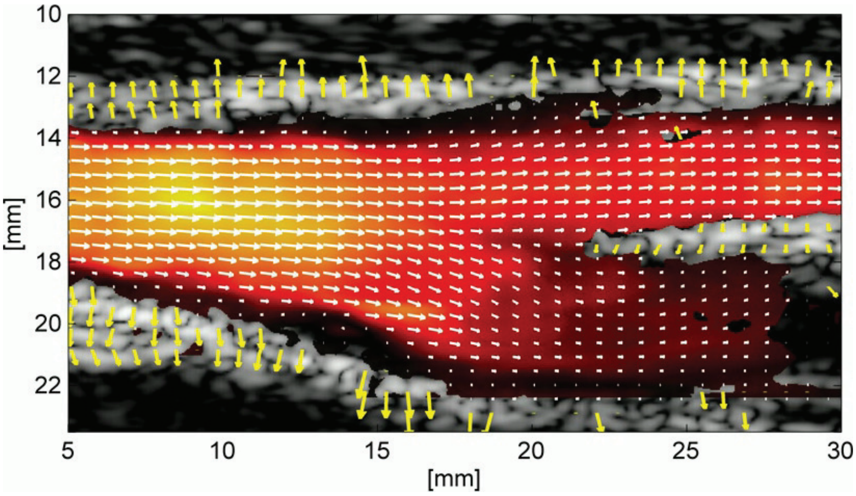

Figure 2.10: 2D tissue and vector flow in a human carotid at systole. Arrows depict the magnitude and direction of the velocities. [*Adapted, ©2013, IEEE, from* [108]].

and flow at high frame rates should be highly relevant for pathology characterization if coupled with appropriate marker measurements. In this chapter, because the transverse oscillation method has been developed for vectorial flow [99] and adapted for tissue motion estimation [101], it seems appropriate to use this technique for simultaneous measurement. Such an approach has been developed in the thesis through tree contribution: *i*) the design of the ultrasound sequence with a 2D motion estimator, *ii*) a new adaptive clutter filtering approach permitting to get rid of the clutter using the tissue information, and *iii*) a clinical proof of concept.

For motion estimation a 2D phase-based estimator is used and presented in the next chapter with the acquisition scheme; in a very similar approach that the one proposed by Kasai *et al.* [66] for the 1D estimation. To achieve a high frame rate, this method is used with plane wave imaging to exceed a thousand images per second in superficial vessels. This approach should permit to yield both vectorial flow and wall motion at high frame rates. Using the tissue velocity measurement, clutter is removed using an advanced adaptive approach described in the fourth chapter permitting to get better flow profiles. Finally, the last chapter presents a clinical proof of concept. Indeed, the technique must also permit to extract pathological markers in a clinical environment.

Chapter 3

Flow and Tissue Motion Estimation at High Frame Rates

The third chapter is the description of the methodology for the simultaneous measurement of flow and tissue motion at high frame rates. Transverse oscillation, which is the main technique used in the thesis, is first described. Then, two different approaches are described for the implementation of the technique. The first one is a time-domain approach which is common in the literature and, the second one is a Fourier filtering approach used in the thesis. A 2D phase-based estimator for assessment of motion, slightly different from classical estimators and adapted to our approach, is then reported. The pipeline of the algorithm is presented and described step by step, including image acquisition and beamforming, tissue motion estimation, and flow estimation. Then, advanced parameters used for validation of the methods are listed and explained. After this methodological part, the estimator is validated based on *in vitro* experiments. A first validation is performed on a commercial flow phantom with a research scanner, and a second validation is done on an in-house tissue and flow phantom explicitly created for the validation. The third chapter concludes with a discussion on the *in vitro* experiments and the limits for an application on *in vivo* carotids.

There are three proceedings at *IEEE International Ultrasonics Symposium* as evidence of the scientific contribution: “Estimation of arterial wall motion using ultrafast imaging and transverse oscillations: in vivo study” (2016), “Simultaneous pulse wave and flow estimation at high-framerate using plane wave and transverse oscillation on carotid phantom” (2017), and “Simultaneous tissue and flow estimation at high frame rate using plane wave and transverse oscillation on in vivo carotid” (2018).

3.1 Transverse oscillation

The first section of the third chapter presents transverse oscillation. This section is broken down into four subsections: concept of transverse oscillation, creation of transverse oscillation by apodization, creation of transverse oscillation by Fourier filtering, and 2D phase-based estimator. In the following, the transverse oscillation introduction approach is described with the estimator permitting to extract the 2D vector velocity field from plane wave acquisitions.

3.1.1 Concept of transverse oscillation

Transverse oscillation (TO) permits to create a 2D oscillation pattern in ultrasound images. This pattern permits to develop 2D phase-based motion estimation algorithms, more accurate than more conventional amplitude-based algorithms. Indeed, after TO introduction, the signals contain a 2D controlled phase that can be extracted to estimate velocity fields.

TO was first described and have been developed by Jensen and Munk in 1998 [99]. A few years later, in 2001, Jensen proposed a new 2D phase-based estimator dedicated to this technique [110]. The idea is to modify the aperture of the probe in transmit or receive to create the 2D pattern; a similar approach was proposed in 1998 by Anderson [111] using spatial quadrature sampling. To understand how this pattern can be created, Jensen and Munk [99] proposed to consider two finite plane waves sent by a transducer (Fig. 3.1). In Fig. 3.1 the 2D pattern is created by the crossing of the two finite plane waves. This approach can be done with one transducer using two subapertures or two distinct ones. By taking a closer look at the intersection (Fig. 3.2), we can extract the new axial and lateral wavelengths. Indeed, by trigonometrical relationships, we can express the axial wavelength as (Eq. (3.1)):

$$\lambda_z = \frac{\lambda}{cos\left(\theta\right)} \tag{3.1}$$

where λ_z is the axial wavelength, λ is the ultrasound wavelength, and θ the angle of the transmit plane waves. The tangent can be written as (Eq. (3.2)):

$$tan\left(\theta\right) = \frac{\lambda_z}{\lambda_x} \tag{3.2}$$

where λ_x is the lateral wavelength. Combining Eq. (3.1) and Eq. (3.2), and using the definition of the tangent function which is the division of the cosine function by the sine function, we can express the lateral wavelength; the two wavelengths can

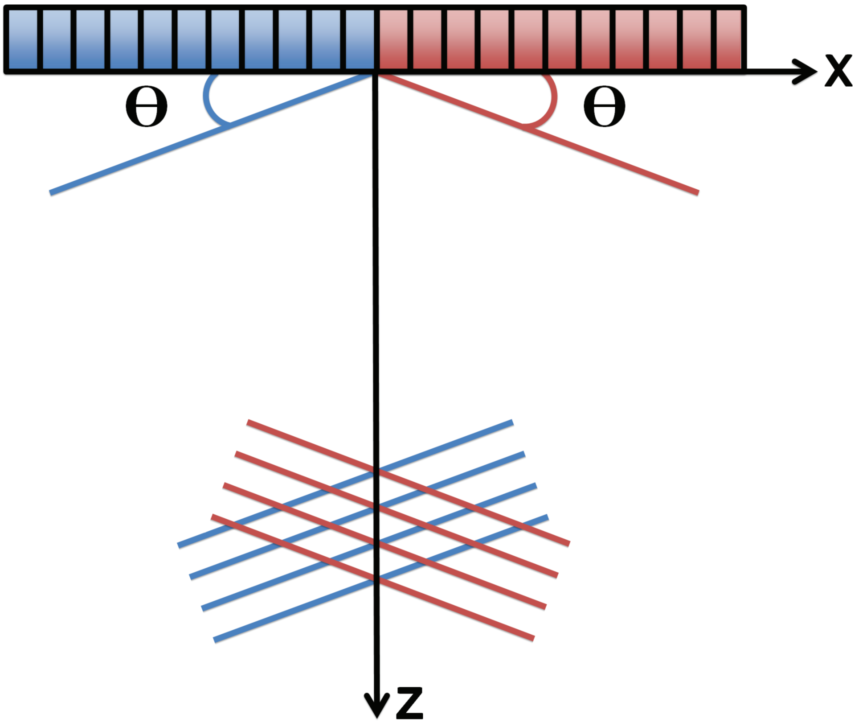

Figure 3.1: Crossing of two finite plane waves. When the two plane waves cross each other, they create a 2D oscillation pattern. [*Reproduced and adapted, ©1998, IEEE, from* [99]].

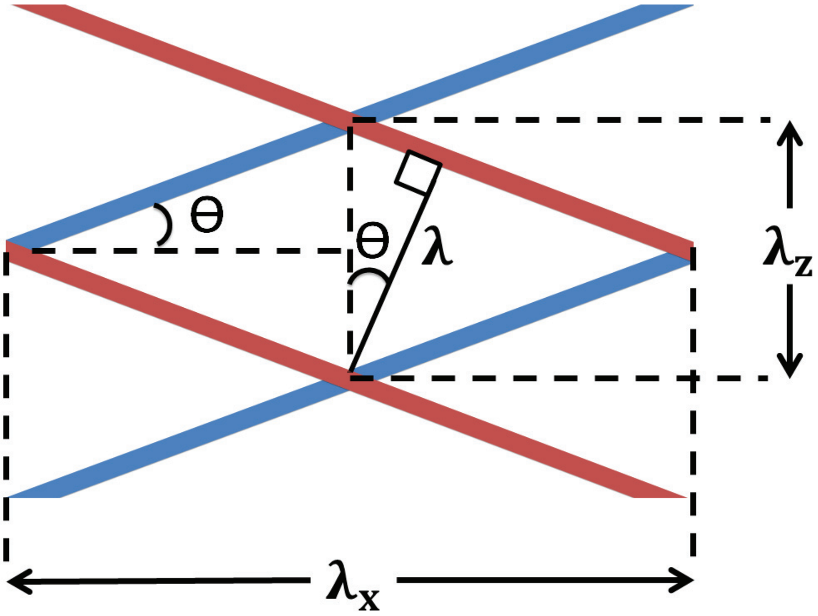

Figure 3.2: Close-up view of the crossing of two finite plane waves. The interference where the two waves cross each other created axial and lateral wavelengths, both different from the ultrasound wavelength. [*Reproduced and adapted, ©1998, IEEE, from* [99]].

finally be written as (Eq. (3.3)):

$$\begin{cases} \lambda_z & = \dfrac{\lambda}{cos\left(\theta\right)} \\ \lambda_x & = \dfrac{\lambda}{sin\left(\theta\right)} \end{cases} \tag{3.3}$$

This crossing of two finite plane waves is behind the concept of TO. In practice, such perfect plane waves cannot be transmitted by a transducer, but this illustration helps to understand the concept of transverse oscillation that can be understood as a crossing of different pressure waves.

3.1.2 Creation of transverse oscillation by apodization

TO can be created by working on the modulation of the point spread function (PSF) of the system. The PSF can be decomposed into the axial and lateral PSF (Eq. (3.4)):

$$h\left(x, z\right) = h_x\left(x\right) \circledast h_z\left(z\right) \tag{3.4}$$

where $h\left(x, z\right)$ is the 2D PSF, h_x is the lateral PSF, and h_z the axial PSF; $\circledast$ is the convolution operation. From the optics, supposing a monochromatic wave, the lateral PSF is the Fourier transform of the aperture under the Fraunhofer assumption which is valid at the focal point (in transmit or receive) (Eq. (3.5)) [112]:

$$h_x\left(x\right) = \mathscr{F}\left\{w\left(\frac{x}{\lambda_z z_f}\right)\right\} \tag{3.5}$$

where $\mathscr{F}$ is the Fourier transform, w is the aperture at the depth z_f. We want to have a lateral PSF expressed as (Eq. (3.6)):

$$h\left(x\right) = g\left(x\right)\ cos\left(2\pi\frac{x}{\lambda_x}\right) \tag{3.6}$$

where $g\left(x\right)$ is a Gaussian function corresponding to the modulation of the envelope. Let us consider the Gaussian function as (Eq. (3.7)):

$$g\left(x\right) = exp\left(\frac{-x^2}{2\sigma_x^2}\right) \tag{3.7}$$

where σ_x is the standard deviation of the Gaussian function; the Gaussian function is designed as a filter function and not as a probability density. The aperture corresponding to this lateral PSF is then (Eq. (3.8)):

$$w\left(x\right)=\frac{1}{2}exp\left(\frac{-x^{2}}{2\sigma_{0}^{2}}\right)\circledast\left(\delta\left(x-x_{0}\right)+\delta\left(x+x_{0}\right)\right) \tag{3.8}$$

where σ_0 is the standard deviation of the Gaussian function, and x_0 the lateral position of the Gaussian peaks; $\circledast$ is the convolution operation. The parameters of the aperture are related to those of the lateral PSF (Eq. (3.9)):

$$\begin{cases} x_{0} & =z\frac{\lambda_{z}}{\lambda_{x}}\\ \sigma_{0} & =z\frac{\sqrt{2}\lambda_{z}}{\sigma_{x}} \end{cases} \tag{3.9}$$

For any Gaussian function, the standard deviation is related to the full width at half maximum (FWHM) as (Eq. (3.10)):

$$\sigma=\frac{\gamma}{2\sqrt{2ln\left(2\right)}} \tag{3.10}$$

where σ is the standard deviation of the Gaussian function, and γ the FWHM. It appears from Eq. (3.9) that the lateral wavelength is dependent on the focal depth. The PSF should be modulated in transmit or receive since the pressure wave passes through the transducer two times. Indeed, the two-way impulse response of the transducer is the convolution of the impulse response in transmit and receive. If the modulation is done in transmit, the lateral wavelength oscillation changes with depth. However, if done in receive, the shape of the aperture can be depth-dependent to have a constant lateral wavelength oscillation in the medium. The deeper the depth, the more the Gaussian peaks are spread away from the center of the transducer. Using this technique to introduce TO, we do not have any crossing of several waves like in Fig. 3.1; the axial wavelength is the same as the ultrasound wavelength. An example is provided in Fig. 3.3 where the aperture is a double Gaussian function (Fig. 3.3a) to create TO in the medium (Fig. 3.3b). This technique has been implemented in real-time on two research scanners: ULA-OP 64 system (MSDLab, Florence, Italy) [113] and ULA-OP 256 system (MSDLab, Florence, Italy) [114]; Fig. 3.4 shows a dual real-time implementation of a standard plane wave transmission and of a plane wave acquisition with TO using the ULA-OP 256 system.

This novel technique has been developed for flow [99], [110], and Udesen and Jensen investigated the reliability of this approach [115], [116]. They have demonstrated that the method was reliable for vector flow imaging, with bias and standard deviation as smaller as the vessel is parallel to the probe. For vascular imaging, since

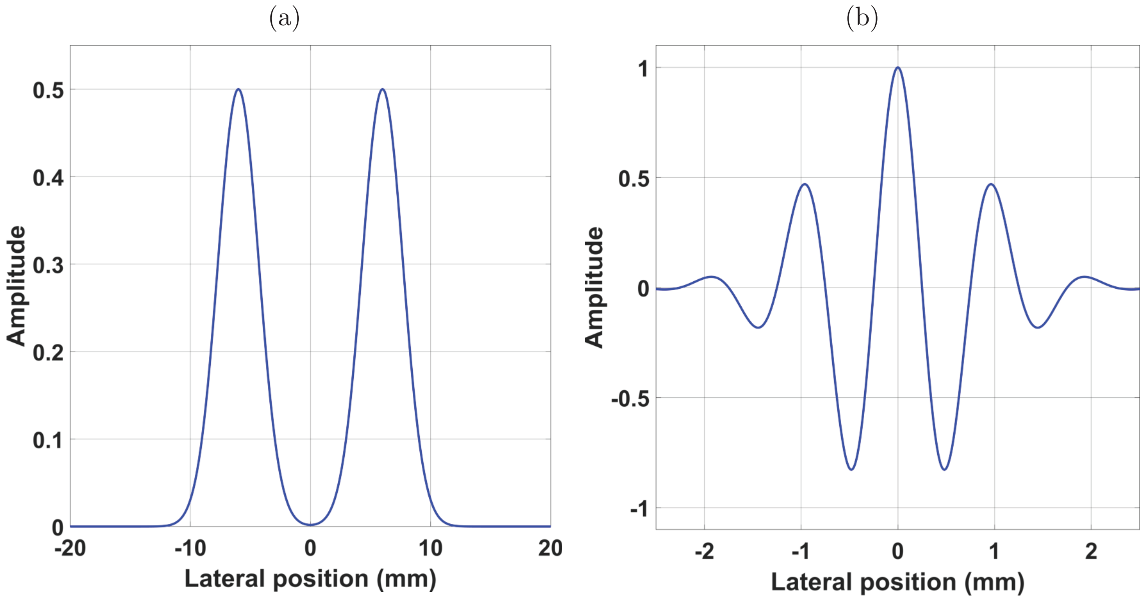

Figure 3.3: Aperture applied on a transducer to create transverse oscillation: (a) aperture applied on the transducer, and (b) lateral PSF created in the medium. TO is introduced at a depth of 2 cm with a lateral wavelength of 1 mm, and the FWHM is 2 mm; ultrasound frequency is 5 MHz with a speed of sound of 1 500 m/s.

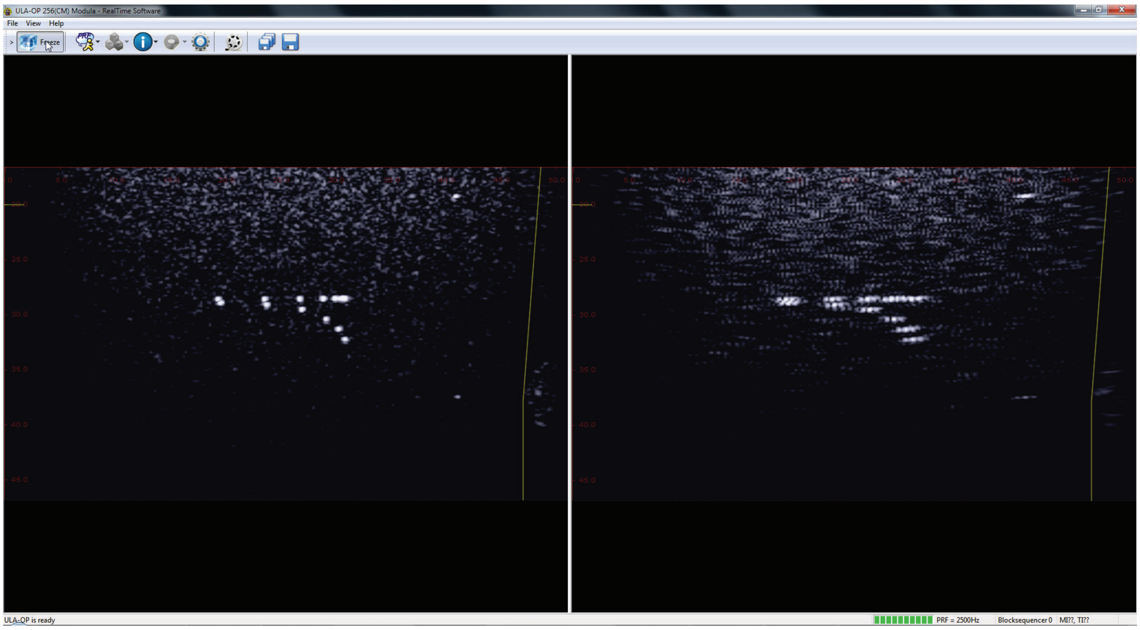

Figure 3.4: Dual real-time implementation of transverse oscillation: (left) B-mode image with a standard plane wave acquisition, and (right) B-mode image with plane wave acquisition with TO. Acquisitions were performed on a calibration phantom (CIRS 054GS, CIRS, Norfolk, Virginia, United States); in the right panel, TO was introduced with a wavelength of 1 mm, and an FWHM of 2 mm. With TO the PSF presents a lateral oscillation, clearly perceptible on the wires.

vessels are mostly parallel to the surface of the skin, we have this configuration. Since the method was reliable for flow imaging, Liebgott *et al.* have modified the approach for tissue motion estimation [101], [117], [118]. Their results were similar to flow imaging; the method was also relevant for tissue imaging. This method has been applied *in vivo* [119], [120], and implemented on a medical BK ProFocus UltraView ultrasound scanner (BK Medical Holding Company, Peabody, Massachusetts, United States) [100]. In the meantime, in research, the method has also been used with tissue imaging for elastography [121], and for wall motion extraction [122]–[124].

3.1.3 Creation of transverse oscillation by Fourier filtering

Previously, we saw that transverse oscillation can be introduced with a specific aperture in transmit or receive. If done in transmit, there is no way back to adjust a parameter. While, in receive, it is possible to redo the aperture and beamforming if needed to change, for instance, the wavelength of transverse oscillation; it is possible only is the raw signals were saved. Changing the TO wavelength is useful in case of aliasing that can occur in pathological vessels in case of high flow velocities. Moreover, due to the poor lateral resolution of TO images, it is still necessary to provide a standard B-mode image for clinicians, using a classic aperture for beamforming. It means that, in the better case, two sets of images should be provided. To get rid of those issues, and to propose an alternative, Liebgott and Varray [121], [125] proposed to filter the f-k spectrum of beamformed images to select a lateral frequency. This approach, done in the Fourier domain, is inexpensive and has been described by Salles *et al.* [126]. If we consider the f-k spectrum of a beamformed ultrasound image, we can use a Gaussian filter along the lateral axis to keep one lateral frequency (Eq. (3.11)):

$$\Omega\left(f_x\right) = exp\left(-2\sigma_x^2 f_x^2\right) \circledast \left(\delta\left(f_x - \frac{1}{\lambda_x}\right) + \delta\left(f_x + \frac{1}{\lambda_x}\right)\right) \tag{3.11}$$

where $\Omega\left(f_x\right)$ is the lateral frequency of the Gaussian filter, σ_x the standard deviation of the filter, and λ_x the lateral wavelength; $\circledast$ is the convolution operation. An example of TO introduction using this approach is provided in Fig. 3.5. The B-mode image after TO introduction (Fig. 3.5b) contains a lateral oscillatory pattern that can be seen on the wires. The f-k spectrum of the image with TO (Fig. 3.5d) contains four signal regions due to the natural axial oscillation of the RF images and the introduced lateral oscillation. This approach has since been investigated by Jensen *et al.* [127] for flow imaging and by Salles *et al.* [123], [124] for tissue imaging. For both applications, the approach was relevant with good results in both *in vitro*

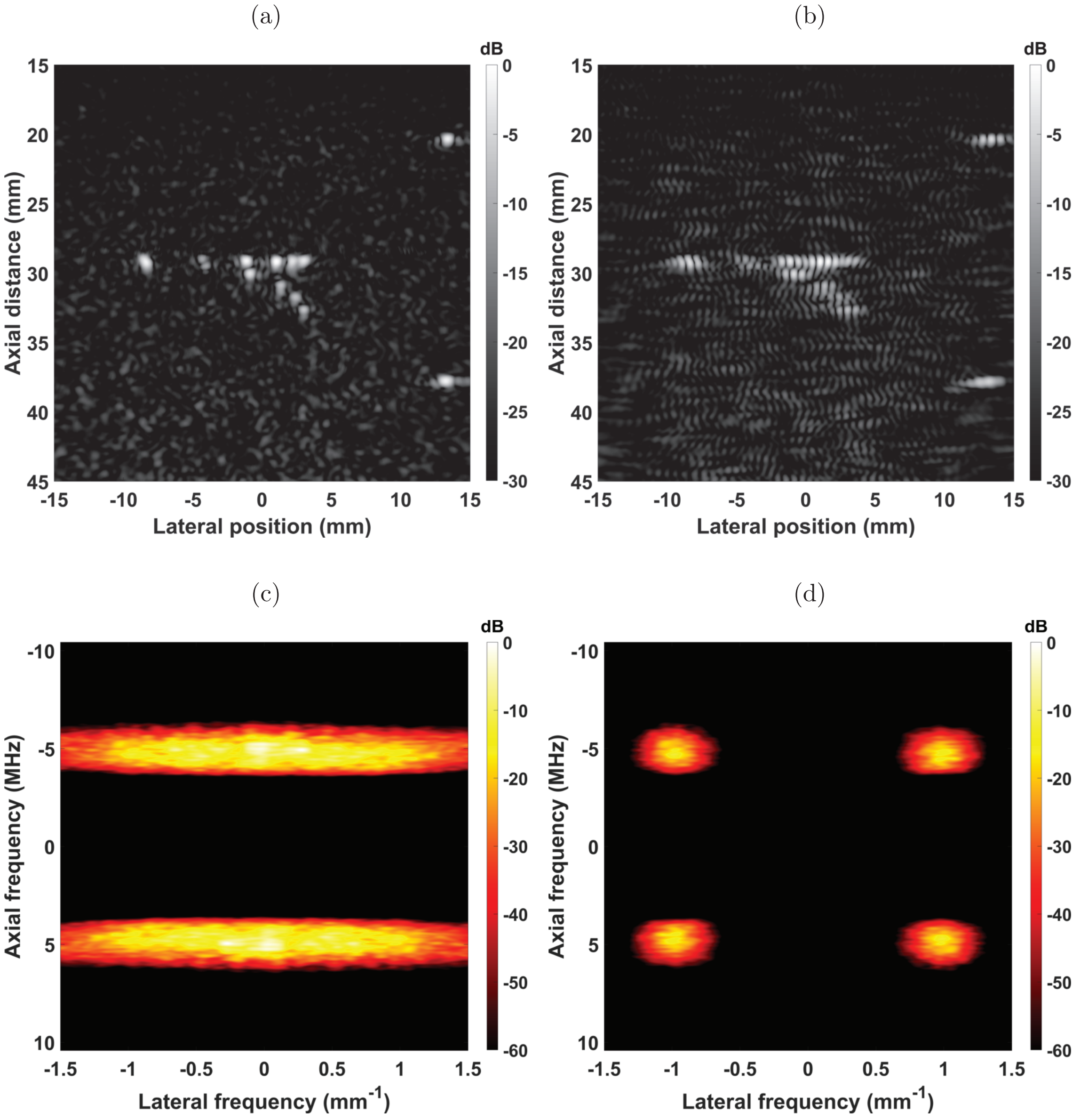

Figure 3.5: Introduction of transverse oscillation in the Fourier domain: (a) B-mode image, (b) B-mode image with TO, (c) f-k spectrum of (a), and (d) f-k spectrum of (b). Acquisitions were performed on a calibration phantom (CIRS 054GS, CIRS, Norfolk, Virginia, United States) with a Verasonics Vantage$^{\mathrm{TM}}$ 256 system (Verasonics, Redmond, Washington, United States), TO was introduced with a wavelength of 1 mm, and an FWHM of 2 mm.

and *in vivo* applications. This filtering is just another inexpensive technique for TO introduction using a different approach.

3.1.4 2D phase-based estimator

Since Kasai *et al.* [66] in 1985 several phase-based estimators have been proposed for flow and tissue imaging based on 1D or 2D phase estimates [110], [128]–[131]. Specific estimators have been proposed for transverse oscillation by Jensen [110], and by Basarab *et al.* [131]. Jensen [110] proposed to use a modified version of the complex autocorrelation to yield the transverse and axial velocity components independently. While Basarab *et al.* [131] developed a phase-based block matching technique permitting to get rid of phase jumps. In the following, we propose to use a 2D phase-based estimation technique with a similar approach to the one developed by Kasai *et al.* [66] using an extension of the Hilbert transform to the n-dimensional case [132], [133] to extract analytic signals.

As previously showed (Fig. 3.5d) the f-k spectrum of an image with TO contains four spots due to the axial and lateral wavelengths. The Hahn's approach [132] consists of extracting two single quadrants of this spectrum to get the corresponding analytic signals [133]. This technique assumes that the 2D oscillation can be described as the product of two 1D oscillation signals. From another point of view, each of those analytic signals can be interpreted as a signal from a virtual sub-aperture. Because of the symmetry of the spectrum, two adjacent quadrants must be extracted; hereby, we are using the two top regions corresponding to the negative axial and negative lateral frequencies, and the negative axial and positive lateral frequencies, respectively. Those quadrants are extracted using a simple mask multiplication in the Fourier domain. An example is provided in Fig. 3.6 where a 2D image (Fig. 3.6a) was decomposed into two complex analytic signals (Figs. 3.6b to 3.6e). The phases of the two analytic signals (Figs. 3.6b and 3.6c) shows two different 1D orientations that are the decomposition of the original image (Fig. 3.6a). The analytic signals have the same magnitudes (Figs. 3.6d and 3.6e), they differ only by their phases (Figs. 3.6b and 3.6c).

To extract velocity components, let us consider a spatial point in the TO image, the signal from this point can be written as (Eq. (3.12)):

$$s\left(t\right)=A\left(t\right)cos\left(2\pi f_x\left(x+dx\left(t\right)\right)\right)cos\left(2\pi f_z\left(z+dz\left(t\right)\right)\right) \tag{3.12}$$

where A is an amplitude term, f_x and f_s are respectively the axial and lateral frequencies, and dz and dx are respectively the axial and lateral displacements. The

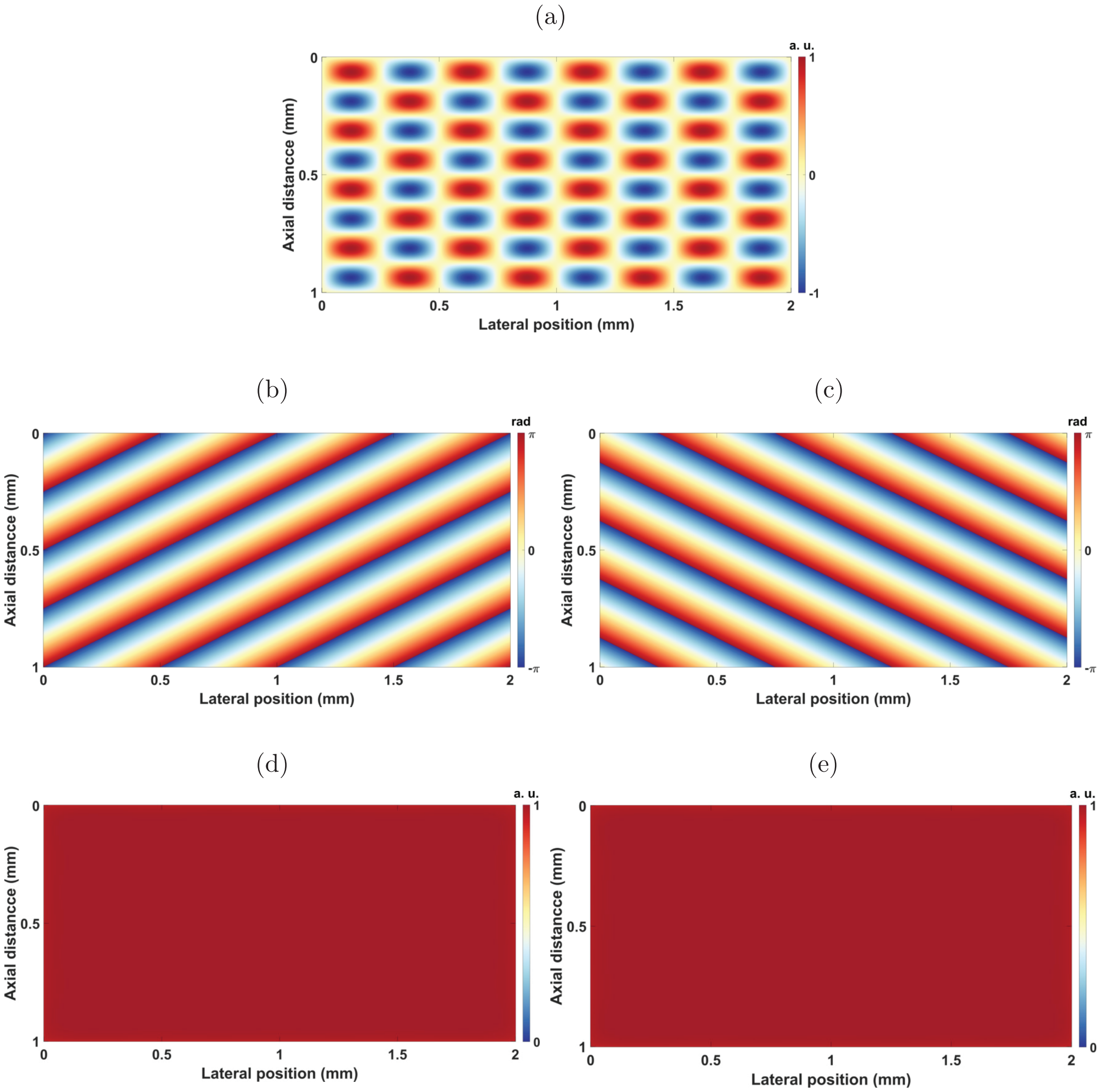

Figure 3.6: 2D analytic decomposition of a 2D image: (a) original image with a 2D oscillation pattern, (b) phase of the first analytic signal, (c) phase of the second analytic signal, (d) magnitude of the first analytic signal, and (e) magnitude of the second analytic signal. The product of two analytic signals returns the original image.

phase of the analytic signals are (Eq. (3.13)):

$$\begin{cases} \Phi^{I}(t) = 2\pi f_x \left(x + dx(t)\right) + 2\pi f_z \left(z + dz(t)\right) \\ \Phi^{II}(t) = -2\pi f_x \left(x + dx(t)\right) + 2\pi f_z \left(z + dz(t)\right) \end{cases} \tag{3.13}$$

where Φ^I and Φ^{II} are the phases of the first and second analytic signals, respectively. We can define the phases differences as (Eq. (3.14)):

$$\begin{cases} \Delta\Phi^{I}(t) = \Phi^{I}(t+\tau) - \Phi^{I}(t) \\ \Delta\Phi^{II}(t) = \Phi^{II}(t+\tau) - \Phi^{II}(t) \end{cases} \tag{3.14}$$

where $\Delta\Phi^I$ and $\Delta\Phi^{II}$ are respectively the phase shifts from the first and second analytic signals, and τ is a lag for the estimation. Those phase shifts can be written as (Eq. (3.15)):

$$\begin{cases} \Delta\Phi^{I}(t) = 2\pi f_x \Delta x(t) + 2\pi f_z \Delta z(t) \\ \Delta\Phi^{II}(t) = -2\pi f_x \Delta x(t) + 2\pi f_z \Delta z(t) \end{cases} \tag{3.15}$$

where Δx and Δz are respectively the displacement from t to $t+\tau$. The axial and lateral velocity components can be recovered using a projection of the phase shifts (Eq. (3.16)):

$$\begin{cases} v_z = \dfrac{PRF}{\tau} \dfrac{c}{4f_z} \dfrac{\Delta\hat{\Phi}^{I}(\tau) + \Delta\hat{\Phi}^{II}(\tau)}{\pi} \\ v_x = \dfrac{PRF}{\tau} \dfrac{c}{4f_x} \dfrac{\Delta\hat{\Phi}^{I}(\tau) - \Delta\hat{\Phi}^{II}(\tau)}{\pi} \end{cases} \tag{3.16}$$

where $\Delta\hat{\Phi}^I$ and $\Delta\hat{\Phi}^{II}$ are respectively the estimated phase shifts from the first and second analytic signals, and v_z and v_x are respectively the axial and lateral velocity components. Here, we are assuming no aliasing and a constant velocity in the observation window to get rid of the τ-dependence on the left side. Like in the 1D estimation, a sliding window with a fixed ensemble length can be used to get the velocity as a function of time. The phase shifts can be estimated using the same estimator as Kasai *et al.* [66] proposed (Eq. (3.17)):

$$\begin{cases} \Delta\hat{\Phi}^{I}(\tau) = atan\left(\dfrac{\mathscr{I}\left\{\hat{R}^{I}(\tau)\right\}}{\mathscr{R}\left\{\hat{R}^{I}(\tau)\right\}}\right) \\ \Delta\hat{\Phi}^{II}(\tau) = atan\left(\dfrac{\mathscr{I}\left\{\hat{R}^{II}(\tau)\right\}}{\mathscr{R}\left\{\hat{R}^{II}(\tau)\right\}}\right) \end{cases} \tag{3.17}$$

where $\hat{R}^I$ and $\hat{R}^{II}$ are respectively the complex autocorrelation of the first and second analytic signals; $\mathscr{I}$ and $\mathscr{R}$ are respectively the imaginary and real functions, and $atan$ is the inverse tangent function. Spatial filtering of the complex autocorrelation estimates is usually performed before velocity estimation to reduce noise in the estimated phase shifts.

To sum up, TO images are decomposed into analytic signals thanks to Hahn's approach [132]; this approach was already used by Basarab *et al.* with their estimator [131]. Then, the phase shift of each analytic signal is estimated based on the complex autocorrelation as proposed by Kasai *et al.* [66]. Finally, velocity components are recovered by the projection of those phase shifts, using the acquisition parameters, in a similar way proposed by Jensen [110].

3.2 Procedure

The second section of the third chapter presents the procedure. This section is broken down into five subsections: general approach, image acquisition and beamforming, tissue motion estimation, flow estimation, and advanced parameters. In the following, the procedure is described with the workflow in detail permitting to get both wall and flow estimates at high frame rate from plane wave acquisitions.

3.2.1 General approach

Overall the estimation process allowing to obtain estimates with parameters from raw signals can be broken down in four steps (Fig. 3.7):

1. **Beamforming**: Correct the time of flight of pressure waves from the scatterers to the probe.
2. **Envelope detection**: Extract the envelope from the beamformed signals to provide B-mode images.
3. **Tissue motion estimation**: Estimate tissue velocity from beamformed signals.
4. **Flow estimation**: Estimate flow from beamformed signals, tissue velocity can be used as an input for clutter filtering.

This flow chart is a simplified version of the overall algorithm. Indeed, each process is composed of several steps, but it permits to identify the main parts of the processing stream. From all the estimates and B-mode images, several parameters can be

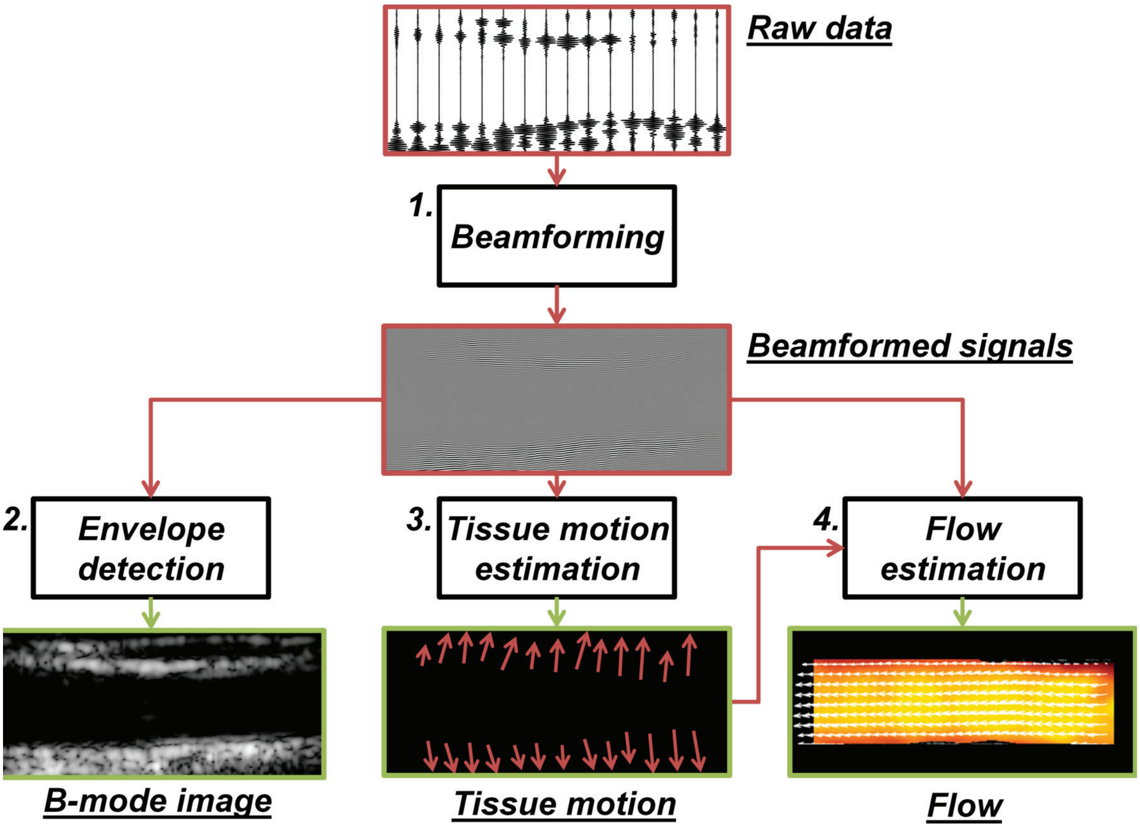

Figure 3.7: Simplified flow chart diagram of the estimation process. Red boxes/arrows are inputs, black boxes are processes, and green boxes/arrows are outputs.

extracted to characterize the medium based on both quantitative and qualitative inspections of the outputs.

3.2.2 Image acquisition and beamforming

As previously stated, plane wave imaging permits to insonify the medium at high frame rates. Since the goal is to study both wall and flow motions with a high temporal resolution, to detect the fastest phenomena, acquisitions are performed using plane waves. The transmit apodization, transmit pulse, and voltage must be chosen in accordance with the medium. Then, raw signals from ultrasound acquisitions need to be beamformed to compensate for the time of flight of pressure waves. For this purpose, a standard delay-and-sum algorithm is used. In addition to receive apodization, which reduces side lobe effects, the f-number has to be set correctly. Indeed, due to both the directivity and noise in the raw signals, full aperture beamforming is not often relevant; especially for the flow, which has low power compared to tissue. However, define a precise criterion for the f-number is difficult; simulations are often used but are acquisition dependent, or the f-number is based on the experience of the operator. It is possible to use a criterion for setting the f-number. As explained in the previous chapter, the f-number can be written as (Eq. (3.18)):

$$F_{\#} = \frac{D}{L} \tag{3.18}$$

where L is the total width of the active aperture, and D is the distance to the focus. The f-number can be expressed by trigonometrical relationships as (Eq. (3.19)):

$$F_{\#} = \frac{1}{2\, tan(\theta)} \tag{3.19}$$

where θ is the maximal angle in the aperture. However, a piezoelectric element has a directivity that can be written as (Eq. (3.20) [134]:

$$d(\theta) = sinc\left(\frac{\pi\, w}{\lambda}\, sin(\theta)\right) \tag{3.20}$$

where $d(\theta)$ is the directivity as a function of the angle θ, w is the element width, and λ is the wavelength; the *sinc* function is cardinal sine defined as the sinusoidal function divided by its argument without any normalization The baffle is assumed to be rigid, in case of a soft baffle assumption the directivity is multiplied by the cosine of the angle; but, for small angles the variation from one assumption to another is insignificant. The general solution to Eq. (3.20) in a range $-\pi/2$ to $\pi/2$ for a given value of the directivity is (Eq. (3.21)):

$$\theta_{-n\,dB} = asin\left(\Omega_{-n\,dB}\,\frac{\lambda}{w}\right) \tag{3.21}$$

where $\theta_{-n\,dB}$ is the angle aperture fixed when the directivity reaches $-n$ dB, the term $\Omega_{-n\,dB}$ can only be estimated numerically and do not have an analytic expression due to the cardinal sine. By expressing the f-number with the limit angle of the aperture, we obtain a limit f-number (Eq. (3.22)) as:

$$F_{\#_{-n\,dB}} = \frac{1}{2\,tan\left(asin\left(\Omega_{-n\,dB}\,\frac{\lambda}{w}\right)\right)} \tag{3.22}$$

For instance, the value for $\Omega_{-n\,dB}$ at -3 dB, and -6 dB are approximately 0.443, and 0.603 respectively. The optimal f-number using a -6 dB threshold (when the directivity drops below -6 dB) is 1.01 using a standard linear probe array with a width of 300 μm at a maximal frequency of 6.5 MHz (central frequency at 5 MHz with a bandwidth of 60 %), and speed of sound of 1 540 m/s. Then, we have an expression with a physical meaning to set the f-number, and in case of *in vivo* or noisy acquisitions, this expression can be used to fix the f-number depending on a directivity threshold. It also shows that the full aperture is often not recommended due to the physical properties of the piezoelectric elements.

In summary, plane wave acquisitions are used to reach high frame rates with transmit signal and apodization in accordance with the medium of interest and its backscattered energy. Raw signals are beamformed using a DAS algorithm with both f-number and received apodization depending on the noise power. An *in vitro* phantom acquisition under perfect experimental conditions can be beamformed with a full aperture while a deep vessel in a patient for flow imaging should be imaged with a smaller aperture.

3.2.3 Tissue motion estimation

For tissue motion extraction, the 2D phase-based estimator is used. Since tissue energy is dominant in the received signals, no specific pre-processing is needed to isolate tissue signals from other backscatter sources. The tissue itself is slowly moving with velocity in the range of the cm/s. However, the wall can be subject to sudden changes in velocity, in particular, due to pulse wave propagating at speed in the range of the m/s [40], [44], [124]. Consequently, it is needed to not over smooth in both space and time to be able to extract fast phenomena happening in tissue.

Also, a high frame rate is required for PWV extraction, which is the case here with the plane wave acquisition scheme.

3.2.4 Flow estimation

For flow extraction, the same estimator than for tissue estimation is used. However, because the flow-to-tissue ratio is low, it is needed to clutter filter the received signal before flow estimation. Clutter filtering consists of removing stationary and quasi-stationary signals, which are not due to blood from the received signals [135], [136]. In case of high noise intensity or high wall velocity, clutter can be in the same velocity range as blood signal and strongly exceed the intensity of the blood. Clutter filtering is widely described in the next chapter with different approaches. Because validation of the sequence has been performed with *in vitro* phantoms under good experimental conditions with high SNR, the clutter filtering is not quite an issue in this chapter. Consequently, standard techniques based on the assumption that the velocity of the wall is low compared to flow have been used with simple criteria. After clutter filtering, flow can be extracted in the same way as tissue. However, SNR is not as good as tissue; consequently, both ensemble length and spatial averaging should be considered to reduce noise in the estimates.

3.2.5 Advanced parameters

Based on flow and tissue motion estimates, several parameters can be extracted. In the first chapter, wall shear rate and pulse wave velocity have been described as good potential pathological markers. Hereby, validation of the flow is done based on flow profiles since the vessel has a regular geometry (linear tube). Indeed, using phantoms with a linear geometry, flow profiles are highly predictable.

Concerning tissue motion, validation is based on PWV measurement for the realistic carotid phantom that is described in this chapter. PWV is estimated in the wall of the carotid phantom during the time based on the tissue estimates; such techniques have been proved to have a good correlation with global PWV measurement used in clinics with pressure captors on the carotid and femoral arteries [137]. At this end, an acceleration map is calculated along the vessel wall (Fig. 3.8). For each point along the vessel, the passage of the pulse wave is defined as the position of the maximum peak of the radial acceleration of the wall; this maximum corresponds to the foot of the wall displacement, at the very beginning of the cycle. This temporal point of reference, the acceleration peak, is different for each position along the wall due to the propagation of the pulse wave. Finally, the PWV can be estimated with

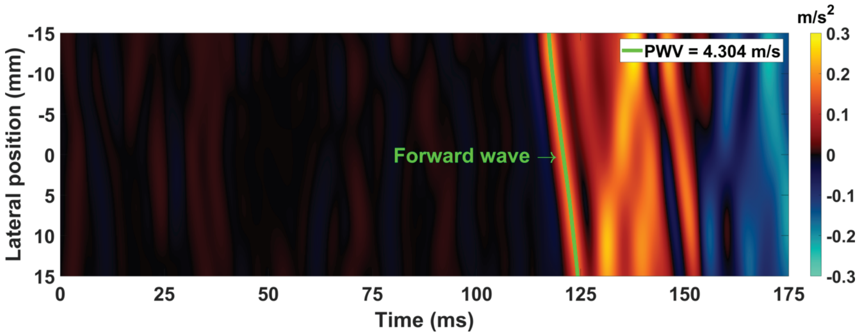

Figure 3.8: Example of acceleration map of the vessel wall for PWV estimation. The slope of the acceleration peak corresponds to a pulse wave propagation; this wave is the forward wave which occurs at the very beginning of the cardiac cycle. A PVA phantom was used with an in-house flow system; this map was estimated on the upper wall.

linear regression (slope of the line) of those passage points. For instance, in Fig. 3.8 the estimated PWV is 4.304 m/s.

3.3 Experiments

The third section of the third chapter presents the experiments. This section is broken down into two subsections: validation of the estimator, and realistic carotid phantom. In the following, the estimator is validated *in vitro* with a commercial flow phantom and an in-house carotid phantom permitting to validate both wall and flow aspects.

3.3.1 Validation of the estimator

3.3.1.1 Material and methods

To validate the estimator a flow phantom (Gammex Doppler 403$^{\text{TM}}$, Gammex, Middleton, Wisconsin, United States) using a plane wave imaging mode with a Verasonics Vantage$^{\text{TM}}$ 256 system (Verasonics, Redmond, Washington, United States) was imaged at continuous low (maximum flow at 7.5 cm/s) and high (maximum flow at 40 cm/s) flow velocities. The low flow velocity corresponds to the minimal achievable velocity with good confidence in the accuracy of the calibration. The high flow velocity is the highest achievable velocity with a parabolic flow profile regarding the distance from the inlet. The beam-to-flow angle was about 12.5° on a 5 mm diameter vessel giving a large lateral velocity compared to the axial component. Acquisition parameters are described in Tab. 3.1, while estimation

Table 3.1: Acquisition parameters for the validation of the estimator

Parameter	**Value**
Probe	L 7-4, ATL Phillips
Number of elements	128
Pitch	298 μm
Central frequency	5.208 MHz
Sampling frequency	20.832 MHz
Excitation pulse	5-cycle sinusoidal
Pulse apodization	None (rectangular)
Speed of sound	1 540 m/s
Pulse repetition frequency	2 000 Hz
Compounding	No (single plane wave)
Steering angle	0° (horizontal plane wave)
Transmit and receive apodization	Rectangular
F-number	1.5

Table 3.2: Estimation parameters for the validation of the estimator

Parameter	**Value**
TO wavelength	1.5 mm
FWHM of TO	2.0 mm
Lag	1 frame (0.5 ms)
Ensemble length	64 frames (32 ms)
Spatial window	None

parameters are detailed in Tab. 3.2. A 5-cycle sinusoidal pulse was used without any apodization on the pulse and aperture to get good condition for validation. Before flow estimation clutter signals were removed using an 11^{th} order Butterworth filter with a cutoff of 0.5 cm/s. TO was introduced with a wavelength of 1.5 mm and an FWHM of 2.0 mm. For estimations, the lag was fixed to 1 frames to truly estimate displacements without using a lower virtual PRF. Estimations were done with an ensemble length of 64 frames to reduce noise, but without any spatial window to get rid of spatial smoothing effects.

3.3.1.2 Results

First, a qualitative inspection of the results was performed. At this end, vectors were displayed onto the B-mode images for both flow settings (Fig. 3.9). In both cases (Figs. 3.9a and 3.9b), profiles are mainly parabolic, as expected since it is a continuous flow, except close to the wall in the low flow setting (Fig. 3.9b) which

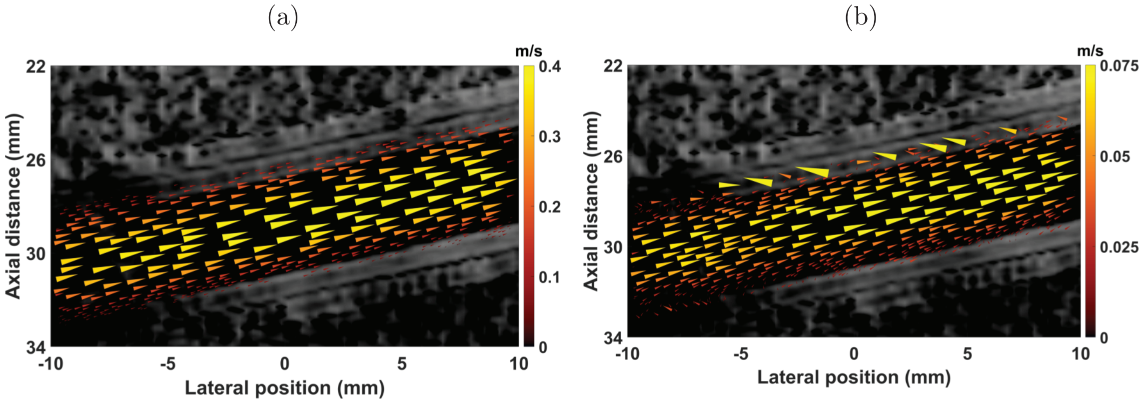

Figure 3.9: Estimated vector flow in a flow phantom: (a) with a high flow setting, and (b) with a low flow setting. The dynamic range is 40 dB.

are poorly estimated and appear as outliers.

To get more quantitative information, estimated velocity components, magnitude, and angle were extracted for the low (Figs. 3.10 and 3.11) and high (Figs. 3.12 and 3.13) flow settings. Theoretical laws of the flow profile were used as references knowing the true maximum velocities with the angles and assuming parabolic profiles; the angle was manually estimated based on the B-mode image. For a better comparison of the different estimates, velocity errors were normalized by the maximum flow velocity to get a value in percent. The angle error is in degree. All parameters were estimated over the full region of interest and across frames. First, concerning the estimates with the high flow setting (Figs. 3.10 and 3.11). Velocity profile estimates are parabolic with a low standard deviation (Figs. 3.10a, 3.10b and 3.11a) with an error of less than 10% in all the vessel. The angle is accurate (Fig. 3.11c) with a mean error of approximately 10% in the overall vessel (Fig. 3.11d). With the low flow settings the flow profile is still parabolic (Fig. 3.13a), but errors for both velocity components (Figs. 3.12a and 3.12b) get very high close to the wall; away from the wall the error in less than 10% (Fig. 3.12a) for the axial component and around 15% for the lateral component (Fig. 3.12b). The difficulty in extracting the velocity close to the wall creates a high error in the angle estimates (Figs. 3.13a and 3.13b) at that position. However, the overall angle error in the center of the lumen is good with a mean error less than 10%.

Overall, the method yields accurate flow profiles, with very low biases, low standard deviations, and low errors when the flow velocity is sufficient (more than 5 cm/s in the flow phantom). This effect can be explained by the small phase shift from one frame to another when the flow is low; this will result in high noise compared to the actual phase shift. Also, due to the clutter filter, which has a cutoff value

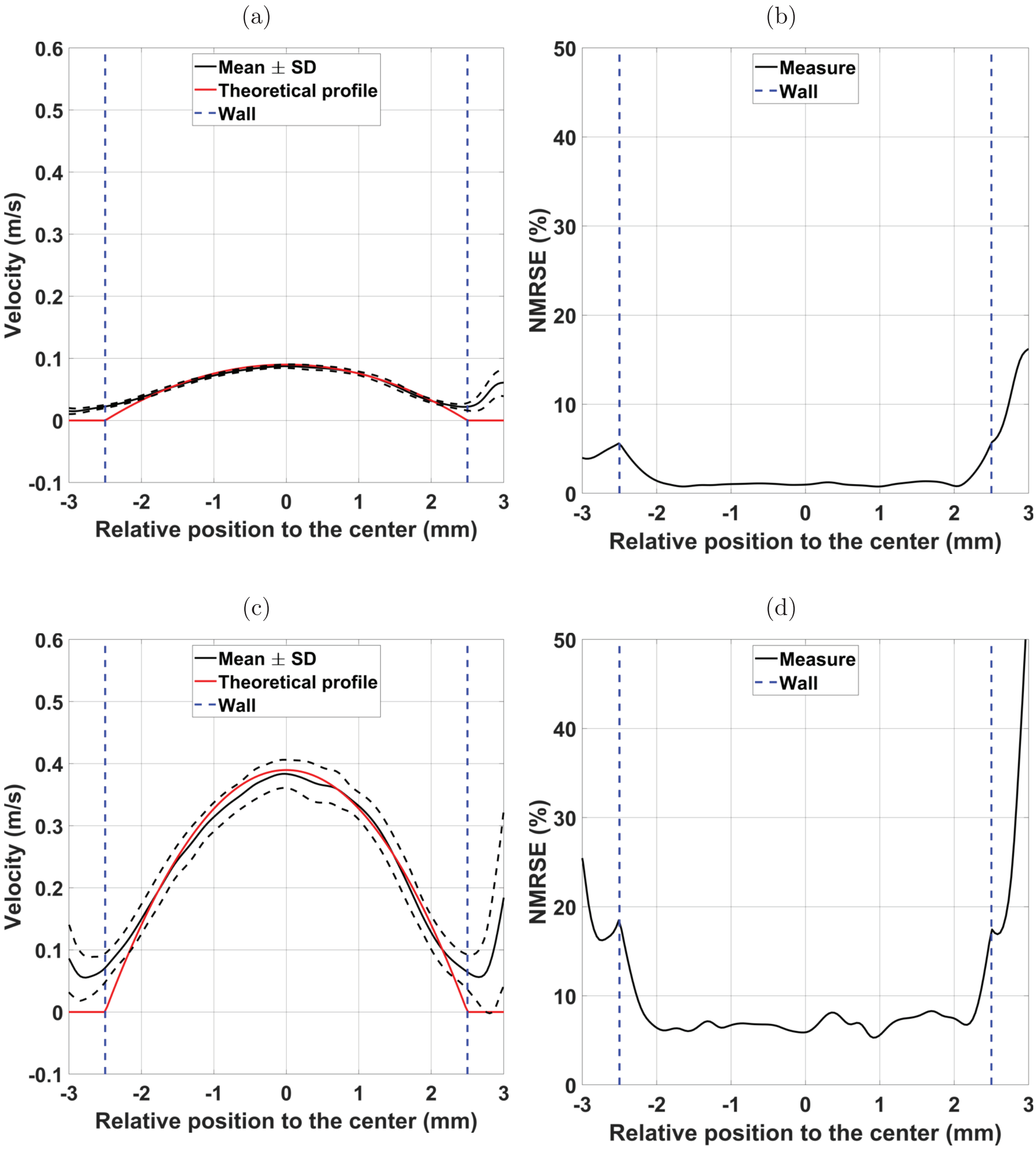

Figure 3.10: Estimated velocity components in a flow phantom with high flow velocity: (a) axial velocity component estimate, (b) error in percent (NMRSE) of the axial velocity component estimate, (c) lateral velocity component estimate, and (d) error in percent (NMRSE) of the lateral velocity component estimate. Velocities are in m/s and are shown with the mean and standard deviations over 1 000 estimations. Wall limits are represented by the dashed blue line while the red line represents the theoretical flow profile.

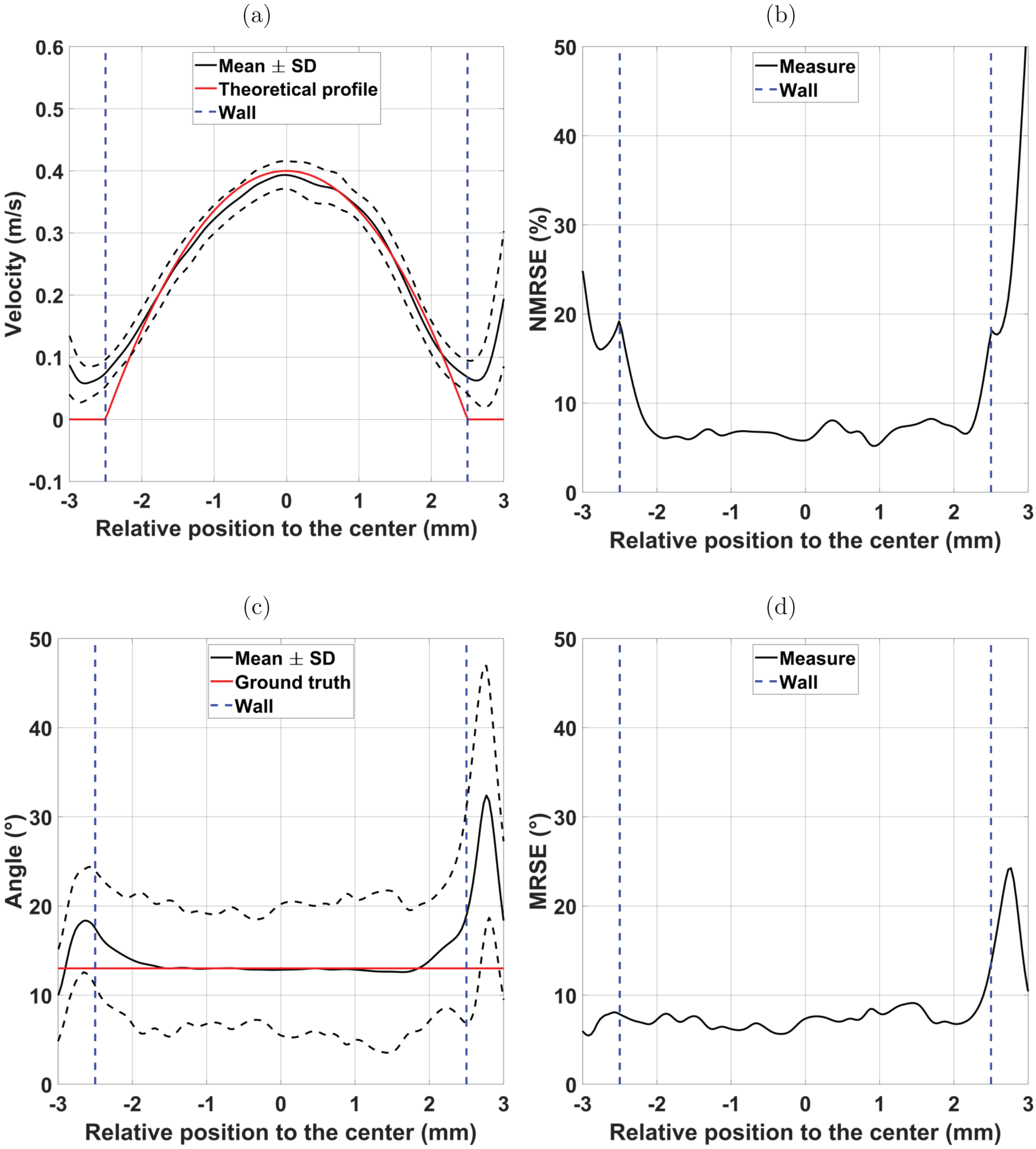

Figure 3.11: Estimated velocity magnitude and angle in a flow phantom with high flow velocity: (a) magnitude velocity estimate, (b) error in percent (NMRSE) of the magnitude velocity estimate, (c) angle estimate, and (d) error in degree (MRSE) of the angle estimate. Magnitude is in m/s while the angle is in degree, both are showed with the mean and standard deviations over 1 000 estimations. Wall limits are represented by the dashed blue line while the red line represents the theoretical flow profile for the magnitude velocity and the ground truth for the angle.

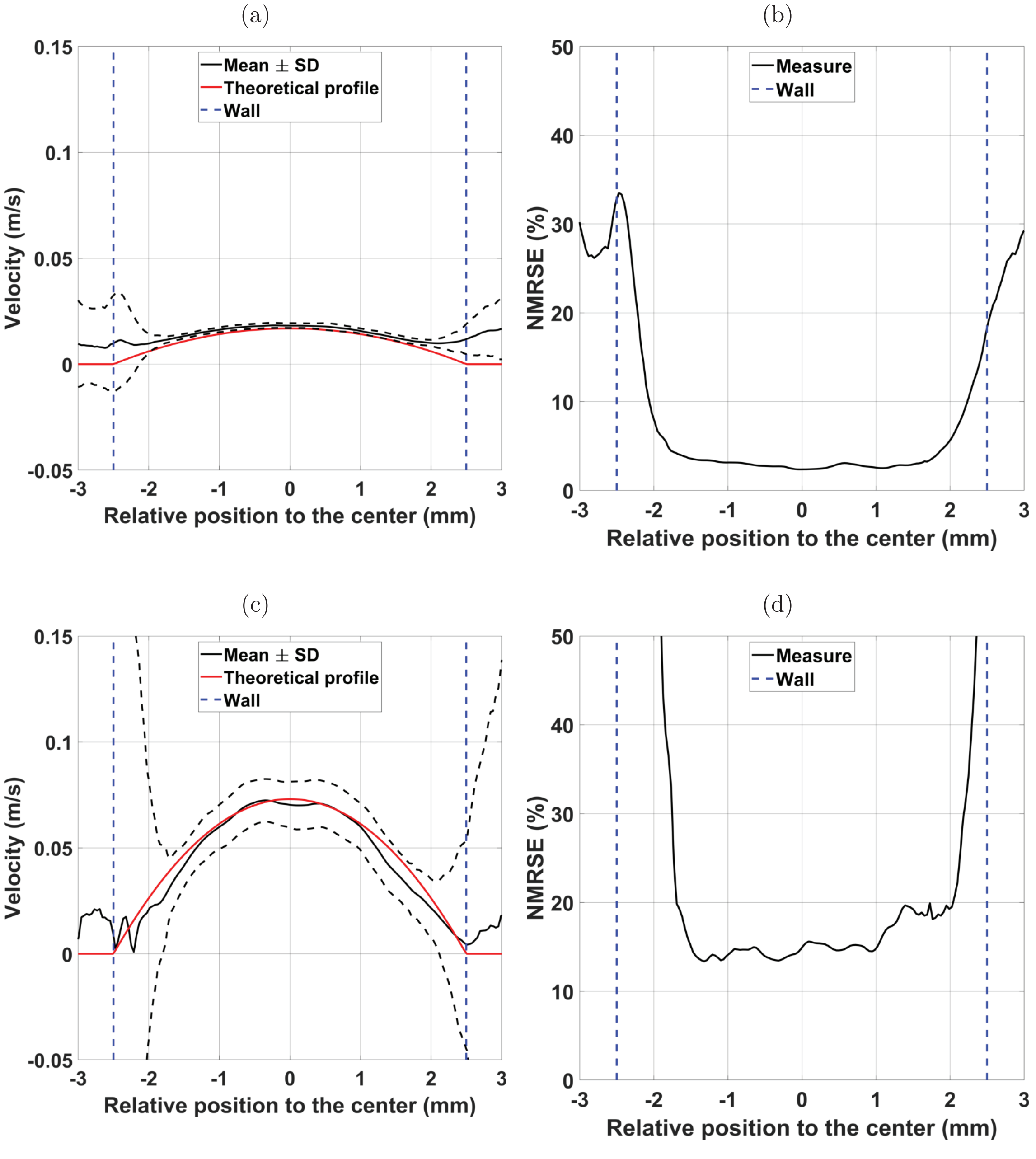

Figure 3.12: Estimated velocity components in a flow phantom with a low flow velocity: (a) axial velocity component estimate, (b) error in percent (NMRSE) of the axial velocity component estimate, (c) lateral velocity component estimate, and (d) error in percent (NMRSE) of the lateral velocity component estimate. Velocities are in m/s and are shown with the mean and standard deviations over 1 000 estimations. Wall limits are represented by the dashed blue line while the red line represents the theoretical flow profile.

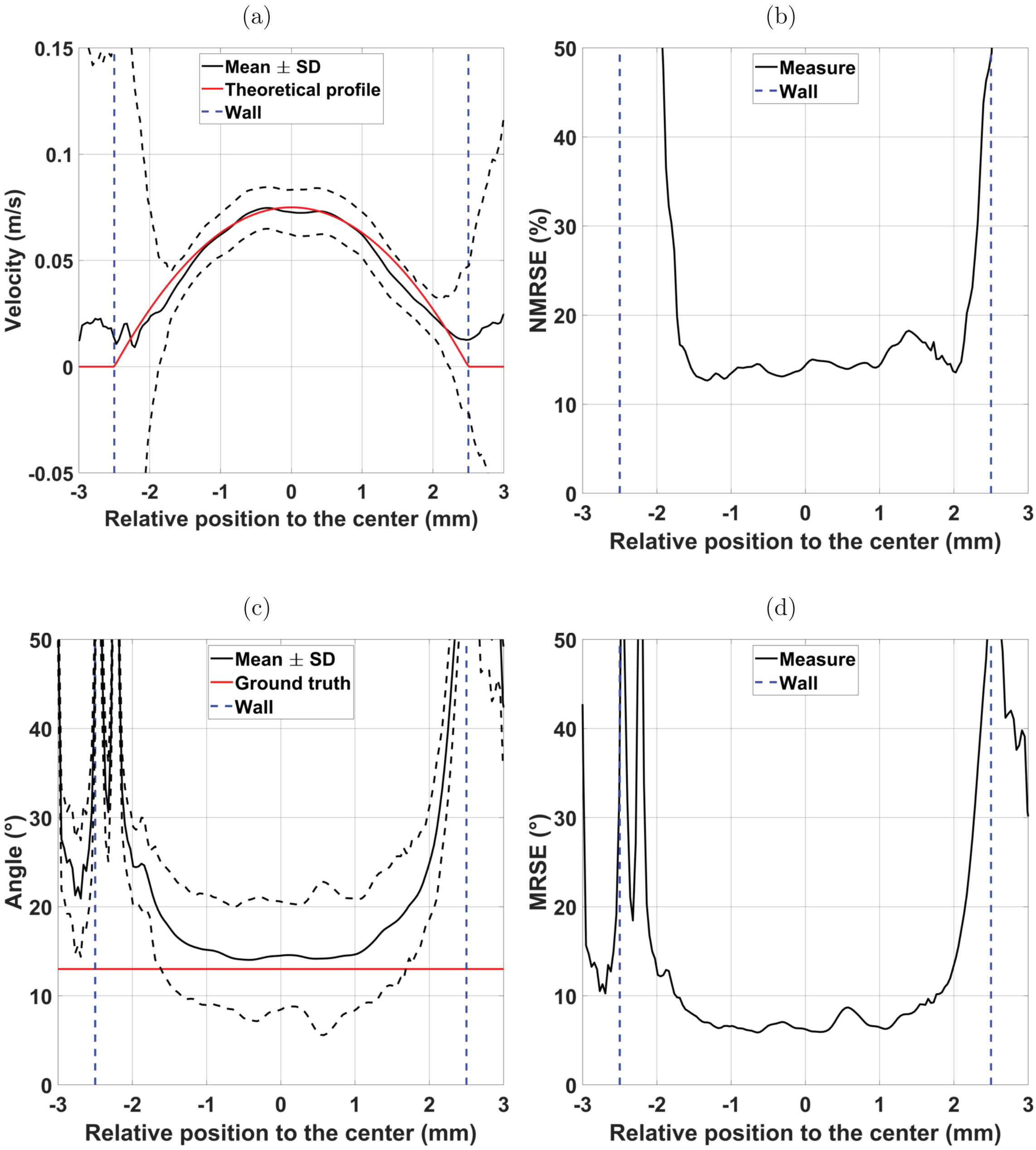

Figure 3.13: Estimated velocity magnitude and angle in a flow phantom with low flow velocity: (a) magnitude velocity estimate, (b) error in percent (NMRSE) of the magnitude velocity estimate, (c) angle estimate, and (d) error in degree (MRSE) of the angle estimate. Magnitude is in m/s while the angle is in degree, both are showed with the mean and standard deviations over 1 000 estimations. Wall limits are represented by the dashed blue line while the red line represents the theoretical flow profile for the magnitude velocity and the ground truth for the angle.

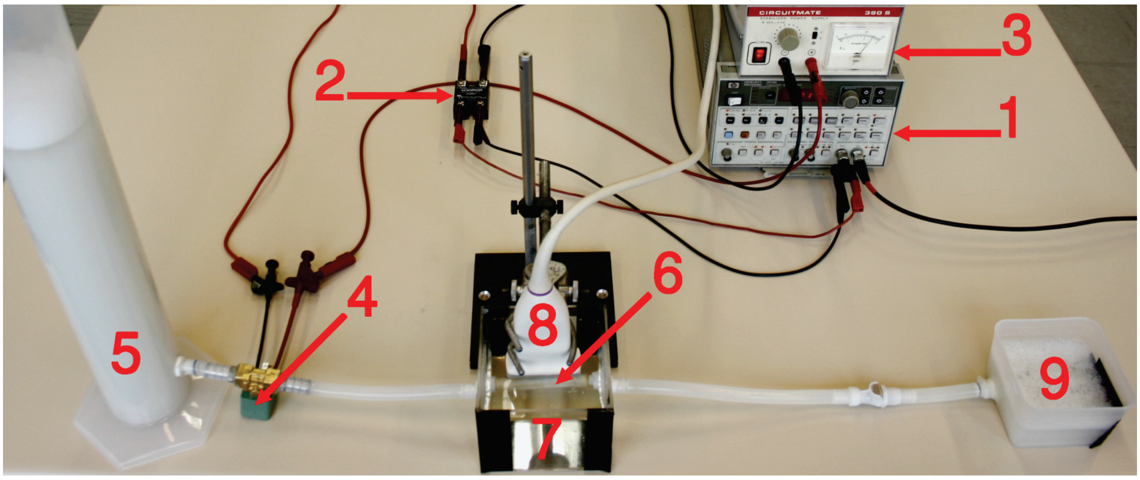

Figure 3.14: In-house realistic carotid phantom system: (1) function generator, (2) electronic switch, (3) 24 V power supply, (4) solenoid valve, (5) Doppler fluid column, (6) PVA phantom, (7) water tank, (8) US probe, and (9) outlet tank.

in the same velocity range as the flow close to the wall, the flow signal is strongly attenuated at the wall. Those issues are two challenges that are still studied in research. In practice, if we have an idea of the average velocity, it is possible to use a higher lag to get a larger phase jump to get rid of the first issue. Concerning clutter filtering, it is more challenging to get rid of its effect, and it is needed to work more on the clutter filter approach itself; this aspect is addressed in the next chapter since it is crucial for *in vivo* acquisitions. The implementation and the method itself is validated for further studies.

3.3.2 Realistic carotid phantom

3.3.2.1 Set-up design

Commercial flow phantoms are commonly used for validation of velocity estimation techniques since they are precisely calibrated by the manufacturer. Previously, the flow has been validated on such a system. However, with this system, walls are rigid, and it does not provide any kind of tissue motion validation. To validate the method on both aspects (flow and tissue), we propose an in-house system creating both wall and flow motions.

An in-house realistic carotid phantom has been designed, the system is depicted in Fig. 3.14 and Fig. 3.15. A function generator is in charge of controlling an electronic switch providing power to a solenoid valve with a specific duty cycle and giving a trigger to the ultrasound scanner. The solenoid valve controls the flow from a Doppler fluid column. The fluid passes through a PVA phantom immersed in

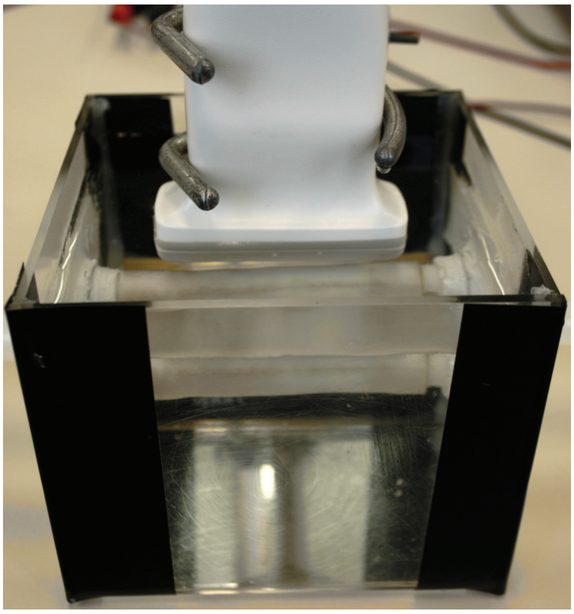

Figure 3.15: Close-up view of a PVA carotid. The probe is parallel to the vessel wall and in a longitudinal view.

a water tank for ultrasound imaging; the probe is above the phantom (Fig. 3.15). The outlet of the PVA phantom goes into a tank. The flow system is not closed; the outlet tank needs to be regularly emptied into the column to keep a constant flow. However, for a few cycles, the pressure at the bottom of the column can be considered constant.

The blood mimicking fluid was made with 5 μm Orgasol® (Arkema, Colombes, France), glycerol, surfactant, and distilled water (2%, 10%, 1% and 87% in weight, respectively) [138]. Orgasol® provides scatterers, glycerol sets viscosity, and surfactant ensures that the scattering particles are dispersed in the fluid. The resulting blood-mimicking fluid is in accordance with the standard physical and acoustic properties of blood [138]. Two columns were used with heights of 25 cm and 50 cm, providing two different static pressures. For the experiments, several PVA phantoms were molded of a length of 8 cm with a diameter of 8 mm and a thickness of 2 mm. The phantom preparation is composed of PVA, silica and distilled water (10%, 1% and 89% in weight, respectively) [139]. PVA acquires its properties by freeze-thaw cycles process; the higher the number of cycles, the higher the Young's modulus. PVA ensures elasticity while silica provides scatterers in the vessel wall. The resulting phantoms are very close to biological tissues in terms of acoustic and mechanical characteristic [139]. Finally, phantoms with four different number of freeze-thaw cycles (from 2 to 5 cycles) were investigated.

Acquisitions were performed using a Verasonics Vantage™ 256 system (Verasonics, Redmond, Washington, United States) as described in Tab. 3.3. Acquisitions were

Table 3.3: Acquisition parameters for the realistic carotid phantom

Parameter	**Value**
Probe	L 7-4, ATL Phillips
Number of elements	128
Pitch	298 μm
Central frequency	5.208 MHz
Sampling frequency	20.832 MHz
Excitation pulse	3-cycle sinusoidal
Pulse apodization	None (rectangular)
Speed of sound	1 540 m/s
Pulse repetition frequency	7 500 Hz
Compounding	No (single plane wave)
Steering angle	0° (horizontal plane wave)
Transmit apodization	Hann
Received apodization	Rectangular
F-number	Full aperture

performed at a high frame rate with a Hann apodization in transmit to reduce side lobes in the transmit field. Because SNR and experimental conditions were good, a full aperture was used for beamforming. For motion estimation, the same parameters as described in Tab. 3.2 were used except that no ensemble length was used, and the spatial window was here 2 mm high by 3 mm wide. Clutter signals were removed using a 1^{st} polynomial regression filer. For each freeze-thaw cycle, 3 phantoms were made, 2 different column heights (25 cm and 50 cm) were used, and 2 acquisitions were performed for each set-up. This results in a total of 48 acquisitions. For each acquisition, the valve was opened during 300 ms and the ultrasound research scanner was triggered by the function generator 100 ms before the opening. To analyze and characterize the phantoms, the flow velocity was extracted in the lumen of the phantom over time, and PWV was estimated for each phantom based on wall velocities, using the acceleration map as described previously.

3.3.2.2 Results

First, a qualitative inspection of the flow was made. For this purpose, vector flow and wall velocities were superimposed on the B-mode images (Fig. 3.16). At the very beginning of the cycle, after the opening of the valve (Fig. 3.16b), the wall starts moving and this moment corresponds to the moment were the PWV crosses the phantom in the field of view; this wave also ripples along the vessel wall. At this time, the flow in the phantom is almost zero (Figs. 3.16a and 3.16b). A few milliseconds (Fig. 3.16c) later the wall velocity is maximum and the flow starts

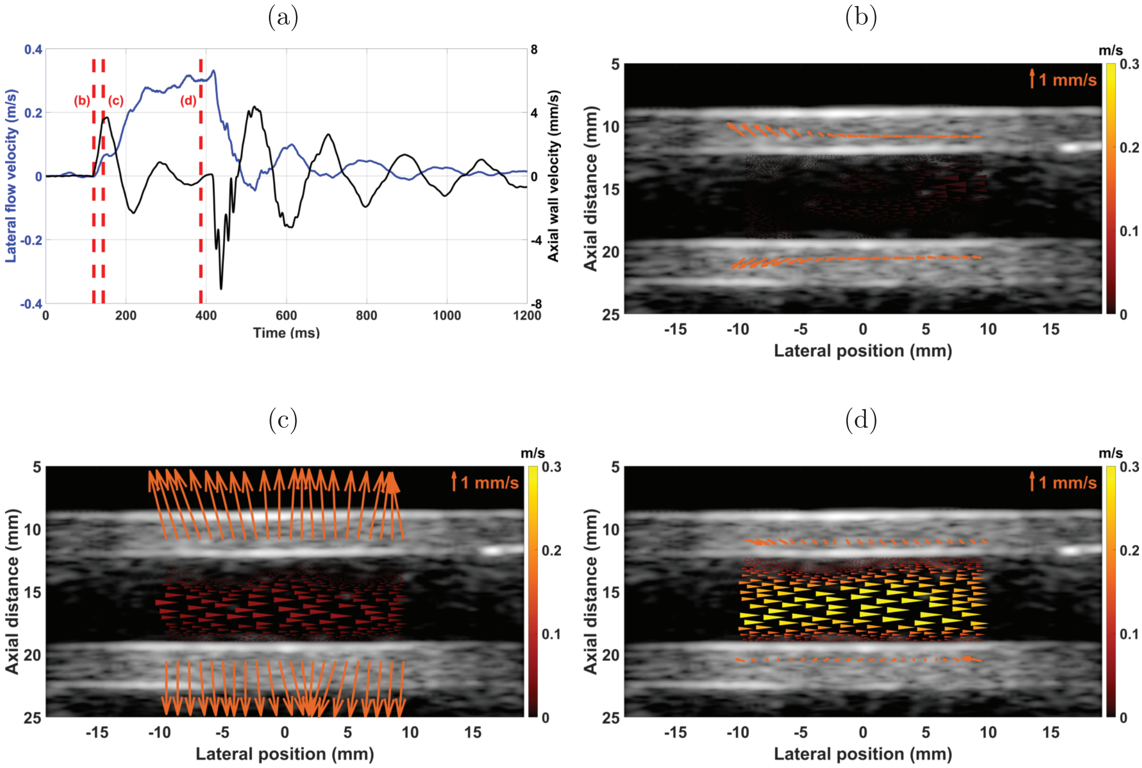
(a) (b) (c) (d)

Figure 3.16: Vector flow and wall velocities in a PVA carotid phantom: (a) temporal evolution of the lateral flow velocity and axial wall velocity for reference, (b) at the very beginning of the cycle when the wall starts moving, (c) when the wall velocity is maximum, and (d) when the flow is maximum. The dynamic range is 40 dB.

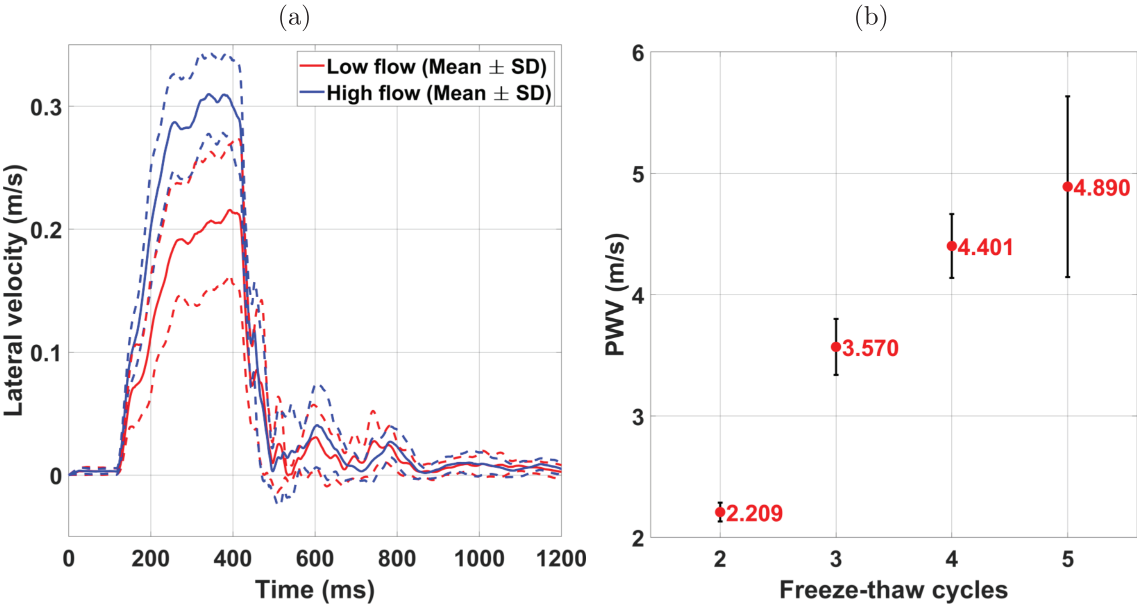

Figure 3.17: Estimated flow and pulse wave velocities in a series of PVA phantoms: (a) temporal evolution of the flow is the center of the phantoms for the low and high flow set-up with standard deviation, and (b) PWV depending upon the freeze-thaw cycles. All measurements are showed with standard deviations; a total of 48 acquisitions were performed, PWV was evaluated on both walls.

flowing into the PVA phantom. Right before the closure of the valve (Fig. 3.16d) the flow reaches its peak velocity, but the wall is not expending anymore, the vessel has reached its maximum diameter. After the closure of the valve (Fig. 3.16a), the flow and wall are subject to oscillatory phenomena due to the brutal stopping of the flow.

To get more quantitative values on the estimates, flow velocity was evaluated in the center of the phantom with PWV as a function of the freeze-thaw cycles (Fig. 3.17). Concerning the maximum flow velocity in the center of the lumen (Fig. 3.17a), the mean value during the opening of the valve is 0.201 m/s and 0.299 m/s for the low and high flow settings, respectively. We do not have access to the ground truth concerning the flow velocity. However using Bernoulli's theorem, the pressure drops from one point A to another point B is proportional to the square of the velocity and also proportional to the height of the fluid column. So, the velocity directly proportional to the square root of the height. To get rid of unknown variables, we can consider the velocity ratio between the two flow settings. The mean velocity ratio is 1.486 which should be equal to the square root of the height difference which is $\sqrt{2} \approx 1.414$, those two values should be equal if we neglect pressure losses. The error in this ratio is around 5%, which is decent regarding the assumptions made. The standard deviation is high compared to the results obtained with the previous phantom. The standard deviations are 12.2% and 26.4% for the low and high flow settings, respectively. This effect can be explained by different pressure losses from one estimate to another and by slight changes in the height of the fluid columns and output tank. However, flow patterns are accurate, and the flow measurements are in accordance with our expectations.

For PWV estimates, the elasticity increases with the number of freeze-thaw cycles (Fig. 3.17b). This trend is expected since the Young's modulus is related to this number of cycles. The pulse wave velocity increases with the number of freeze-thaw cycles as predicted from 2.209 m/s ±3.53% to 4.890 m/s ± 15.23%. The shape of the curve seems to flatten, which is also expected since the theoretical curve converges after 5 freeze-thaw cycles [139]. All linear regressions for PWV estimations were accurate with a correlation coefficient (between the maximum points and the linear regression) higher than 0.95. The standard deviations remain small compared to the pulse wave velocities even if they increase with the number of freeze-thaw cycles. Indeed, when the PWV increases, the number of frames where the pulse wave crosses the phantom decrease, which reduces the robustness of the estimates and increases the standard deviation. Moreover, the fabrication of PVA phantoms is long (one day for each freeze-thaw cycle). Consequently, differences during the thawing process might have occurred in particular due to some temperature variations; those differences accumulate with the number of freeze-thaw cycles. Overall, the method can extract pulse wave velocity related to the elasticity of the medium and flow velocity in accordance with our expectations.

3.4 From *in vitro* to *in vivo* experiments

In this chapter, the transverse oscillation technique has been described, and an approach permitting to introduce TO in the f-k spectrum at an inexpensive cost has been described. Validation on *in vitro* phantoms can be tricky. However, using two different phantoms, one for flow and an in-house system for PWV imaging, the method has been validated for both tissue and flow motion imaging.

Since the method is now validated, the next stage is to validate the approach *in vivo* and also to determine the feasibility in a clinical environment. Unfortunately, with *in vivo* and clinical acquisitions, clutter can be more challenging to get rid of. Indeed, with patients, tissue can be subject to high velocity that overlaps with flow velocity estimates. Moreover, SNR is not as good as with *in vitro* data. Since the method can yield tissue velocity estimates, it seems appropriate to use that information to remove clutter and improve the flow estimate.

For this purpose, in the next chapter, clutter filtering is described, and methods to improve flow estimates *in vivo* are presented. Those methods use the tissue estimates to get rid of undesired clutter coupled with a temporal adaptive approach permitting to improve flow estimates.

Chapter 4

Adaptive Clutter Filtering Based on Tissue Velocity Estimates: *In Vivo* Volunteers

The fourth chapter is the description of the methodology for adaptive clutter filtering techniques that are based on the tissue velocity estimates. First, clutter filtering is introduced with a description of clutter and flow signals. Conventional convolution-based filters (finite and infinite impulse response) are depicted with regression-based (polynomial), and eigen-based filters (principal component analysis and singular value decomposition); automatic data-driven clutter filters are also described. After listing the standard categories of filters, the motivations for a clutter filtering technique based on tissue estimates are reported. Then, the conventional approaches for comparison are described with details on the temporal adaptive and spatial and temporal adaptive clutter filtering methods. Finally, *in vivo* experiments are reported on volunteers with the description of the material and methods, presentation of the results, and a comparison with a data-driven approach based on singular value decomposition. The fourth chapter concludes with the potential application of adaptive clutter filtering in clinics.

There are two proceedings at *International Ultrasonics Symposium* as evidence of the scientific contribution: “Spatial and temporal adaptive FIR clutter filtering” (2018), and “Comparison of adaptive clutter filters for vector velocity estimation: realistic simulations and in vivo examples” (2019). Parts of the contribution presented in this chapter were conducted during a six weeks doctoral stay in the Department of Circulation and Medical Imaging in the Norwegian University of Science and Technology, Trondheim, Norway.

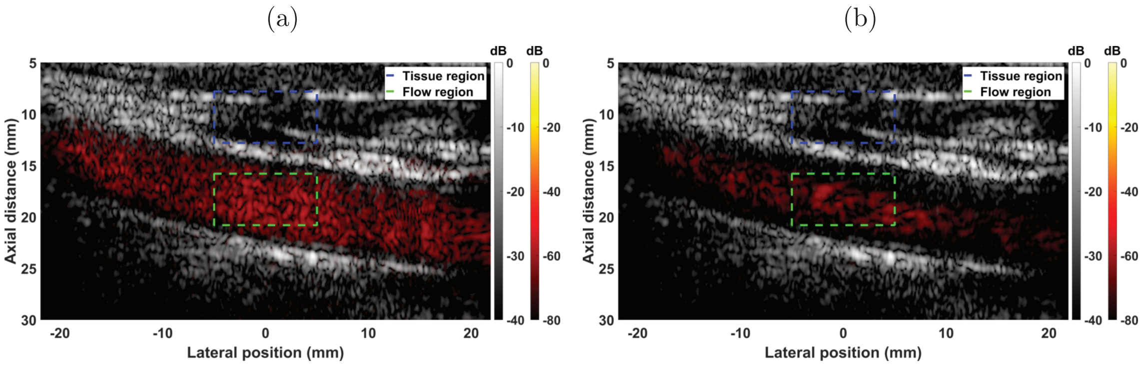

Figure 4.1: Measurement of tissue-to-flow ratio: (a) flow power superimposed onto the standard B-mode image at systole, and (b) flow power superimposed onto the standard B-mode image at late diastole. To mitigate stationary clutter signals, the signals were low-pass filtered by a 1^{th} order Butterworth filter with a cutoff velocity of 5 cm/s. Acquisitions were performed on a healthy volunteer using a plane wave imaging mode with a Verasonics Vantage$^{\text{TM}}$ 256 system (Verasonics, Redmond, Washington, United States). The dashed rectangles indicated the areas to compute the tissue-to-flow ratio; the tissue is used as a reference for power estimation.

4.1 Introduction to clutter filtering

The first section of the fourth chapter presents an introduction to clutter filtering. This section is broken down into five subsections: clutter and flow signal, convolution filters, regression filters, eigen-based filters, and data-driven clutter filters. In the following, clutter filtering is introduced with the different categories of filters for clutter rejection.

4.1.1 Clutter and flow signal

Clutter filtering is an essential step before flow estimation. Indeed, flow backscatters less energy than surrounding tissue. Due to the PSF of the system, the tissue signal extends into the lumen and obscures flow signals. Moreover, some strong tissue artifacts can also be found in the lumen, such as reverberation echoes of the wall in the lumen. Then, without clutter filtering, mean frequency estimators are biased for flow estimation due to this gap in terms of power. An example is provided in Fig. 4.1 where the power of the flow signal after clutter filtering is superimposed onto the B-mode images at systole (Fig. 4.1a) and late diastole (Fig. 4.1b). In Fig. 4.1 the tissue-to-flow ratio is 38.66 dB and 47.41 dB in systole and diastole, respectively. Moreover, visual inspection of the flow power compared to tissue (Fig. 4.1) permits to realize that flow and tissue are in a completely different order of magnitude. Consequently, flow signals must be isolated from clutter before flow estimation.

Tissue, like flow, is subject to motion according to the different phases of the cardiac cycle. This effect needs to be taken into account for clutter filtering. For instance, in Fig. 4.2 Doppler spectra of both tissue and flow are depicted without clutter filtering. B-mode image (Fig. 4.2a) shows where the Doppler spectra of tissue (Figs. 4.2c to 4.2e) and flow (Figs. 4.2f to 4.2h) were extracted. Axial tissue velocity (Fig. 4.2b) was also estimated using the complex autocorrelation of received signals. Axial velocity of tissue (Fig. 4.2b) and Doppler spectra of tissue (Figs. 4.2c to 4.2e) show that tissue moves throughout the overall cardiac cycle with velocity peaks during systole (red arrows in Fig. 4.2c and Fig. 4.2d) and diastole (green arrows in Fig. 4.2c and Fig. 4.2e) due to mechanical wave propagating along wall, heart beating, and flow pressure. Wall velocity can be seen in the center of the lumen without clutter filtering (Figs. 4.2f to 4.2h) worsening spectrum dynamic and still with a gap of approximately 40 dB. Tissue velocity can be more or less high depending on the current phase of the cardiac cycle, but the tissue still dominates the spectrum dynamic.

As an introduction to clutter filtering, to get rid of clutter signals the most straightforward and natural technique is to use a fixed target canceler by substrating consecutive ultrasound pulses to remove stationary signals [68], [140]; it comes from sonar where the ground is perfectly stationary. Even if this approach is natural, it assumes that the clutter is stationary throughout the acquisition, which is false regarding tissue and relative displacement due to the handling of the ultrasound probe. However, such a technique can be modified using a larger observation window for canceling [140].

4.1.2 Convolution filters

4.1.2.1 Finite impulse response

Finite impulse response (FIR) filters are, as the name implies, real filters with a finite duration. It means that the impulse response of a N^{th} order FIR filter lasts exactly $N+1$ samples. The fixed target canceler is one of the simplest 1^{st} order (2 samples) FIR filter. Such filter can be expressed as a finite convolution sum considering a fixed spatial point during acquisitions (Eq. (4.1)):

$$y\left(t\right)=\sum_{n=0}^{N}h\left(n\right)x\left(t-n\right) \tag{4.1}$$

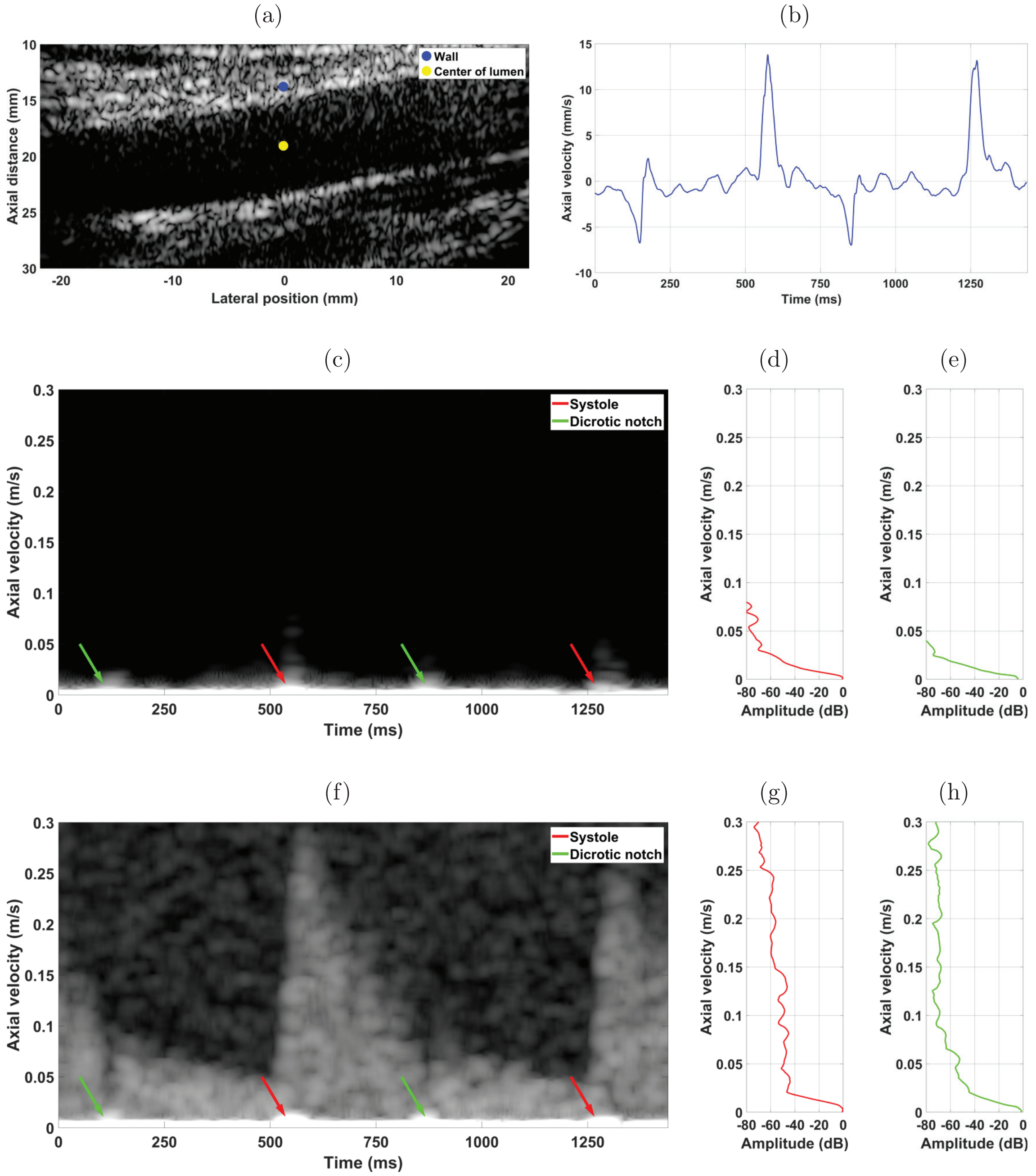

Figure 4.2: Doppler spectra of tissue and flow without clutter filtering: (a) B-mode image with the positions for extracting Doppler spectra in tissue and flow, (b) axial wall velocity during time at the point in (a), (c) Doppler spectrum in the wall at the point in (a), (d) Doppler spectrum of the wall at systole, (e) Doppler spectrum of the wall at dicrotic notch, (f) Doppler spectrum in the flow at the point in (a), (g) Doppler spectrum of the flow at systole, and (h) Doppler spectrum of the flow at dicrotic notch. Spectra are frequency-based while the axial wall velocity estimate is phase-based. Acquisitions were performed on a healthy volunteer using a plane wave imaging mode with a Verasonics Vantage$^{\mathrm{TM}}$ 256 system (Verasonics, Redmond, Washington, United States). The dynamic ranges are 40 dB for the B-mode image and 80 dB for the spectra.

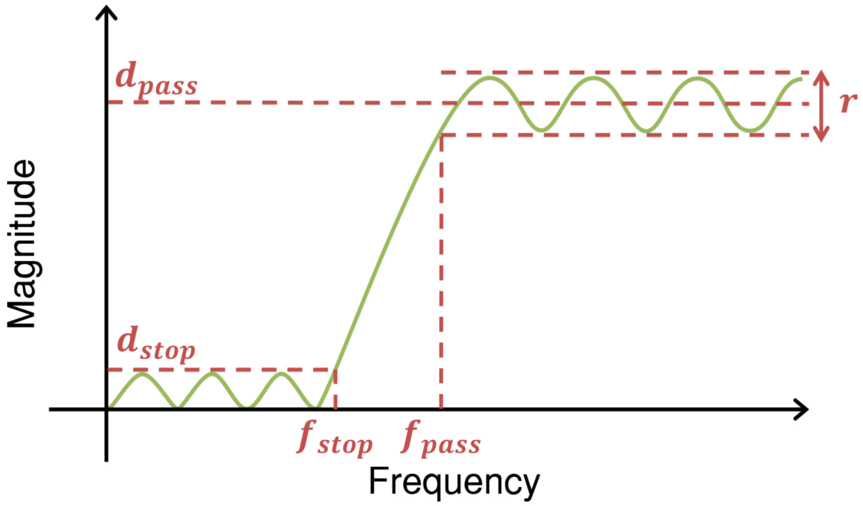

Figure 4.3: Design parameters for a frequency-based filter: ripple (r) is around the pass magnitude (d_{pass}), attenuation of the stopband (d_{stop}) is for a given stop frequency (f_{stop}) which results to a frequency range corresponding to a transition band from attenuated stop frequency (f_{stop}) to pass frequency (f_{pass}).

where y is the filtered signal, h are the coefficients of the N^{th} order filter, and x the signal before filtering. Due to the length of the filter, the valid output is reduced by the order of the filter.

FIR filters have been described for Doppler imaging by Torp [135] and Bjaerum *et al.* [136]. To design a filter, several parameters need to be taken into account (Fig. 4.3). Because having a filter of an infinite length is not possible, the filter is an approximation of a perfect step filter, so attenuation, ripple, and transition band are additional parameters compared to a perfect step filter setting only by a single stop/pass frequency. FIR filters can be designed with a linear phase, so no distortion depending on the frequency will appear, and all frequency components of the input signal will be shifted in time of the same delay. Moreover, they are, by nature, always stable. Several numerical design methods exist and permit to create such filters[†] using different approaches such as a weighted least-squares method, a window model (for instance a Kaiser windowing), or an iterative approach (for instance equiripple). Whatever the design method, all parameters of the filter are dependent and fixing all the parameters is impossible. For a given attenuation, if we want the transition width and ripples to be very small, this will result in a very high order. Another example, for the same attenuation, fixing a very small order will result in a large transition band and/or ripples.

[†] Filter design is a complex field of engineering on its own. To design the filters, the DSP System Toolbox™ of MATLAB (The MathWorks, Natick, Massachusetts, United States) was used with optimized built-in functions.

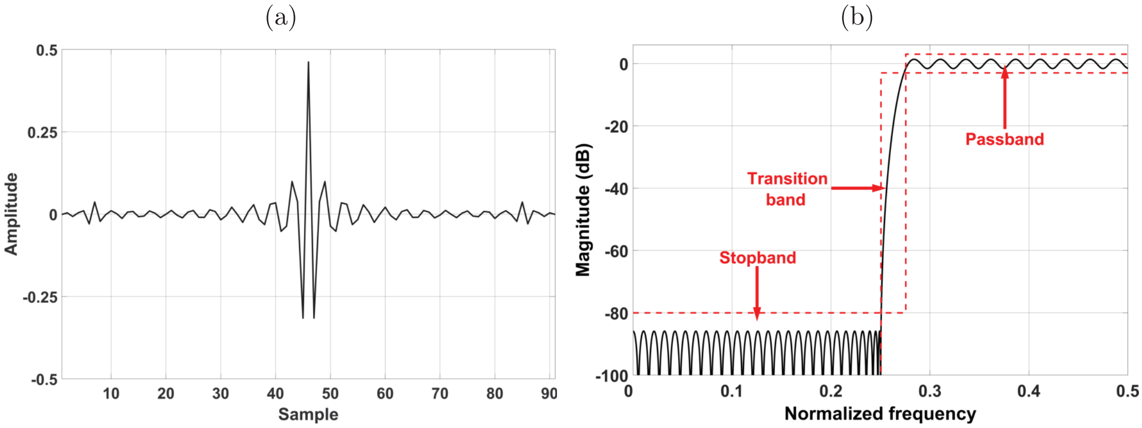

Figure 4.4: Example of an FIR filter: (a) coefficients of the filter, and (b) frequency response of the filter. The frequency axis is normalized regarding the sampling frequency for comparison with other filters. The filter is an equiripple filter with an attenuation of 80 dB, stop frequency at 0.25 with a transition band of 0.025, and maximum ripple of 6 dB; the resulting order of the filter is 90.

An example of an FIR filter is provided in Fig. 4.4; the filter is designed as an equiripple filter which ensures less maximum error in the design than other FIR designs at the cost of a constant ripple in the passband. To achieve the desired impulse response (Fig. 4.4b) the filter is quite long (Fig. 4.4a). The advantages of FIR filters come to the cost of a relatively high order. This disadvantage can lead to voluntarily reduce the performance of the filter to have a smaller order to have valid output samples in case of a short observation window for the signal.

4.1.2.2 Infinite impulse response

Another variety of convolution-based filters are infinite impulse response (IIR) filters. As the name suggests, such filters do not have a finite impulse response, and if a Dirac impulsion is used as the input the output does not become exactly zero past a certain point but continues indefinitely. Such filters are expressed as a convolution product with a recursive approach (Eq. (4.2)):

$$y\left(t\right)=\sum_{n=0}^{N}h_b\left(n\right)x\left(t-n\right)-\sum_{n=1}^{N}h_a\left(n\right)y\left(t-n\right) \tag{4.2}$$

where h_a and h_b are the coefficients of the filter. The recursive approach is the cause of the infinite impulse response of the filter; any impulsion will give residues that will last forever in the output.

IIR filters have also been described for Doppler imaging by Torp [135] and Bjaerum *et al.* [136]. IIR filters have also the disadvantage not to have a linear phase (this

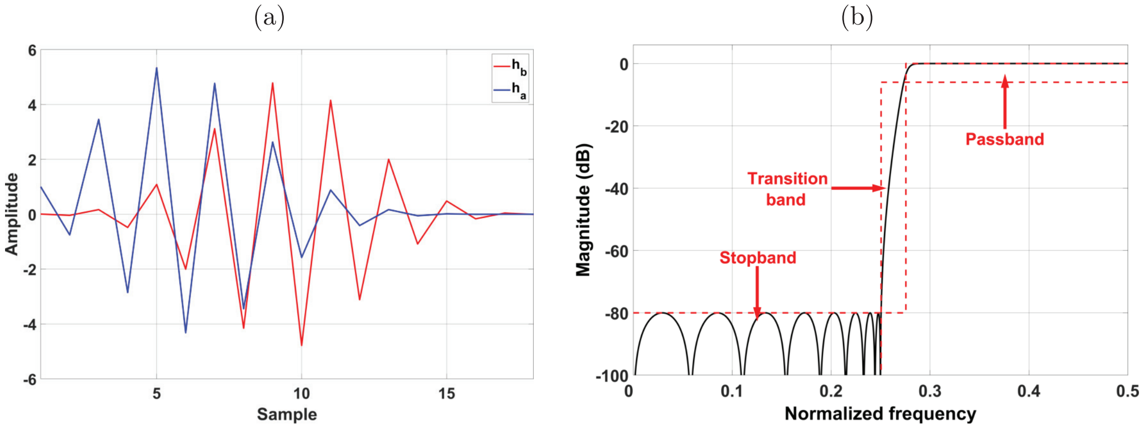

Figure 4.5: Example of an IIR filter: (a) coefficients of the filter, and (b) frequency response of the filter. The frequency axis is normalized regarding the sampling frequency for comparison with other filters. The filter is a Chebyshev type II filter with an attenuation of 80 dB, stop frequency at 0.25 with a transition band of 0.025, and maximum ripple of 6 dB; the resulting order of the filter is 17.

effect can be minimized during the design), which results in a distortion of the output which must be taken into account. Moreover, because of the recursive approach, they are sensitive to initialization and are not always stable, accumulation of errors can occur in the output samples. Several numerical design methods exist and permit to create such filters depending on several criteria such as the best Taylor Series approximation (Butterworth) or minimization of the absolute difference between the ideal and actual frequency response (Chebyshev). For comparison with an FIR filter, an example of an IIR filter is provided in Fig. 4.5 using a Chebyshev type II which gives ripples only in the stopband; the filter was designed with the same restrictions as the FIR filter (Fig. 4.4). To achieve the desired filtering (Fig. 4.5b), the filter order is lower (Fig. 4.4a) than the FIR filter (Fig. 4.4b). The advantages of IIR filters come to the cost of a non-linear phase and particular attention during designing.

4.1.3 Regression filters

The simplest form of regression is the linear regression as proposed by Hoeks *et al.* in 1991 [141]. It consists of considering several time points and remove a linear fitting from this dataset. Polynomial regression filters assume that clutter echoes are of high amplitude and vary slowly compared to blood signals; then clutter signals can be approximated by a polynomial based for instance, on a least-squares method. By adjusting the packet size (the number of points to consider) and the order of the regression, the cutoff frequency can be set.

Linear regression is a first-order polynomial regression. The technique can be used with any different order and has been described by Torp [135] and Bjaerum *et al.* [136]. To do this regression, basis functions are needed to determine the properties of the regression. The general filtering operation, for any linear filtering, can be expressed as (Eq. (4.3)):

$$y = Ax \tag{4.3}$$

where y is the N samples row output, x is the N samples row input, and A the filter matrix. For a polynomial regression, the filter matrix is expressed as (Eq. (4.4)):

$$a\left(n,m\right) = \delta\left(n,m\right) - \sum_{k=0}^{K} b_k^*\left(n\right) b_k\left(m\right) \tag{4.4}$$

where $a\left(n,m\right)$ is the value of the filter matrix at the position n,m, δ is the Dirac function, and b_k the k^{th} basis function; * is the conjugate notation. Such a regression have a frequency response that can be calculated as (Eq. (4.5)):

$$H_0\left(f\right) = 1 - \frac{1}{N}\sum_{k=0}^{K} B_k^*\left(f\right) B_k\left(f\right) \tag{4.5}$$

where H_0 is the response of the filter, K the order of the regression, N is the packet size, and B_k is the Fourier transform of the basis function k; * is the conjugate notation. While many functions can be used as a basis, sinusoidal and Legendre polynomial bases are often used. The Legendre polynomial basis is often preferred because of its high stopband rejection. Such polynomials can be expressed as (Eq. (4.6)):

$$P_n\left(x\right) = \frac{1}{2^n\ n!}\frac{d^n}{dx^n}\left(x^2-1\right)^n \tag{4.6}$$

where P_n is the nth polynomial. Polynomial regression is depicted in Fig. 4.6 where the very first polynomials are shown (Fig. 4.6a) with the frequency responses for the 5^{th} order polynomial regressions (Fig. 4.6b). For a fixed packet size, the higher the order of the regression, the higher the cutoff. Also, increasing the packet size for a fixed order of regression gives a lower cutoff. Then, the cutoff is inversely proportional to the packet size and proportional to the order of the regression. An example is provided in Fig. 4.7 where a polynomial regression is applied onto two signals with two different trends (1^{st} and 3^{rd} orders). In both cases (Figs. 4.7a and 4.7b) the regression was able to remove the overall trend, and the residue should correspond to high-frequency components mainly due to flow. However, the packet size and the order of the polynomial regression have a major influence on the fitting and residue. Consequently, to fix those parameters, we need assumptions on the input signal or a method to first estimate the order of the clutter before filtering.

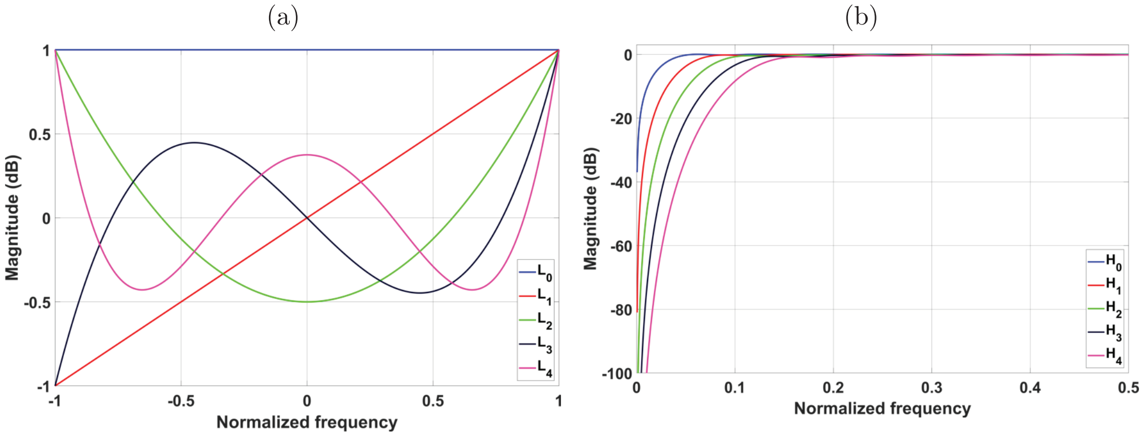

Figure 4.6: Example of Legendre polynomials and frequency responses for Legendre polynomial regression: (a) normalized first four Legendre polynomials, and (b) frequency responses for the Legendre polynomial regressions for the first four orders. Packet size is 16 frames, polynomials are normalized for display, and numbers in indices describe the order.

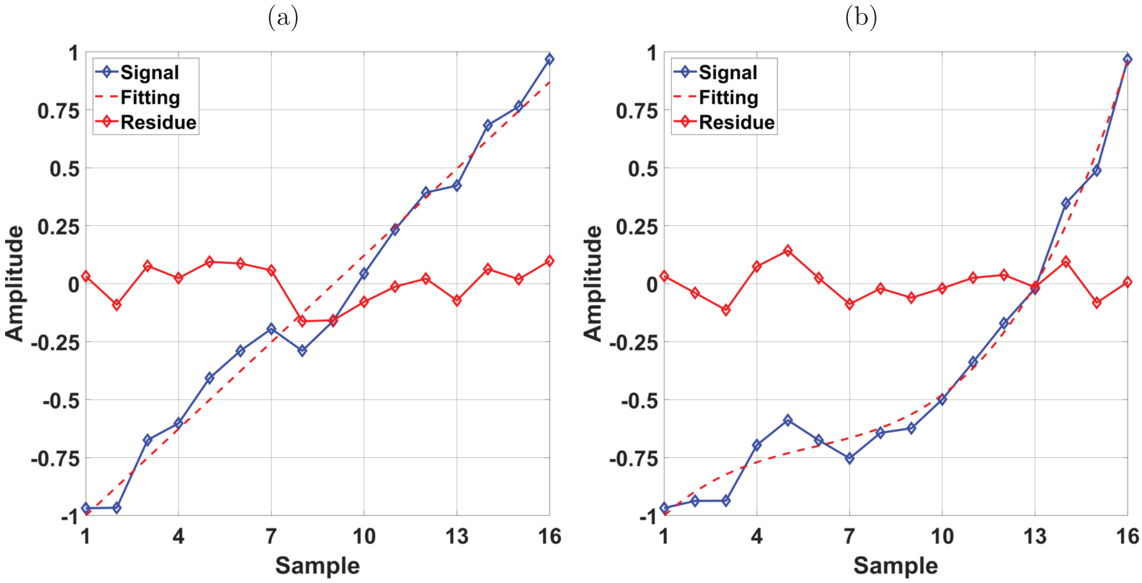

Figure 4.7: Example of polynomial regressions with two different orders: (a) polynomial regression for a 1^{st} order signal, and (b) polynomial regression for a 3^{rd} order signal. For each regression, the input signal has a trend in accordance with the order of the regression.

4.1.4 Eigen-based filters

Eigen-based filters started to be used and developed in the mid 90s for Doppler flow imaging [142], [143]. Those filters have been described for flow imaging in a review by Yu and Løvstakken [144] and can be used as other filters in real-time with automatic criterion [145].

Briefly, eigenvalues decomposition assumes that a slow-time vector (1D signal, one single reception from a element) can be decomposed as (Eq. (4.7)) [144]:

$$x\left(t\right)=\sum_{k=1}^{N}\gamma_k\left(t\right)e_k \tag{4.7}$$

where x is the slow-time vector of length N, γ_k is the kth weight, and e_k is the kth eigenvector. Due to the orthogonality the weights must satisfy (Eq. (4.8)):

$$E\left\{\left(\gamma_k\left(t\right)e_k\right)^{*T}\left(\gamma_l\left(t\right)e_l\right)\right\}=\begin{cases}\lambda_k\left(t\right), & \text{if } k=l\\ 0, & \text{otherwise}\end{cases} \tag{4.8}$$

where λ_k is kth eigenvalue; * is the conjugate notation and ^{T} is the transpose operation. Usually, components are ranked in a descending energy order. Consequently, it is possible to remove clutter from the slow-time vector by determining the last eigenvalue of the clutter and set the previous eigenvalues to zero.

Let us define the following correlation matrix through eigenvalue decomposition (EVD) (Eq. (4.9)) [144]:

$$R\equiv AA^{*T}=E\left\{xx^{*T}\right\}=\sum_{k=1}^{N}\lambda_k e_k e_k^{*T} \tag{4.9}$$

In that case, the matrix A (non-square) can be written using two different bases for decomposition as (Eq. (4.10))

$$A=\sum_{k=1}^{N}\sigma_k u_k v_k^{*T} \tag{4.10}$$

where σ_k is the kth singular value, u_k is the kth eigenvector of the column space, v_k is the kth eigenvector of the line space; u_k and v_k are named the left and right singular vector. This is the singular value decomposition (SVD). Introducing A^{*T}

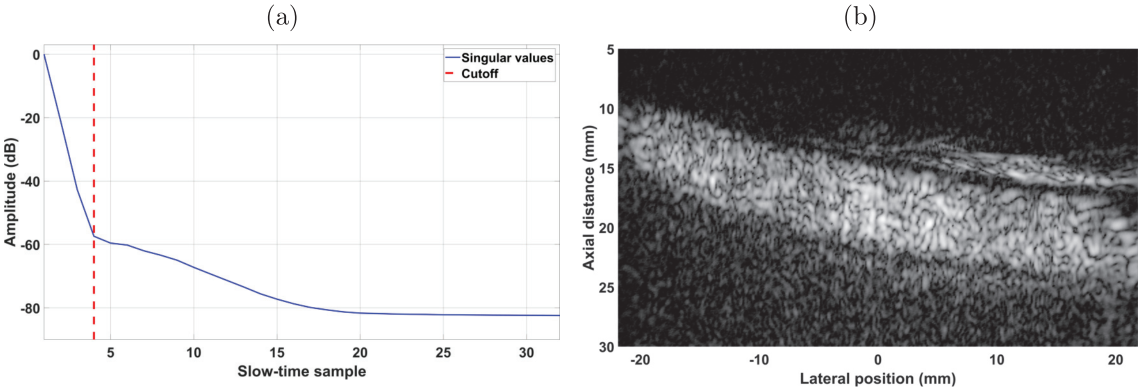

Figure 4.8: Example clutter filter using SVD: (a) singular values amplitude in dB before filtering with selected cutoff, and (b) B-mode image after clutter filtering at the given cutoff. The cutoff was manually selected to remove clutter in the acquisition based on the curve in (a). The frame is during systole with a dynamic range of 40 dB.

in Eq. (4.10) permit to compare the SVD with EVD (Eq. (4.11))

$$AA^{*T} = \sum_{k=1}^{N} \sigma_k^2 u_k u_k^{*T} \equiv R \tag{4.11}$$

It appears from Eq. (4.9) and Eq. (4.11) that the left singular vectors of A are eigenvectors of AA^{*T}, the right singular vectors of A are eigenvectors of $A^{*T}A$, and the singular values of A are the square roots of the eigenvalues of both AA^{*T} and $A^{*T}A$.

Usually, the SVD is written in a matrix form (Eq. (4.12)):

$$A = U\Sigma V \tag{4.12}$$

where A is the matrix before factorization, U and V are matrices with respectively the left and right singular vectors of A, and Σ is a diagonal matrix with the singular values of A. If A has a size of $n \times m$, U is $n \times n$, Σ is $m \times n$, and V is $m \times m$. The main interest of the SVD is that the input matrix can be non-square while the EVD is applied onto a square correlation matrix. For flow imaging, the input matrix for SVD is often a set of slow-time observations arranged in a 2D form like observations × slow-time. The very first singular values can be set to zero in Σ to remove clutter. An example is provided in Fig. 4.8 where clutter was removed based on an inspection of the singular values (Fig. 4.8a), after clutter filtering flow is dominant in the B-mode image (Fig. 4.8b).

4.1.5 Data-driven clutter filters

Both polynomial regression and eigen-based filters can be used as data-driven clutter filters. Such data-driven approaches are based on a criterion to set the optimal cutoff automatically.

Akaike information criterion (AIC) is a method permitting to quantify the quality of a model for a given dataset [146]. If a list of models is set, the optimal model should be the one with the minimum AIC. This criterion is well adapted for least-squares regression [147] and has been used for Doppler imaging [148]. The AIC is expressed as (Eq. (4.13)) [146]:

$$AIC = 2k + N\, ln\left(\frac{R}{N}\right) + \frac{2k\,(k+1)}{N-k-1} \tag{4.13}$$

where AIC is the Akaike information criterion, k is the degree of freedom, N is the size of the input data, and R is the sum of squares of the residuals between the input data and model. For a polynomial regression, the model list is given by the different possibilities for the order of the polynomial. For an SVD filter, the model list is composed of the reconstructed data with the kth first singular values.

Another approach has been developed for SVD clutter filtering and is based on the left singular vector representing the space. This approach was initially proposed for blood flow imaging [149], but have also been used for cavitation imaging of microbubbles [150]. After SVD, a normalized covariance matrix is computed as (Eq. (4.14)) [150]:

$$C\,(n,m) = \frac{1}{N}\sum_{k}\left(|U\,(k,n)| - \overline{|U\,(k,n)|}\right)\cdot\left(|U\,(k,m)| - \overline{|U\,(k,m)|}\right) \tag{4.14}$$

where C is the normalized covariance matrix (sometimes referred to as similarity matrix), N is the total number of pixels, and U is the left (spatial) singular vectors; $|\cdot|$ is the absolute value, and $\bar{\cdot}$ is the average value. This similarity is square defined by the number of singular vectors used for decomposition. An example of a similarity matrix for an in vivo carotid is provided in Fig. 4.9a. The very first square corresponds to the tissue components, while the second broader square is the flow. Indeed, singular vectors from flow are very similar to themselves, which leads to a square shape (the same is true for tissue). Consequently, the optimal cutoff is defined by the bottom-right corner of tissue terms, which is also the top-left corner of flow terms. A technique to find the square corresponding to the flow is to compute the normalized correlation between all the possible squares along the diagonal and

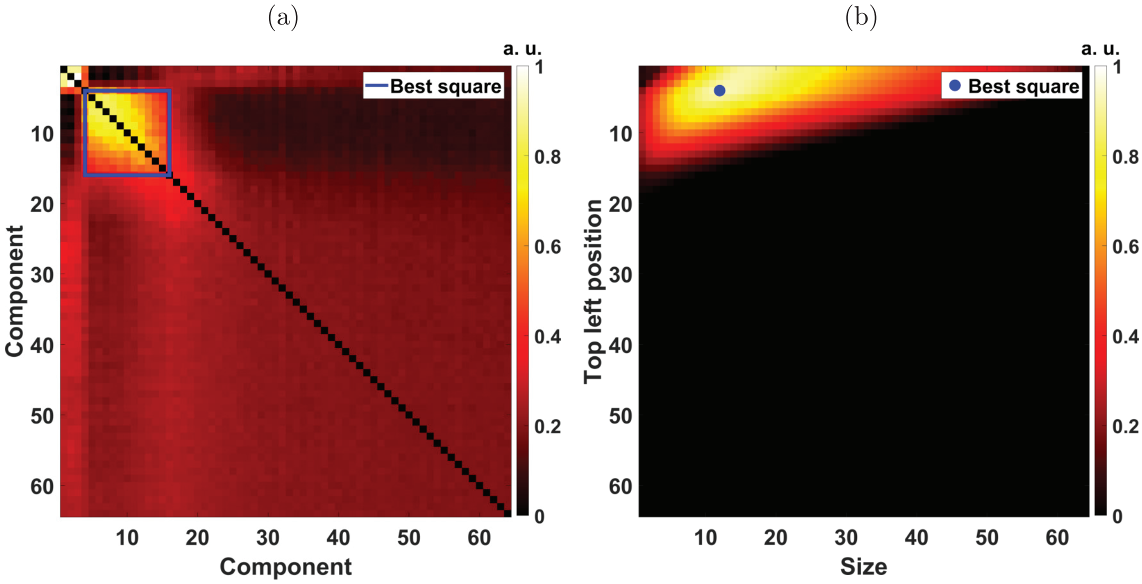

Figure 4.9: Similarity and square correlation matrices for automatic SVD clutter filtering: (a) similarity matrix, and (b) square correlation matrix of all the possible square along the diagonal of (a). The blue point in (b) represents the best correlation giving the square in (a). Computations were done using an in vivo acquisition with 64 frames for SVD.

a perfect square of the same size (Eq. (4.15)) [150]:

$$\begin{cases} \chi\left(C,\sigma_{a,b}\right) = \dfrac{1}{N_t}\sum_{n,m}\left(\left|C\left(n,m\right)\right| - \overline{\left|C\left(n,m\right)\right|}\right)\cdot\left(\left|\sigma_{a,b}\left(n,m\right)\right| - \overline{\left|\sigma_{a,b}\left(n,m\right)\right|}\right) \\ \chi_N\left(a,b\right) = \dfrac{\chi\left(C,\sigma_{a,b}\right)}{\sqrt{\chi\left(C,C\right)\chi\left(\sigma_{a,b},\sigma_{a,b}\right)}} \end{cases} \tag{4.15}$$

where χ and χ_N are respectively the non-normalized and normalized correlation (square correlation) matrices, C is the covariance matrix, $\sigma_{a,b}$ is the square base matrix with the same size than C with 1 in the square and 0 outside, a is the top-left position of the square, and b the size of the square; $|\cdot|$ is the absolute value, and $\bar{\cdot}$ is the average value. This square correlation for Fig. 4.9a is shown in Fig. 4.9b, the blue square is defined by the maximum of the square correlation matrix. Then, the top-left position of the square is the optimal cutoff for SVD clutter filtering.

4.2 Adaptive clutter filtering methods based on FIR filters

The second section of the fourth chapter presents the adaptive clutter filtering methods based on FIR filters. This section is broken down into three subsections: motivation and proposed approach, conventional approach, and adaptive approach.

In the following, the novel adaptive approach for clutter filtering is described with details concerning the filters and algorithm.

4.2.1 Motivation and proposed approach

Previously, different categories of clutter filters were described. Indeed, various types of clutter filters have been developed since the very beginning of flow estimation and Doppler technique developments such as FIR and IIR filters, polynomial regression, and eigen-based filtering. Standard FIR filtering may be implemented as a convolution in the time-domain with the impulse response, but a relatively high filter order is needed to obtain sufficient performance [135], [136]. IIR filters can also be used and have the advantage to yield the same performance as the FIR filters with a lower order, but need to be well-initialized to guarantee stability [135], [136]. Both filtering methods are set with a frequency/velocity cutoff. More recently, eigen-based filters have been proposed as another solution for separating clutter and blood signal, but they require some hypotheses or analysis to select a power threshold for the tissue signal [144]. Regression filters have also been proposed to subtract the clutter components from received signals using a polynomial or linear fitting; this method requires the selection of a polynomial basis and the order of the polynomial [135], [136].

As previously stated, clutter filtering is a crucial step in flow estimation; especially in the case of *in vivo* data with both flow and wall motion. Using a too high cutoff leads to suppression of low-velocity blood signal. Concerning the effect on the estimates, a high cutoff makes it challenging to extract low-velocity flow, which can occur close to the wall, during diastole or in case of pathology. However, using a low cutoff leads to residual clutters in the signal. The low cutoff induces biases and outliers in the estimates because of the remaining clutter. Consequently, a clutter filter with a stopband frequency following the actual tissue velocity yields a lower bias and a better flow estimate. Moreover, because the tissue velocity changes during the cardiac cycle, filters with a temporal adaptive cutoff velocity can achieve better performance than the non-adaptive filters [151].

Temporal variation of the tissue surrounding the vessel is a well-known property inherent to the cardiac cycle and the pulsatility of the vessel due to the blood circulation. However, spatial variations of the tissue velocity can also occur and are due to various phenomena such as pulse wave [152], aging [36], or plaques [153] in case of a pathological artery. Because of these spatial variations, the real tissue velocity and optimal clutter stopband frequency are not only time-dependent but

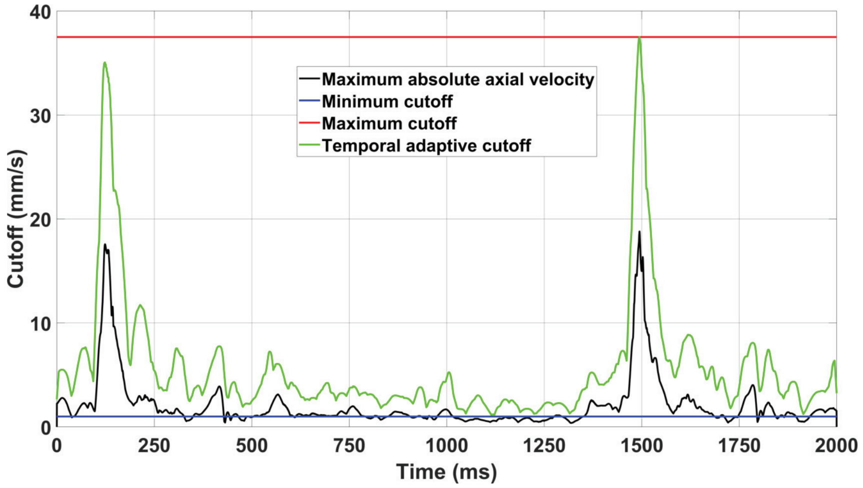

Figure 4.10: Comparison of cutoff velocities for different clutter filtering strategies.

also a function of the position relative to the tissue. Consequently, a clutter filter taking into account the spatial variation of the tissue velocity should outperform the standard clutter FIR concerning clutter rejection.

After presenting the conventional in the next section approach adaptive clutter filtering approaches, taking into account tissue velocity, will be presented. FIR filters are used for the adaptive approaches because they are always stable and because the selected cutoff is directly corresponding to tissue velocities. By estimating the tissue motion and setting the corresponding clutter filter with that estimate, we can expect more accurate flow estimates.

4.2.2 Conventional approach

A conventional approach is a non-adaptive approach, where the cutoff value is constant through the overall acquisition. Two fixed cutoffs are used: a low cutoff (minimum filter) and a high cutoff (maximum filter). The minimum FIR clutter filter corresponds to the very low cutoff arbitrary fixed. The corresponding cutoff velocity at 1 mm/s and this cutoff are shown in Fig. 4.10. The maximum FIR clutter filter has a cutoff set to two times on the maximum estimated tissue velocity estimated in all the frames. The corresponding value is approximately 37 mm/s in the example provided in Fig. 4.10.

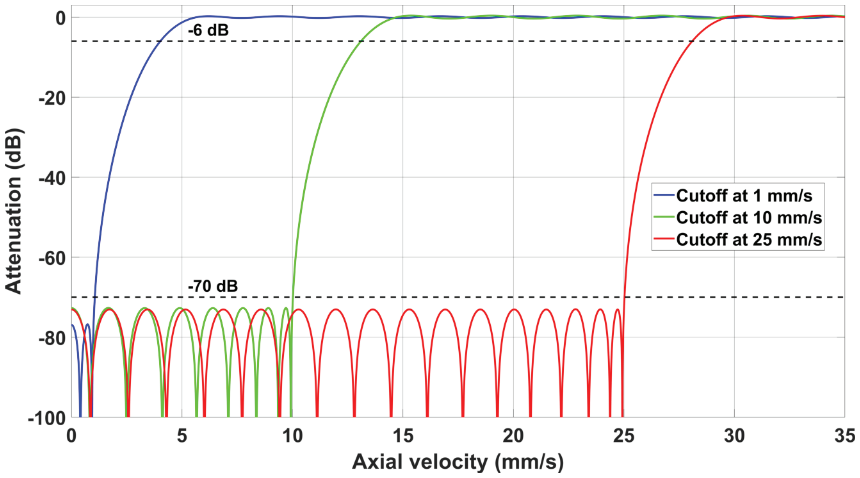

Figure 4.11: Three impulse responses of FIR filters used for temporal adaptive clutter filtering. The attenuation is set to 70 dB with an equiripple design method.

4.2.3 Adaptive approach

4.2.3.1 Temporal adaptive FIR clutter filtering

For the temporal adaptive filter, the cutoff is frame-dependent and is two times the maximum estimated velocity in that frame. This approach computes one filter per frame; an example is shown in Fig. 4.10, the two peaks at 150 ms and 1 500 ms correspond to strong expansions of the wall at the beginning of systole; such filter is in accordance with tissue motion and so cardiac cycle. The filters have all the same characteristics except for the stop frequency. An example of three different filters is in Fig. 4.11 where only the stop frequency changes from a filter to another; responses of lowest cutoff filters can be seen as a truncated version of the highest one.

4.2.3.2 Spatial and temporal adaptive FIR clutter filtering

For the spatial and temporal adaptive filtering, the concept is to go even further than the previous one by including the PSF (measured or simulated) as a criterion to spatially computes filters; one filter is calculated per pixel and frame. The upside-down PSF attenuation is used since, by positioning it on a pixel, that indicates the contribution of other pixels at this point with their respective attenuation. The process for one pixel at a specific time can be broken down into four steps (Fig. 4.12):

1. A $n \times m$ window surrounding the pixel of interest is created based on the beamformed PSF at n dB (corresponding to the attenuation target of the

filter).

2. Each pixel in this $n \times m$ window may influence the pixel of interest. The contribution of each pixel, in terms of tissue velocity in this window, are listed with their respective contribution using the upside-down PSF.
3. For each combination PSF/velocity (each pixel) a filter candidate is calculated. The filter is extracted from a pre-computed dictionary of filters[†], all designed with the same characteristics so that the attenuation at the tissue velocity is the target attenuation minus the PSF attenuation at that point; this process returns a cutoff lower than the tissue velocity like in the example in Fig. 4.13. At this step, $n \times m$ filter candidates are listed.
4. From the $n \times m$ filter candidates, the selected filter for the center of the window at that frame is the one with the highest cutoff. This criterion permits to remove the more severe tissue contribution that has contributed to the central pixel.

This process is repeated for each filter and each frame to get one filter per frame and pixel. Afterward, the filtering can be done like a classic FIR clutter filtering except that the filter in the convolution is unique to each pixel and frame.

4.3 Experiments

The third section of the fourth chapter presents the experiments. This section is broken down into three subsections: material and methods, results, and comparison with an SVD data-driven clutter filtering method. In the following, the adaptive approach for clutter filtering is validated *in vivo* with comparison using standard approaches and a comparison with an SVD data-driven technique.

[†] A dictionary is used to reduce the computation load. Indeed, even if filter design is well optimized the typical duration for design is 0.1 s on an Intel® Core™ i7-6700 CPU; with about 100 000 pixels per frame in this work, this results in approximately 166 minutes of computing time per frame just for filter design. While a pre-computed dictionary of filters from a cutoff of 0 cm/s to 10 cm/s with a discretization step of 0.01 mm/s is composed of 10 000 filters and needs 16 minutes to be computed. Filters are then computed once for all acquisitions. This approach replaces the filter design with a filter selection, which is done almost without machine calculation inside the pipeline.

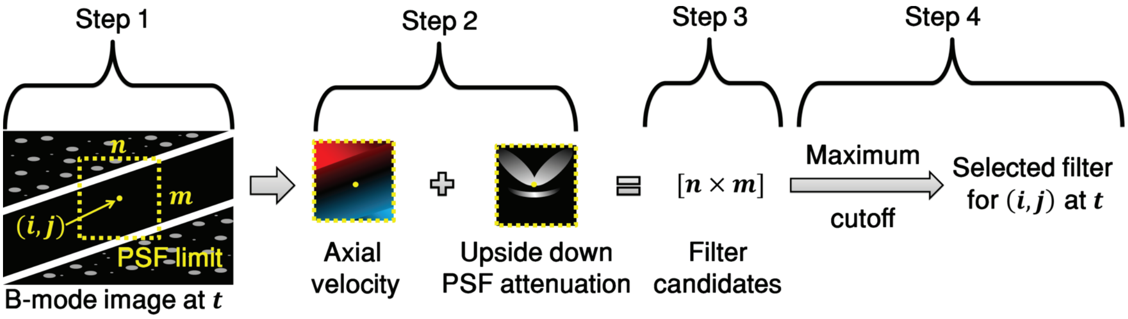

Figure 4.12: Block diagram of the algorithm to compute the spatial and temporal adaptive filters: (1) select a pixel of interest at a position (i, j) at t, (2) select the estimated axial tissue velocities in the $n \times m$ pixel region determined by the size of the PSF, (3) by combining the tissue velocity with the upside-down PSF attenuation calculated $n \times m$ filter candidates, and (4) the selected filter for the position (i, j) at t if the filter with the maximum cutoff, indeed each pixel in that area have a contribution at (i, j) so the more severe filter is considered. An iteration is done on all the pixels and frames to compute all the filters.

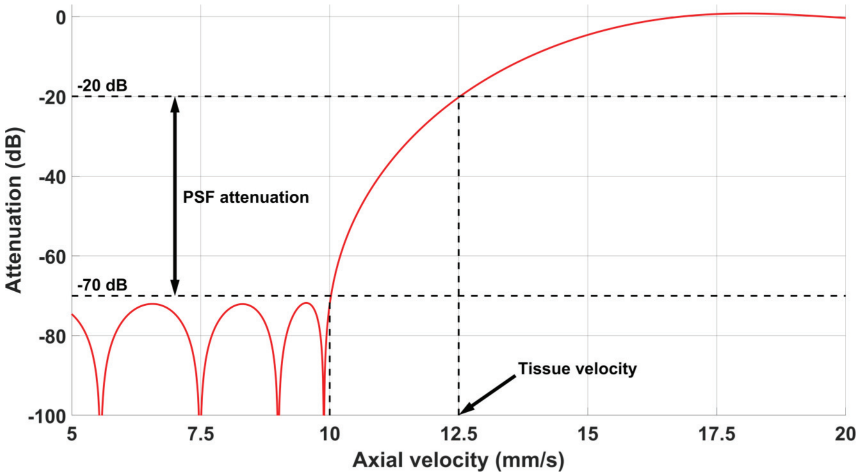

Figure 4.13: Computation of an FIR filter with the PSF attenuation and tissue velocity. In this example for the pixel, the PSF attenuation is −50 dB with a tissue velocity of 12.5 mm/s. The cutoff of the filter is set at 10 mm/s to get 20 dB attenuation at the tissue velocity providing the attenuation target of 70 dB with the PSF attenuation of 50 dB.

Table 4.1: Acquisition parameters for the adaptive clutter filtering study

Parameter	**Value**
Probe	L7-4, ATL Phillips
Number of elements	128
Pitch	298 μm
Central frequency	5.208 MHz
Sampling frequency	20.832 MHz
Excitation pulse	3-cycle sinusoidal
Pulse apodization	None (rectangular)
Speed of sound	1 540 m/s
Pulse repetition frequency	5 000 Hz
Compounding	No (single plane wave)
Steering angle	0° (horizontal plane wave)
Transmit and receive apodization	Rectangular
F-number	1.5

Table 4.2: Estimation parameters for the adaptive clutter filtering study

Parameter	**Tissue**	**Flow**
TO wavelength	N/A	0.8 mm
FWHM of TO	N/A	2.5 mm
Lag	1 frame (0.2 ms)	1 frame (0.2 ms)
Ensemble length	16 frames (3.2 ms)	64 frames (12.8 ms)
Spatial window	Hann	Rectangular
Spatial window size	1 mm (axial) × 2.5 mm (lateral)	1 mm (axial) × 2.5 mm (lateral)

4.3.1 Material and methods

For acquisitions, a Verasonics Vantage$^{\text{TM}}$ 256 system (Verasonics, Redmond, Washington, United States) with the L7-4 (ATL Philips, Bothell, Washington, United States) probe were used. Acquisition parameters are described in Tab. 4.1 and data were beamformed using a DAS algorithm with an f-number of 1.5 without apodization to maximize the power of signals since acquisitions are *in vivo* carotids. Acquisitions were performed on healthy volunteers, six subjects under the age of thirty who stood at rest 20 minutes before the acquisition. This procedure was performed to ensure that all phenomena which occur during acquisitions are entirely natural. Before clutter filtering, axial tissue velocities were estimated based on the complex autocorrelation of beamformed signals as described in Tab. 4.2. Because tissues can be subject to local and rapid velocity changes, a Hann window was applied for spatial filtering to avoid oversmoothing with a relatively small ensemble

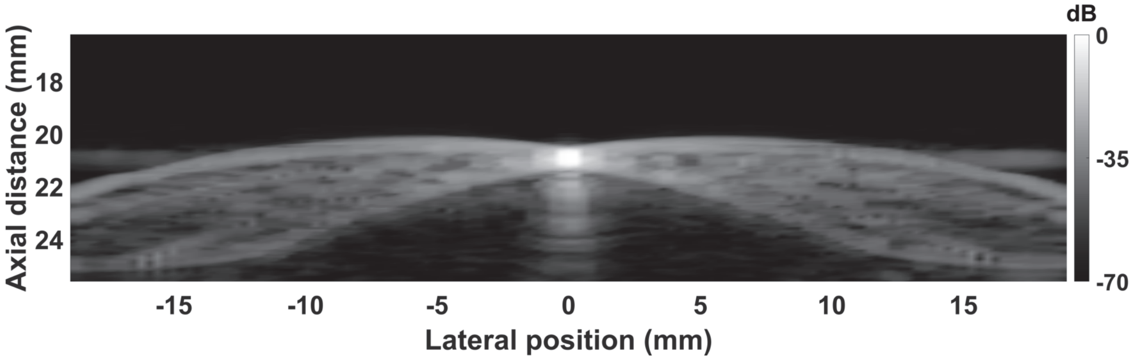

Figure 4.14: Measured PSF on a surgical wire. The PSF was measured on a 30 μm surgical wire and beamformed using the same parameters than for volunteer imaging.

Table 4.3: FIR filter parameters for the adaptive clutter filtering study

Parameter	Value
Method	Equiripple
Order	200
Attenuation	70 dB
Ripple	3 dB
Minimum cutoff	1 mm/s
Discretization step	0.01 mm/s

(16 frames) compared to flow (rectangular window with 64 frames for ensemble). For FIR filter design, the beamformed PSF was estimated on a surgical wire with a diameter of 30 μm in water along the central axis of the probe and a representative depth of the carotid (Fig. 4.14). FIR filters were computed using the characteristics described in Tab. 4.3; those filters have the same overall characteristics as the ones in Fig. 4.11. After clutter filtering, the flow was estimated using transverse oscillation with the 2D phase-based estimator with the parameters in Tab. 4.2.

4.3.2 Results

From the six volunteers, tendencies and results are similar for the minimum and maximum filters. At the very beginning of systole corresponding to the moment where tissue start moving, filters have completely different behaviors, the minimum filter (Fig. 4.15a) permits to extract a parabolic flow with an overall low moving flow while the maximum filter (Fig. 4.15b) is completely biased by the noise since both wall and flow have been removed due to the high cutoff. The minimum filter is unable to estimate the flow at the systolic peak (Fig. 4.15c) because of the remaining clutter due to the low cutoff. Indeed, at the systolic peak, the tissue is moving then the estimates are biased toward zero due to slow-moving (compared to the flow)

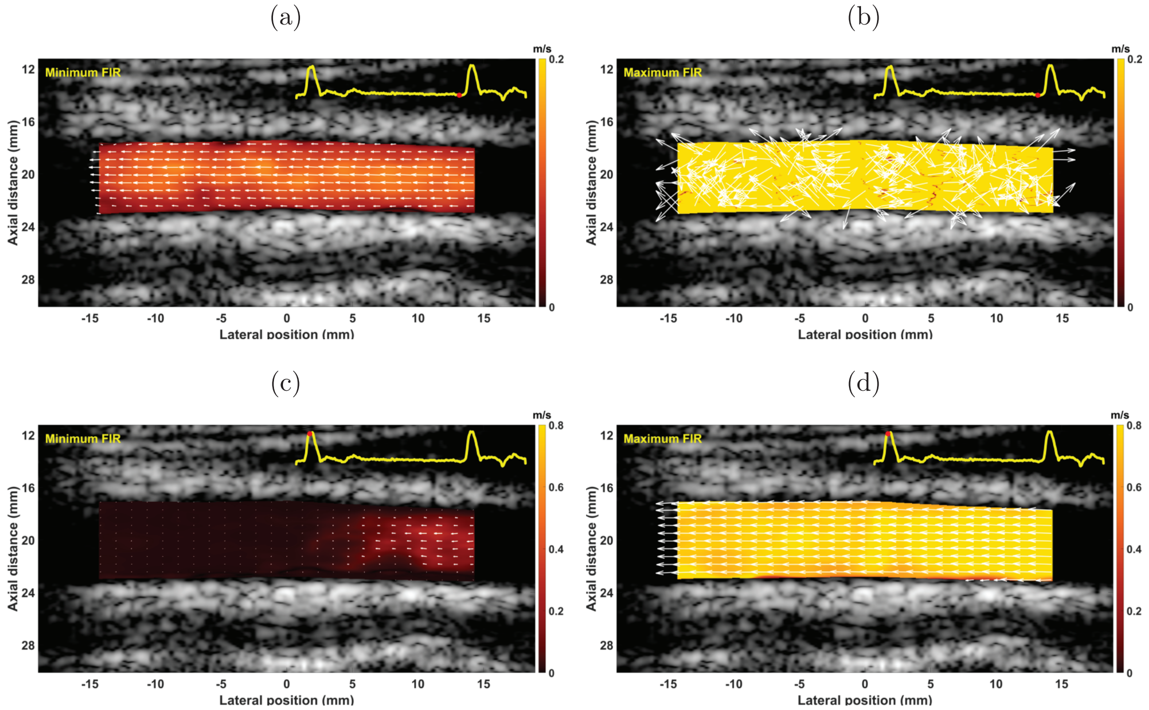

Figure 4.15: Vector flow with the minimum and maximum FIR filters: (a) flow at early systole with the minimum filter, (b) flow at early systole with the maximum filter, (c) flow at systolic peak with the minimum filter, and (d) flow at systolic peak with the maximum filter. Top-left curves represent the current position in the cardiac cycle based on the lateral flow estimate at the center of the vessel. Colorbar ranges are different for early systoles and systolic peaks, and the dynamic range is 40 dB.

components. During this phase, the maximum filter (Fig. 4.15d) seems to estimate more accurately the flow due to the high cutoff, but the flow does not reach zero at the wall as expected if we assume a parabolic flow. That effect could be explained by overfiltering close to the wall that leads to an overestimation of the phase shifts.

From the six volunteers, two acquisitions yield observable differences in terms of flow estimates with the adaptive filters. For comparison, the flow was extracted at early systole, mid systole, and systolic peak for both adaptive filters (Fig. 4.16). At early systole, the temporal adaptive filter (Fig. 4.16a) is less accurate along the upper wall than the spatial and temporal adaptive filter (Fig. 4.16b). Indeed, at this specific time, the pulse wave arrives from the left and tissue velocity depends on the lateral position; as illustrated in Fig. 4.17 showing the axial upper wall velocity at that frame depending on the lateral position. Consequently, local variations of tissues lead to such differences in flow estimates since the temporal adaptive filter is based on the maximum axial tissue velocity in that frame. In mid systole spatial and temporal adaptive filter (Fig. 4.16c) permits to get a better-looking flow close to the wall than the temporal adaptive filter (Fig. 4.16d). This effect is particularly noticeable along the lower wall at the left part of the image. At systole, both filters give similar flow estimates (Figs. 4.16e and 4.16f) because, at this moment, the tissue motion is the same along the wall.

The observations are summed up in Fig. 4.18 with the temporal flow evolution in the center of the vessel and along the wall. In the center of the vessel (Fig. 4.18a) the minimum filter is accurate only when the wall is stationary while the maximum filter has the opposite behavior. Both adaptive methods yield expected flow estimates throughout the overall cardiac cycle and cannot be genuinely distinguished. However, close to the wall (Fig. 4.18b) the spatial and temporal adaptive filter outperforms the temporal adaptive filter in case of strong and localized wall velocity that can occur during early systole, for instance. Apart from those brief moments, they have very similar behaviors. Both adaptive filters outperform the non-adaptive ones and using a spatial and temporal clutter filter to estimate a local cutoff flow permits to get closer to the wall for specific cases (2 out of 6 volunteers).

4.3.3 Comparison with an SVD data-driven clutter filtering method

To evaluate the performance of SVD data-driven clutter filters, vector flow was extracted on 3 *in vivo* carotids with the acquisition parameters described in Tab. 4.1. The temporal adaptive filter was designed as previously explained with the parameter in Tab. 4.3. AIC and covariance techniques were implemented as described previously and used to estimate optimal cutoff with an ensemble of 200 frames, which is the length of the FIR filter. Motions were extracted as described in Tab. 4.2.

Results are shown and compared for a volunteer in Fig. 4.19 at late diastole. It seems that the cutoffs (Fig. 4.19a) are almost identical for the covariance technique and a manually selected cutoff; however, the AIC seems to overestimate this cutoff. Both manual (Fig. 4.19c) and covariance (Fig. 4.19e) technique give similar flow estimates. However, the temporal adaptive FIR approach (Fig. 4.19a) can extract the flow closer to the upper wall. Concerning the AIC (Fig. 4.19d) the flow estimate is only noise; this effect was expected since the cutoff was overestimated (Fig. 4.19a) compared to other SVD approaches.

The overestimation of the cutoff with the AIC technique can be explained by looking at the AIC curve (Fig. 4.20). The curve is very flat, then the minimum has no real meaning and leads to a wrong cutoff. It is not simple to explain this effect since the

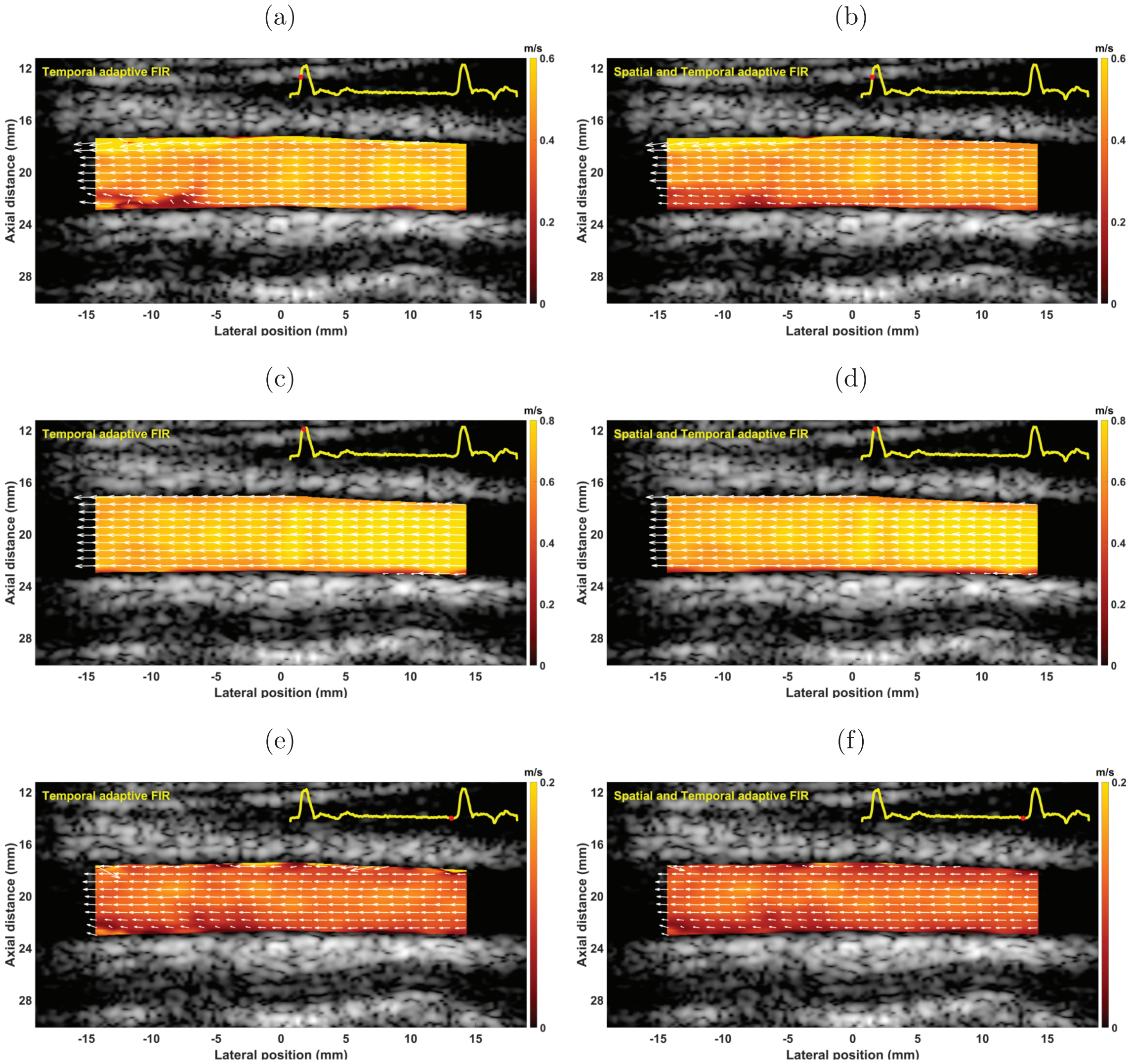

Figure 4.16: Vector flow with the adaptive FIR filters: (a) flow at early systole with the temporal adaptive filter, (b) flow at early systole with the spatial and temporal adaptive filter, (c) flow at mid systole with the temporal adaptive filter, (d) flow at mid systole peak with the temporal adaptive filter, (e) flow at late diastole with the temporal adaptive filter, and (f) flow at late diastole with the spatial and temporal adaptive filter. Top-left curves represent the current position in the cardiac cycle based on the lateral flow estimate at the center of the vessel. Colorbar ranges are different for early systolic and other phases, and the dynamic range is 40 dB

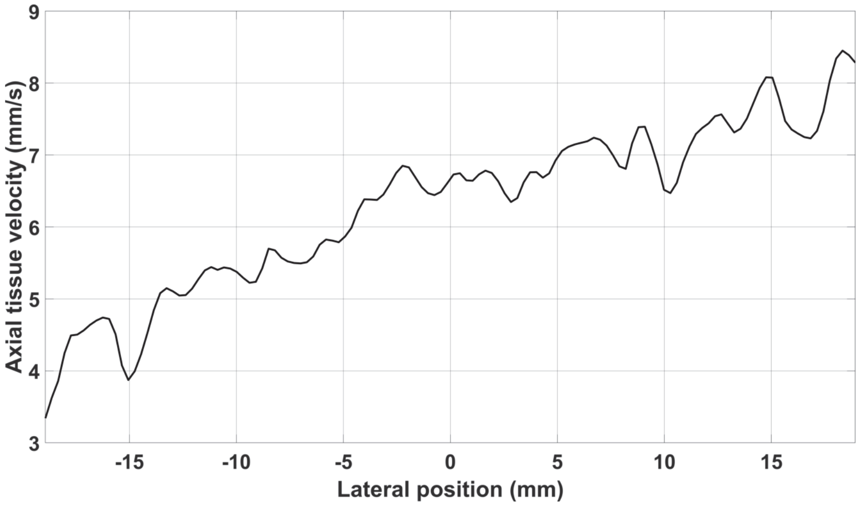

Figure 4.17: Axial wall velocity depending on the lateral position at early systole. Pulse wave arrives from the right, creating a tissue velocity gradient along the wall. The upper wall is considered in this plot.

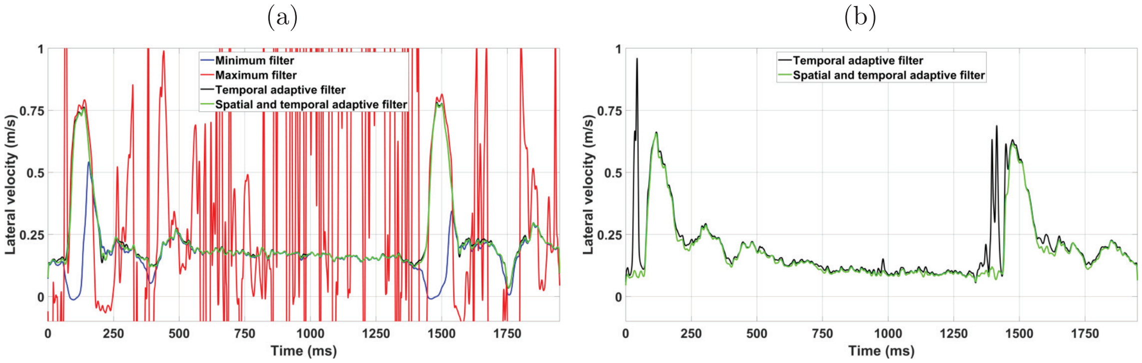

Figure 4.18: Temporal evolution of flow estimates depending on the clutter filtering strategy: (a) flow estimates in the center of the lumen, and (b) flow estimates 1 mm away from the middle of the upper wall.

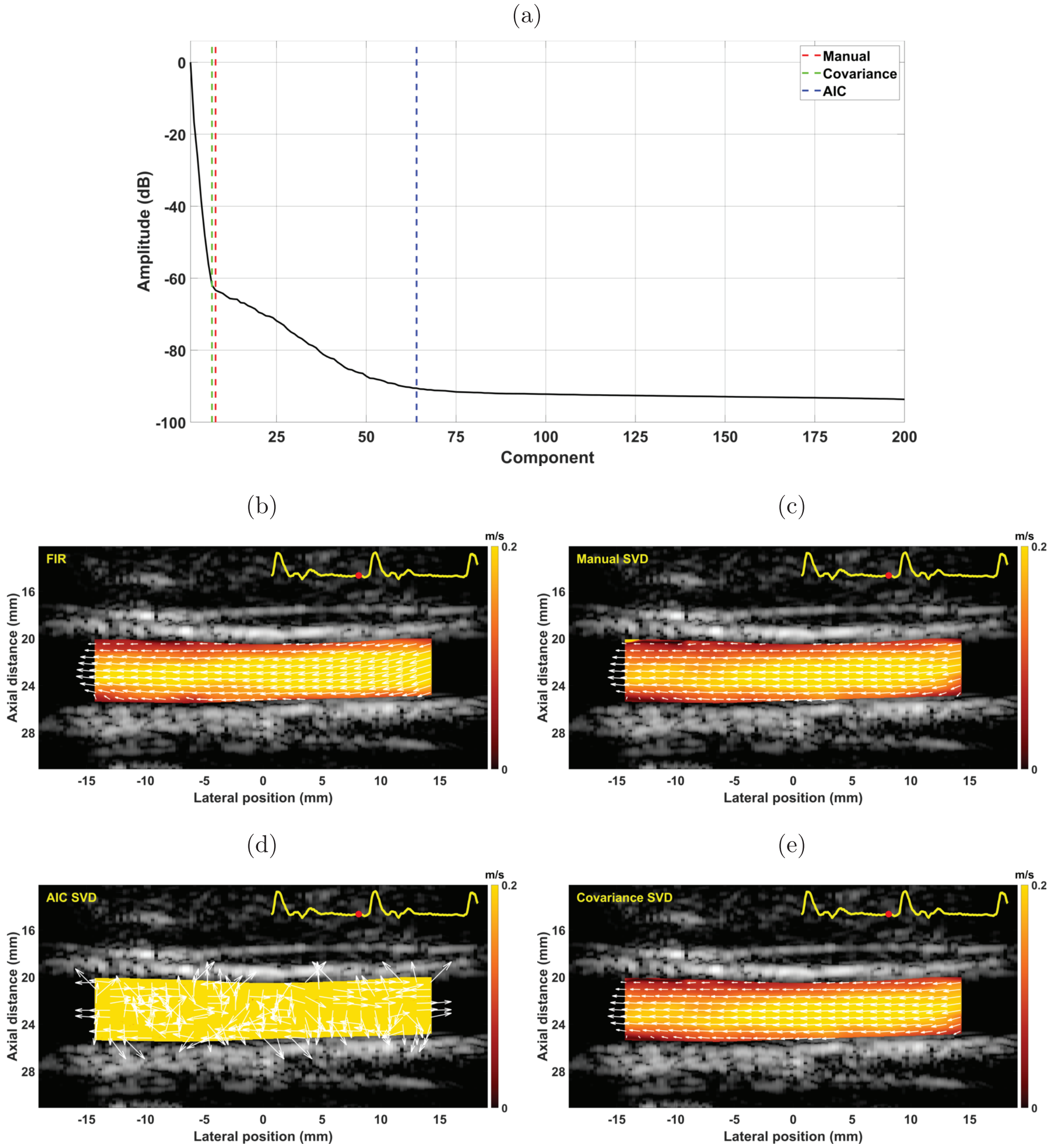
(a)
(b)
(c)
(d)
(e)

Figure 4.19: Vector flow imaging with the SVD data-driven and FIR clutter filters: (a) cutoffs for the SVD approaches, (b) vector flow with the temporal adaptive clutter filter, (c) vector flow with a manual SVD cutoff, (d) vector flow with a data-driven SVD cutoff based on AIC, and (e) vector flow with a data-driven SVD cutoff based on the covariance of the spatial singular vectors. For all approaches, the same ensemble of 200 frames was used in late diastole. Top-left curves represent the current position in the cardiac cycle based on the lateral flow estimate at the center of the vessel. The dynamic range is 40 dB.

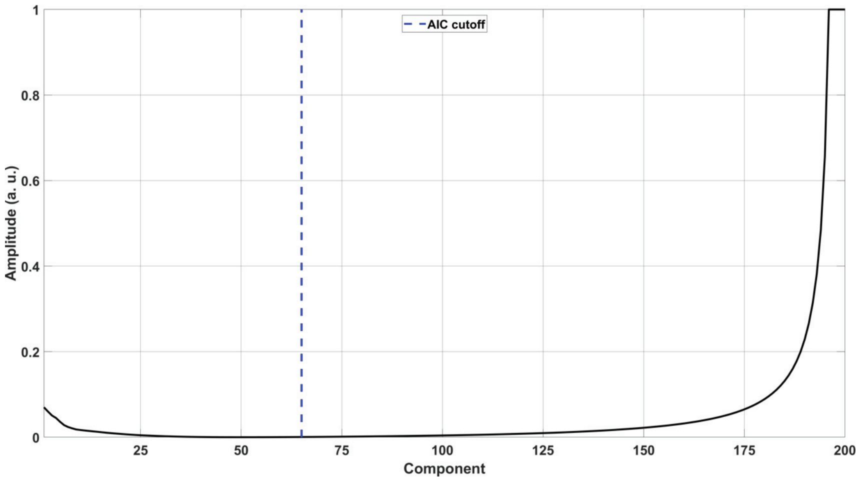

Figure 4.20: Example of a poorly defined AIC curve. The cutoff corresponds to the minimum AIC.

AIC technique comes from statistical modeling and information theory. A possible explanation is that the statistical distribution of the spatial singular vectors does not follow a normal distribution as assumed by the AIC technique. Another possibility is that the penalization used by AIC is unsatisfactory[†].

For specific phases of the cardiac cycle, the covariance technique also failed to estimate the cutoff. An example is provided in Fig. 4.21, which is in early systole a few milliseconds before the systolic peak. In this example, the covariance matrix (Fig. 4.21a) does not present a square well defined for the flow, which leads to a wrong square fitting by the similarity matrix (Fig. 4.21b). Indeed, during this cardiac phase, the flow accelerates through the artery. Combining this acceleration with the large flow velocity range, the similarity of flow terms is decreasing from one term to another and flow terms do not describe a square but the limit (Fig. 4.21a) is blurred between flow terms and noise.

4.4 Usability and clinical interest

In this chapter, clutter filtering techniques have been introduced and presented; FIR, IIR, polynomial regression, and SVD clutter filters were described. Moreover, temporal adaptive approaches using FIR filters based on tissue estimates and PSF were also widely described. Approaches were compared to each other

---

[†] A workaround is to use the Bayesian Information Criterion (BIC), which is similar to AIC but induces a higher penalization for models. The main difference is that AIC selects the model that most adequately describes an unknown, while BIC finds the true model among the set of candidates. If both AIC and BIC failed in case of overfitting/underfitting, then other criteria such as normalized maximum likelihood can be used, but at a high computational cost.

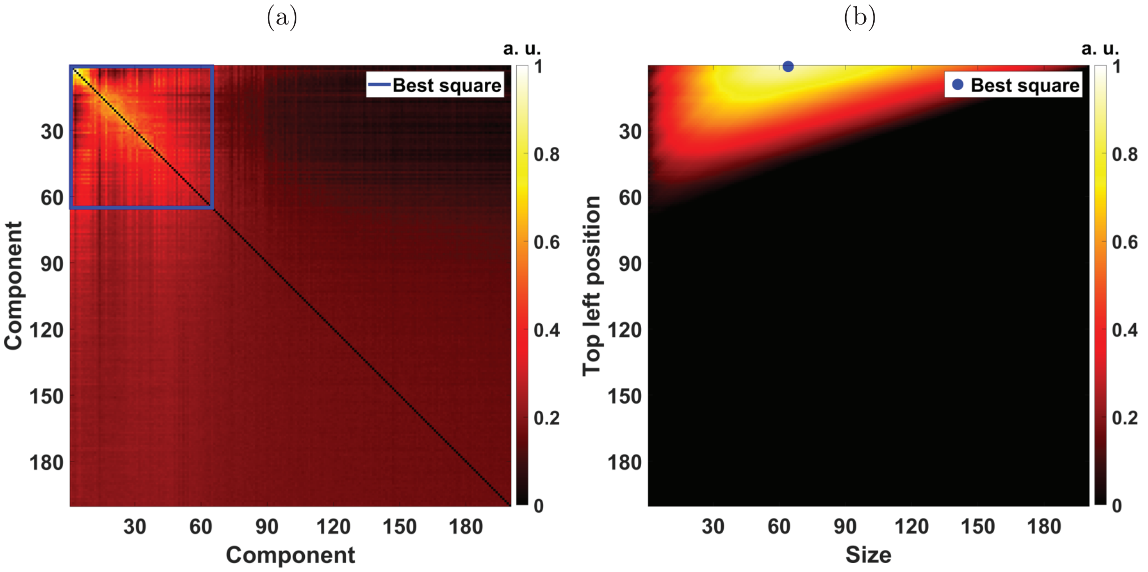

Figure 4.21: Similarity and square correlation matrices for automatic SVD clutter filtering in a bad case scenario: (a) similarity matrix, and (b) square correlation matrix of all the possible square along the diagonal of (a). The blue point in (b) represents the best correlation giving the square in (a). Computations were done using an *in vivo* acquisition with 200 frames for SVD in early systole.

with *in vivo* acquisitions. Results showed that the temporal adaptive approaches outperform the standard techniques concerning FIR clutter filters; FIR filters were considered because they are always stable and can be directly set with the estimated tissue velocity to remove clutter. Also, SVD filters are more and more used in the literature and described as powerful techniques. However, it has been shown that the temporal adaptive approach gives similar results that data-driven SVD clutter filters or outperform those SVD approaches. That means that knowing the actual tissue velocity permits to get better clutter rejection that data-driven techniques. The temporal adaptive approach developed in this chapter is consequently validated for extensive use.

Since temporal adaptive approaches based on tissue estimates outperforms the other approaches, they are going to be used in the next chapter for clinical acquisition. However, only the temporal adaptive approach will be considered and not the spatial and temporal approach. Indeed, even it was useful for particular cases and cardiac phases, the computational load is very high compared to the other adaptive approach. Such filters will lead to accurate estimates in pathological cases with plaques, or other diseases which lead to abnormal wall motion with high wall velocity during cardiac cycles.

Chapter 5

Toward Clinical Routine: Proof Of Concept

The fifth and last chapter is a step toward clinical use of the simultaneous tissue and flow measurement methods developed, and it consists of a clinical trial on carotids from both volunteers and patients. The methods and material used, as well as the description of the population, are first given. However, since they were already described earlier in the manuscript, the reader will be mainly refereed to the previous chapters regarding methods. Then, the metrics extracted during the clinical proof of concept are detailed. Finally, results are reported through qualitative inspection, values of the metrics, and a presentation of an additional case, which is internal carotid stenosis. The chapter concludes with the limitation, opportunities, and future works to go further in clinical usability.

There is one article submitted in *IEEE Transactions on Ultrasonics, Ferroelectrics, and Frequency Control* as evidence of the scientific contribution: “Simultaneous vectorial blood flow and wall motion imaging in the carotid artery: a clinical proof of concept” (2019). The clinical proof of concept was conducted in St. Olavs Hospital, Trondheim, Norway, and during a two months doctoral stay in the Department of Circulation and Medical Imaging in the Norwegian University of Science and Technology, Trondheim, Norway.

5.1 Material and methods

The first section of the fifth chapter presents the material and methods. This section is broken down into three subsections: patient and volunteer populations, tissue motion and flow estimation methods, and metrics/markers extracted from measurements. In the following, the pipeline is described from acquisitions to the extraction of carotid properties.

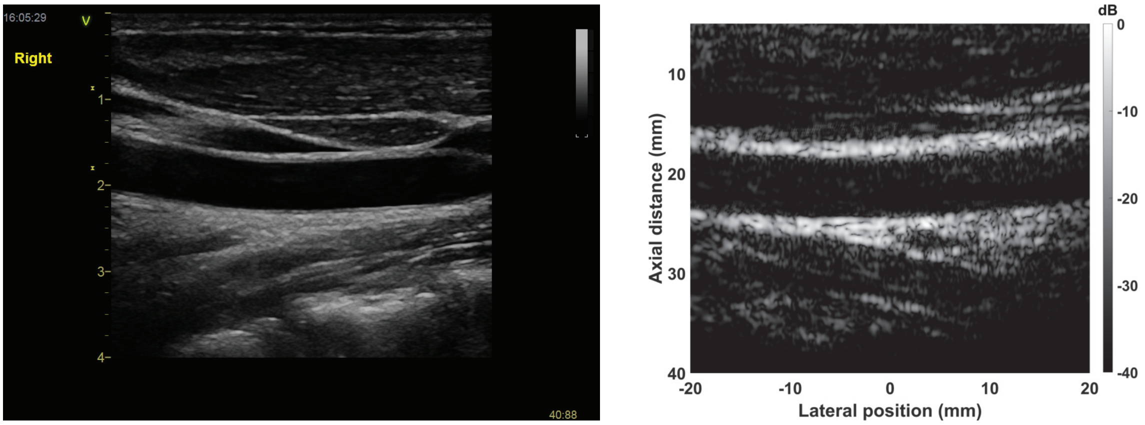
(a) (b)

Figure 5.1: Acquisition of a carotid with the medical and research scanners: (a) carotid of a volunteer acquired with the medical scanner, and (b) same carotid with the research scanner. The view is slightly different due to the different positioning of the probes and potential patient movement from one acquisition to another.

5.1.1 Patient and volunteer populations

Thirteen patients from St. Olavs Hospital, Trondheim, Norway, were recruited in this clinical proof of concept, as well as twelve healthy volunteers. The clinical proof of concept received approval from the research ethics board, and the written consent of each person participating in the study has been obtained before the examination. Carotids were recorded using a Verasonics Vantage$^{\text{TM}}$ 256 system (Verasonics, Redmond, Washington, United States) with a 9L-D (General Electric Company, Boston, Massachusetts, United States) linear probe array, following a standard clinical routine examination using a Vivid$^{\text{TM}}$ E95(General Electric Company, Boston, Massachusetts, United States) ultrasound system. Before imaging, thermal and acoustical measurements were conducted to estimate thermal and mechanical indexes (TI and MI), in addition to the heating measurement of the transducer surface. Also, the MI and TI values are updated and shown in real-time on the scanner during imaging of the patient for the navigation acquisition sequence. All measurements are within the limits set by the international standard IEC 60601-2-37:2004 [154]. All acquisitions were performed in the hospital by cardiologists (Fig. 5.1).

Both common carotid arteries (left and right) were imaged for 12 patients as well as for volunteers; the remaining patient is an additional case of stenosis in the internal carotid artery. Among the 24 common carotid arteries of the patients, 3 present too much out-of-plane motion, and 2 have a too strong clutter signal in the data to be processed and are thus discarded from the study. All the other acquisitions

Table 5.1: Acquisition parameters for the clinical proof of concept

Parameter	**Value**
Probe	9L-D, GE
Number of elements	192 elements
Pitch	229 μm
Transmit frequency	4.8 MHz
Sampling frequency	19.2 MHz
Transmit pulse	2.5 cycles
Speed of sound	1 540 m/s
PRF	12 000 Hz
Compounding	2 plane waves
Steering angles	$[-15°; 15°]$
Transmit and receive apodization	Rectangular
Images per second	6 000
Acquisition duration	1.5 s
F-number	1.5

(volunteers and additional case) were suitable for the clinical proof of concept.

Patients (19 carotids) were subdivided into two categories: without any apparent pathology (13 carotids) or with an apparent pathology (6 carotids) detected by the cardiologist during the clinical exam. In the pathological subgroup, 2 carotids were scanned on a patient who had a stroke, 1 had stenosis located further down along the artery, 2 presented plaques, and 1 was calcified. To identify also potential modifications of the different parameters linked to aging, volunteers (24 carotids) were also separated into two subgroups: younger than 35 (18 carotids) or 35 years of age and older (6 carotids); the threshold at 35 was chosen subjectively.

To achieve a high frame rate (6 000 Hz) with a large field of view, a two plane wave acquisition scheme was used. Ultrasound images were compounded after beamforming to increase SNR before estimation or further processing. Acquisition parameters are summarized in Tab. 5.1. Channel data were recorded from the research scanner, after which beamforming and processing were performed offline.

5.1.2 Tissue motion and flow estimation

The pipeline used for the extraction of both tissue motion and flow is the one presented in chapter 3 (Fig. 3.7) with the estimation parameters in Tab. 5.2. Regarding clutter filtering, the temporal adaptive filter presented in Chapter 4 was applied with the same settings (Tab. 4.3) to improve the estimates compared to standard clutter filtering methods with a relatively short computation time

Table 5.2: Estimation parameters for the clinical proof of concept

Parameter	**Tissue**	**Flow**
TO wavelength	N/A	0.8 mm
FWHM of TO	N/A	2.0 mm
Lag	12 frames (2 ms)	1 frame (0.17 ms)
Ensemble length	1 frame (0.17 ms)	60 frames (10 ms)
Spatial window	Hann	Rectangular
Spatial window size	1 mm (axial) × 2 mm (lateral)	1 mm (axial) × 2 mm (lateral)

considering the large volume of data acquired.

5.1.3 Metrics extracted from measurements

As explained in Chapter 1, the development of cardiovascular diseases influences the flow field as well as the properties of the vessel wall. After motion estimation, several characteristics can be extracted. The following are the quantitative parameters that are estimated and described in Chapter 1.

Parameters obtained from the wall velocity estimates:

- Wall velocity range (ΔV_{wall}, mm/s)
- Mean diameter ($\bar{d}$, mm)
- Distensibility (D, %)

The wall velocity range is the difference between the maximum and minimum wall velocity during the cardiac cycle. This value represents the ability of the vessel to deform itself due to mechanical waves and blood pressure. It is expected to decrease when the arterial wall thickness or stiffness increases. The mean diameter is averaged over several cardiac cycles and the entire field of view. Pathologies can influence geometry and hence this value; remodeling that occurs with age also contributes to modify this parameter. The distensibility is the relative difference between the largest and smallest diameter during the heart cycle. This value represents the compliance of the artery; stiff and calcified arteries are less compliant than healthy ones.

Parameters obtained from the flow velocity estimates:

- Peak systolic velocity (PSV, m/s)
- Resistivity (RI, %)
- Backflow (B, percentage of acquisitions with backflow in the group, %)

Peak systolic velocity is measured globally and is calculated using the vector velocity field. This value is directly related to the maximum blood flow rate. In the case of narrowing upstream, this value increases; also, the overall remodeling and compliance of the arterial system influence this velocity. The resistivity index is the ratio between end-diastolic velocity (EDV, m/s) and peak systolic velocity (PSV, m/s); both velocities were selected based on the flow profile without ECG. This parameter is related to the vascular resistance of the downstream vascular bed. In the case of atherosclerosis, it is affected by both upstream and downstream locations. The waveform can be mono or triphasic in arteries. Triphasic flow indicates a backflow during cardiac cycles. In a healthy carotid artery, backflow does not occur. If observed, it would indicate a malfunction of blood circulation; the value is in percent, which indicates the proportion of acquisitions with backflow in each group.

Advanced measurements:

- Pulse wave velocity (PWV, m/s)
- Mean wall shear rate ($mWSR$, s^{-1})
- Peak wall shear rate ($pWSR$, s^{-1})

The pulse wave velocity is related to the stiffness of the vessel. For each carotid, the PWV is the averaged value of the measurements on both upper and lower walls using as many cardiac cycles as possible (typically between 1 and 3). The wall shear rate, calculated from the flow, provides indirect information on the shear forces applied onto the vessel wall. Both mean and peak wall shear rate were extracted as potential indicators of pathologies, and were estimated 1 mm away from the wall.

Statistical tests were also performed. Except for the backflow, a normal distribution with an unequal variance for the measurements was assumed, and a Welch's t-test was used. This statistical test is an adaptation of Student's t-test, but it is more reliable in case of unequal variances and unequal sample group sizes which is the case of this study. For the backflow, because this parameter is a categorical variable, the p-values cannot be evaluated using the previous test. To compute the p-values in such a case the Fisher's exact test was used. This statistical test is based on the analysis of a contingency table. Because p-values were calculated with a limited number of patients and volunteers, small p-values indicate a significant difference in that study but cannot be extrapolated outside of the current study. Statistical tests are then used to prove that the approach can point out differences between groups in a clinical environment.

5.2 Results

The second section of the fifth chapter presents the results. This section is broken down into three subsections: qualitative inspection, carotid properties, and internal carotid stenosis. In the following, all results of the clinical proof of concept from all material are reported.

5.2.1 Qualitative inspection

The approach permits to do qualitative inspection due to the simultaneous wall and flow velocity measurements. Indeed, it becomes possible to study and visualize both characteristics at the same time. An example of visualization is showed in Fig. 5.2. For one of the volunteers (Figs. 5.2a, 5.2c and 5.2e), flow is mainly parabolic during the cardiac cycle without any backflow or unusual flow pattern, and the wall moves in correspondence to the cardiac cycle. For one of the patients (Figs. 5.2b, 5.2d and 5.2f), who was admitted for having a stroke with plaques and calcifications, the diameter of the artery is larger compared to the volunteer. The flow shows an unusual pattern at the systolic peak (Fig. 5.2d) close to the upper wall with a low flow region, the wall is not moving around this region, and the flow is globally slower compared to the volunteers. At the end of the systole (Fig. 5.2f), a complex flow pattern occurs with backflow in the carotid, and a vortex close to the carotid bifurcation (left of the image) can be visualized.

5.2.2 Carotid properties

For quantitative measurements, groups are compared regarding the tissue estimates (Fig. 5.3), flow measurements (Fig. 5.4), and carotid properties (Fig. 5.5). Tabs. 5.3 and 5.4 summarize all the results with the mean and standard deviations while p-values are reported in Tab. 5.5.

The wall velocity range (ΔV_{wall}, Fig. 5.3a) decreases with age and between volunteers and patients; it can further separate young volunteers from older volunteers, and volunteers from patients. The diameter of the artery ($\bar{d}$, Fig. 5.3b) is significantly larger for patients than for volunteers; it can be used to separate both groups. However, no significant differences can be observed within the groups. The results show that distensibility (D, Fig. 5.3c) decreases with age and was lower for patients

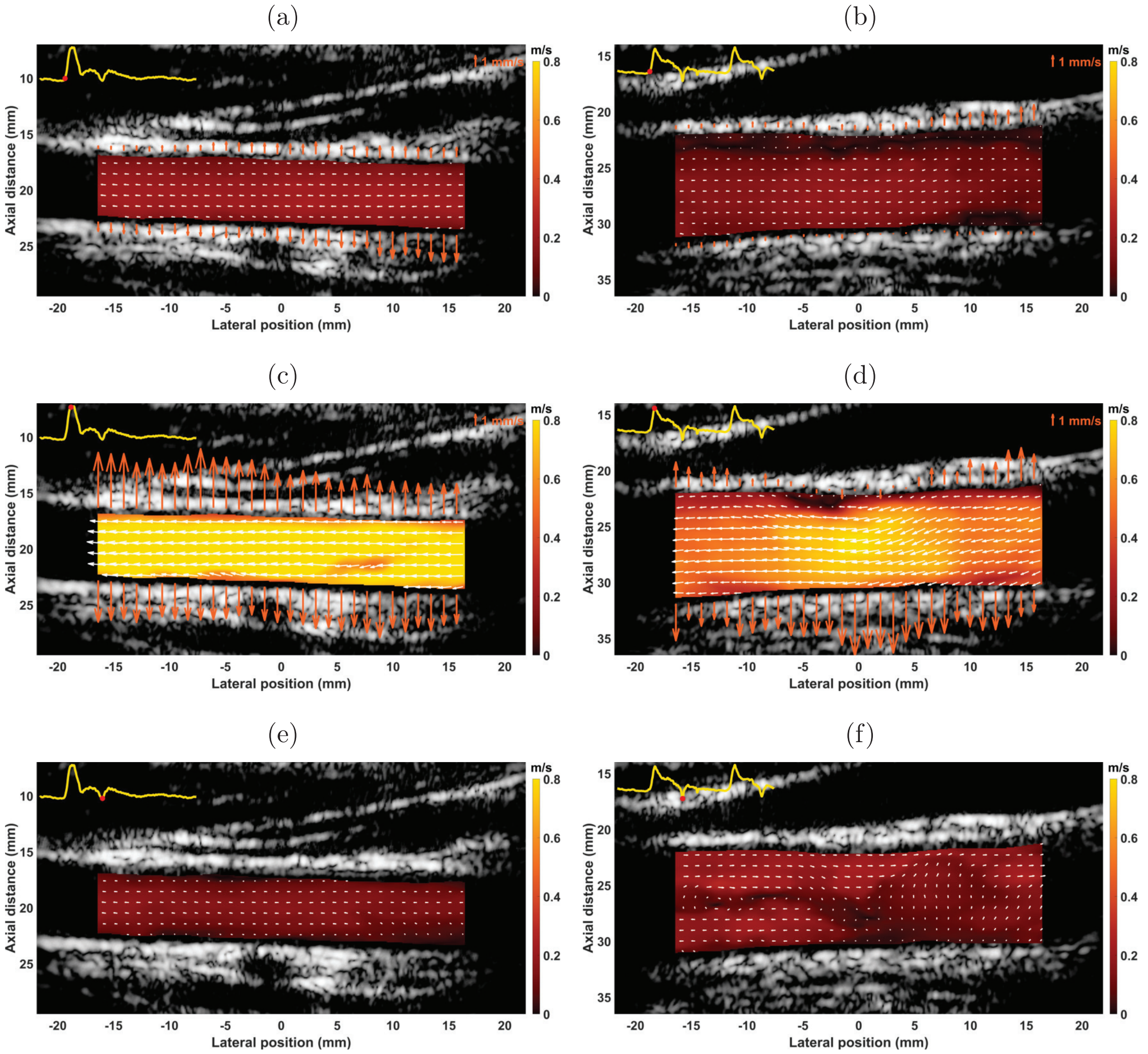

(a) (b) (c) (d) (e) (f)

Figure 5.2: Flow and tissue velocity estimates superimposed onto B-mode images for a volunteer (a, c, e) and a patient (b, d, f): (a, b) is at the very beginning of the systole, (c, d) at the systolic peak, and (e, f) at the end of the systole (valve closure). The top-left plot on each image is the lateral flow velocity in the center of the lumen. For (e, f) arrows are not shown for a better flow visualization because the vessel is in an active contracting phase, and arrows will overlap with the flow estimates. Carotids were acquired with the brain to the left of the images.

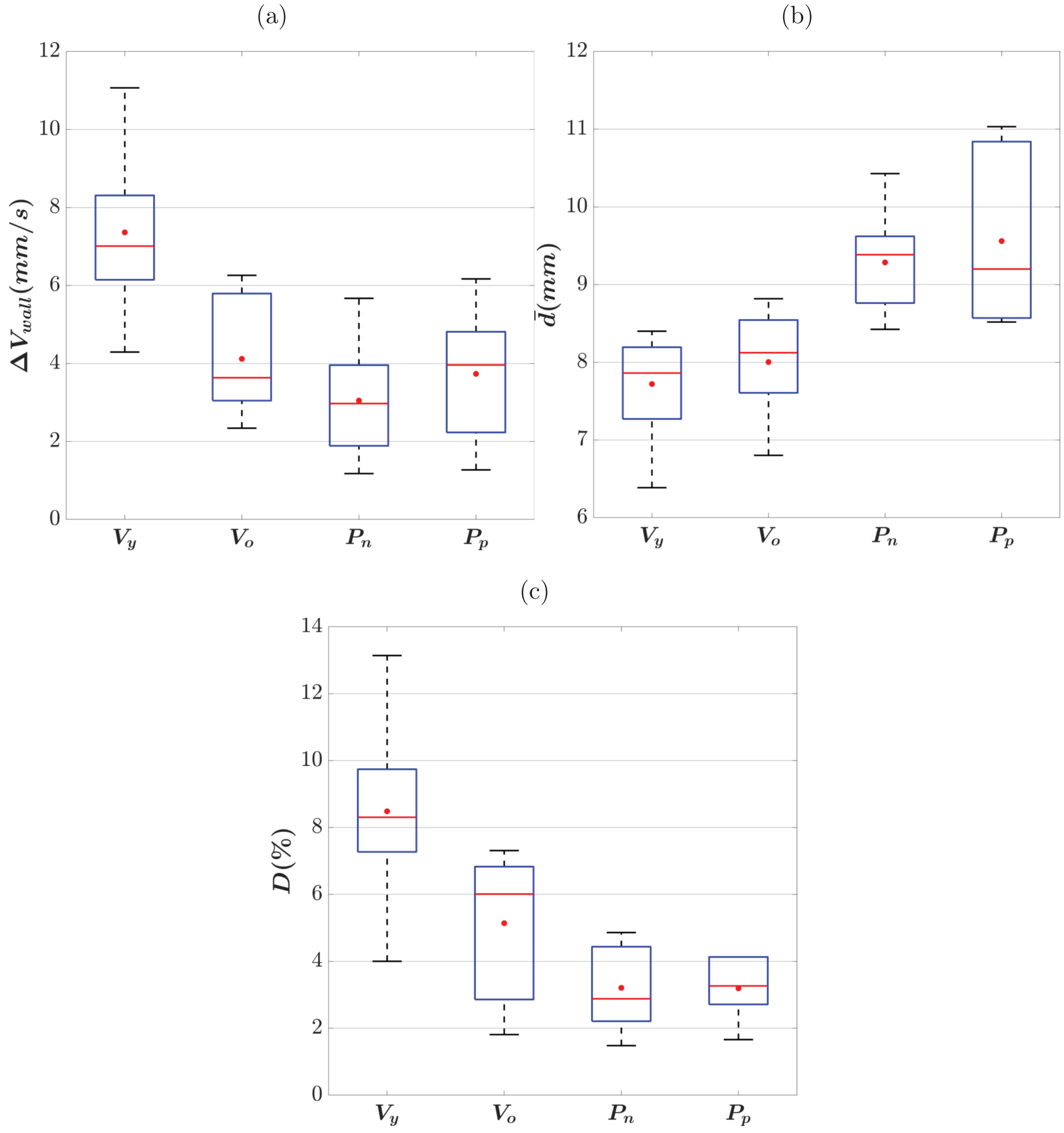

Figure 5.3: (a) Wall velocity range (ΔV_{wall}), diameter of the artery ($\bar{d}$), and (c) distensibility (D) for all the groups of the clinical proof of concept. V and P are for the volunteers and patients, respectively; lower cases Y, O, N, and P are for young, old, non-pathological and pathological subgroups, respectively.

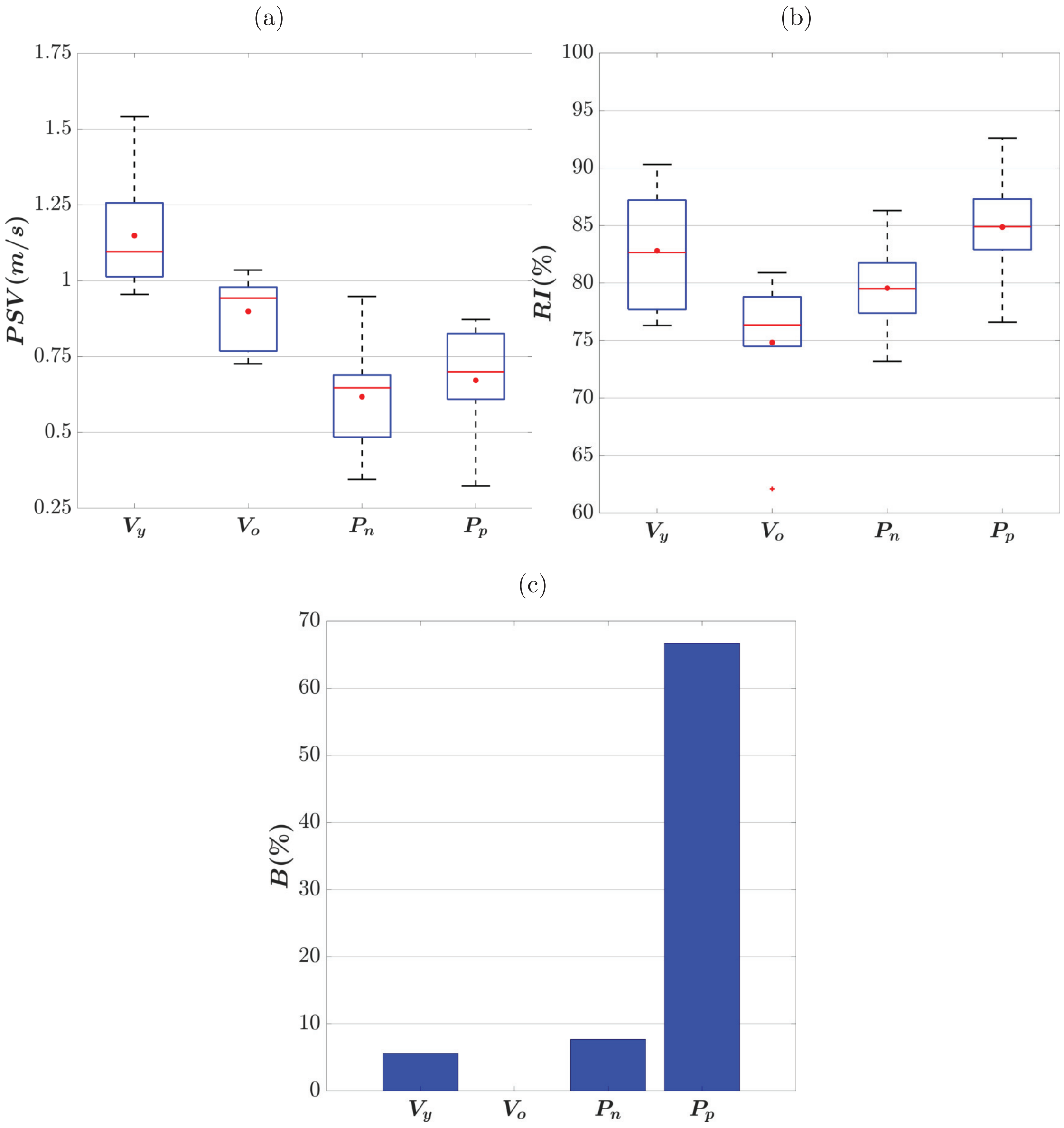

Figure 5.4: (a) Peak systolic velocity (PSV), resistivity index (RI), and (c) backflow (B) for all the groups of the clinical proof of concept. V and P are for the volunteers and patients; lower cases Y, O, N, and P are for young, old, non-pathological and pathological subgroups, respectively.

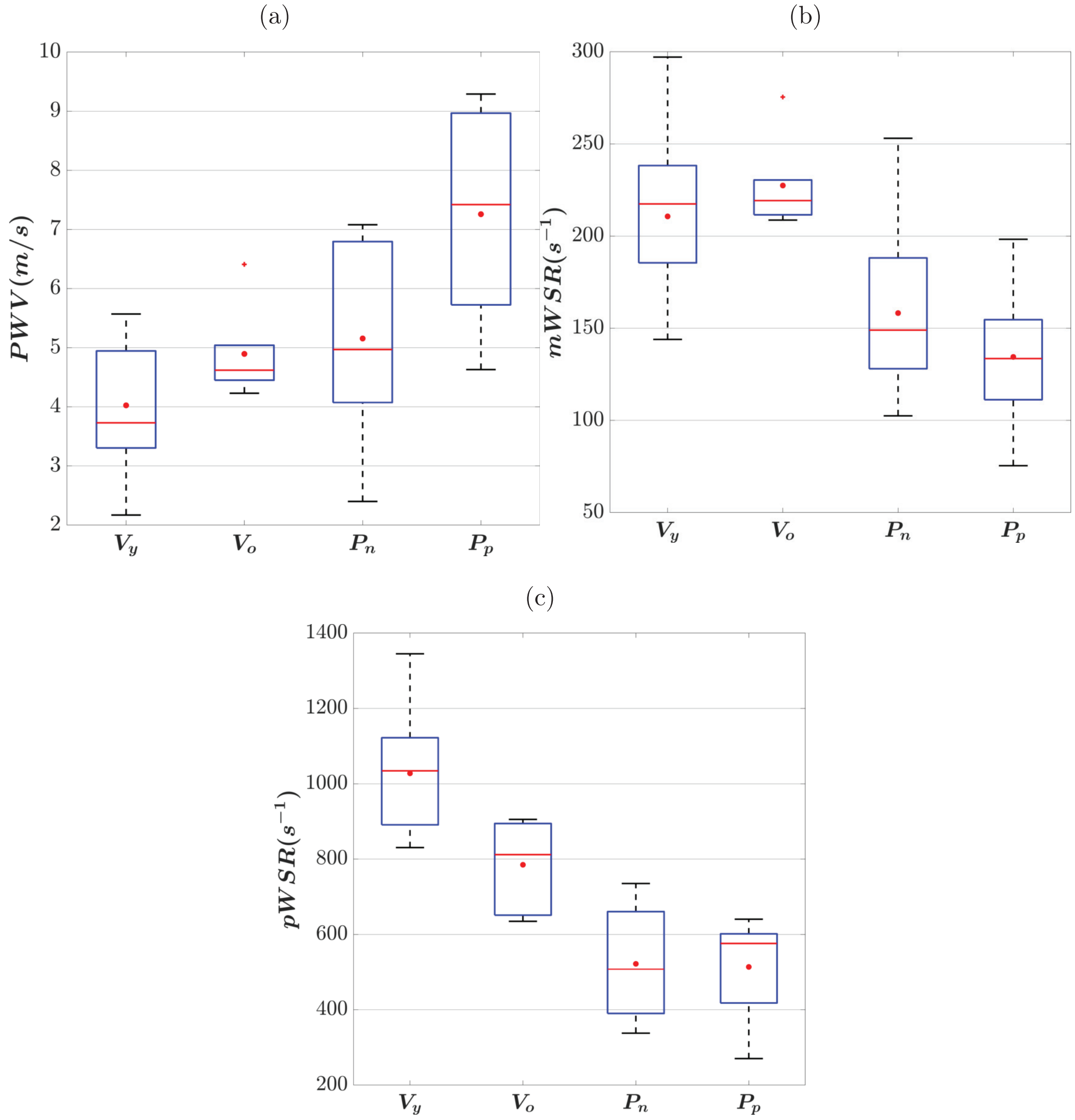

Figure 5.5: (a) Pulse wave velocity (PWV), mean wall shear rate ($mWSR$), and (c) peak wall shear rate ($pWSR$) for all the groups of the clinical proof of concept. V and P are for the volunteers and patients; lower cases Y, O, N, and P are for young, old, non-pathological and pathological subgroups, respectively.

Table 5.3: Measurements for the volunteers of the clinical proof of concept

Metric	Young $\mu \pm \sigma$ $N = 18$	Old $\mu \pm \sigma$ $N = 6$	All $\mu \pm \sigma$ $N = 24$
ΔV_{wall} (mm/s)	7.36 ± 1.89	4.12 ± 1.57	6.55 ± 2.29
$\bar{d}$ (mm)	7.72 ± 0.58	8.00 ± 0.74	7.80 ± 0.62
D (mm)	8.48 ± 2.44	5.14 ± 2.26	7.65 ± 2.77
PSV (m/s)	1.15 ± 0.16	0.90 ± 0.13	1.09 ± 0.19
RI (%)	82.81 ± 4.66	74.83 ± 6.66	80.61 ± 6.18
B (%)	$5.56 \pm N/A$	$0 \pm N/A$	$4.17 \pm N/A$
PWV (m/s)	4.03 ± 0.98	4.90 ± 0.79	4.26 ± 1.00
$mWSR$ (s^{-1})	210.69 ± 39.34	227.45 ± 25.16	214.88 ± 36.56
$pWSR$ (s^{-1})	1027.64 ± 148.69	784.90 ± 121.98	966.95 ± 176.36

than for volunteers; significant differences is found both between young and older volunteers and between volunteers and patients.

Similar observations were found for the peak flow velocity (V_{flow}, Fig. 5.4a); older volunteers have significantly lower velocities than young volunteers, and patients have significantly lower velocities than volunteers. The resistivity index (RI, Fig. 5.4b) seems to decrease with age only; it distinguishes young volunteers from older volunteers. Backflow (B, Fig. 5.4c) is observed primarily in patients with apparent pathology; it is observed in 67 % of those carotids, compared to less than 10 % of all carotids in other groups.

The measured pulse wave velocity (PWV, Fig. 5.5a) seems to increase with the risk of pathology. A value higher than 7 m/s is always corresponding to a patient with pathology; the volunteers can be distinguished from the patients and the older volunteers from the patients with pathology. The mean wall shear rate ($mWSR$, Fig. 5.5b) is lower for the patients than for the volunteers. The peak wall shear rate ($pWSR$, Fig. 5.5c) is also higher for volunteers than for patients, and also higher for young volunteers than older ones.

5.2.3 Internal carotid stenosis

An additional example is included to show the potential, possible extension, and feasibility of this method with more complex geometries and advanced pathologies. Fig. 5.6 shows the internal carotid artery of a patient with severe stenosis; in the stenotic region, the wall moves slower compared to the overall upper

Table 5.4: Measurements for the patients of the clinical proof of concept

Metric	Non-pathological $\mu \pm \sigma$ $N = 13$	Pathological $\mu \pm \sigma$ $N = 6$	All $\mu \pm \sigma$ $N = 19$
ΔV_{wall} (mm/s)	3.05 ± 1.29	3.73 ± 1.79	3.26 ± 1.45
$\bar{d}$ (mm)	9.28 ± 0.62	9.56 ± 1.12	9.38 ± 0.80
D (mm)	3.21 ± 1.22	3.19 ± 0.93	3.20 ± 1.11
PSV (m/s)	0.62 ± 0.16	0.67 ± 0.20	0.63 ± 0.17
RI (%)	79.56 ± 3.76	84.87 ± 5.39	81.24 ± 4.89
B (%)	$7.69 \pm N/A$	$66.67 \pm N/A$	$26.32 \pm N/A$
PWV (m/s)	5.16 ± 1.18	7.26 ± 1.94	6.21 ± 2.11
$mWSR$ (s^{-1})	158.23 ± 42.51	134.44 ± 42.32	150.71 ± 42.79
$pWSR$ (s^{-1})	521.85 ± 137.02	513.65 ± 141.49	519.26 ± 134.5

Table 5.5: P-values between groups and subgroups depending on the metric. V and P are for the volunteers and patients, respectively; lower cases Y, O, N, and P are for young, old, non-pathological and pathological subgroups, respectively.

Metric	V-P	Vy-Vo	Pn-Pp	Vy-Pn	Vy-Pp	Vo-Pn	Vo-Pp
ΔV_{wall}	< 0.001	0.002	0.425	< 0.001	0.002	0.182	0.701
$\bar{d}$	< 0.001	0.417	0.595	< 0.001	0.009	0.005	0.020
D	< 0.001	0.013	0.978	< 0.001	< 0.001	0.094	0.094
PSV	< 0.001	0.002	0.571	< 0.001	< 0.001	< 0.001	0.042
RI	0.803	0.031	0.064	0.041	0.427	0.152	0.017
B	0.046	0.331	0.037	0.824	0.033	0.337	0.025
PWV	0.018	0.055	0.119	0.254	0.018	0.782	0.050
$mWSR$	< 0.001	0.246	0.282	0.002	0.005	< 0.001	0.002
$pWSR$	< 0.001	0.002	0.908	< 0.001	< 0.001	0.001	0.005

Metric	V-Pn	V-Pp	P-Vy	P-Vo
ΔV_{wall}	< 0.001	0.009	< 0.001	0.272
$\bar{d}$	< 0.001	0.011	< 0.001	0.004
D	< 0.001	< 0.001	< 0.001	0.091
PSV	< 0.001	0.002	< 0.001	0.002
RI	0.450	0.146	0.325	0.067
B	0.691	0.031	0.089	0.021
PWV	0.352	0.024	0.010	0.101
$mWSR$	< 0.001	0.004	< 0.001	< 0.001
$pWSR$	< 0.001	< 0.001	< 0.001	< 0.001

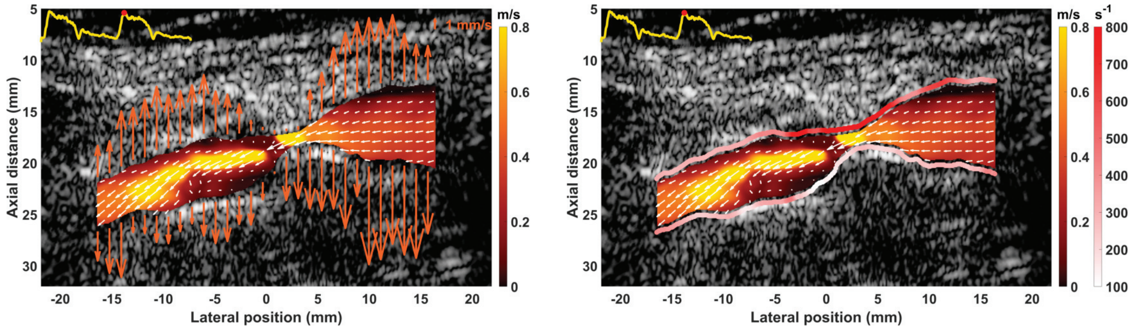
(a) (b)

Figure 5.6: (a) Flow and tissue velocity estimates superimposed with B-mode images for the internal carotid artery with stenosis, and in (b) tissue velocity has been replaced with the local peak wall shear rate.

wall (Fig. 5.6a). Moreover, the pWSR is higher at this position. Before the stenosis, the flow is parabolic, whereas after the stenosis a jetstream can be visualized with potential out-of-plane flow surrounding the central jet (Fig. 5.6b).

5.3 Limitations and opportunities

The feasibility of simultaneous measurement of the vessel wall and blood flow velocities was investigated in a relevant clinical context at a high frame rate. Indeed, flow and wall motion were extracted for all the volunteers. For the patients, if we do not take into account the ones presenting too much out-of-plane motion in the data (which could probably be corrected at the scanning stage and is not linked to the method itself), the feasibility is around 90 %, which is high; the remaining 10 % percent is due to strong clutter in the flow or out-of-plane acquisitions. The flow estimation process is not able to handle data with clutter too intense compared to the flow signal. Further, the feasibility of using these estimates to derive markers such as pulse wave velocity and wall shear rate was investigated, and groups were compared based on statistical tests.

The visualization of flow and tissue motion showed similar results for all volunteers, yielding a parabolic flow profile and uniform motion in the wall. In patients, the resulting images showed complex flow patterns, vortices, and low-velocity regions close to the wall. The vectors allow analyzing more precisely flow patterns compared to conventional color Doppler imaging where only one component of the velocity can be extracted. The technique could also be used for the detection of unusual wall motion. Indeed in the cases discussed in this work, the method was able to highlight motionless parts of the arterial wall. Using the measured parameters, it was possible to distinguish volunteers according to their age and from patients, and patients with an apparent pathology from the others.

Several aspects can be criticized; first, because of the small number of patients, this work must be regarded as clinical proof of concept and not a clinical study. Second, the grouping of the patients was based on the observations of the cardiologist during conventional screening. However, that does not exclude pathology in the arterial system or hyper/hypotension. This aspect could explain the difficulty in separating the two subgroups of patients and the variability in measurements for the two subgroups; some missing histories could also lead to a bias for the patients. Third, out-of-plane motions may affect the estimates, and aligning the probe position to the carotid geometry is challenging, especially in the patient population. A solution should be to use a 3D imaging technique for both tissue and flow motion estimations. Unfortunately, the current technology does not permit to reach a sufficiently high frame rate using a 3D imaging technique to assess the carotid properties investigated in this study. Finally, the WSR was measured in this study, and not the wall shear stress (WSS). Although the stress due to the passing blood flow would be better represented by the WSS, this value is dependent on the value of the blood viscosity, which can change locally in the arterial system.

Overall, this study has shown the feasibility of the investigated methods in a clinical context using a research scanner. Velocity derived measurements could successfully be extracted both in healthy volunteers and a relevant patient population, including complex geometries with stenoses and remodeling. Future work should include more carotids with different geometries to precisely evaluate the potential clinical benefits. Indeed the next stage is to evaluate, with a longitudinal study, if combining flow and wall motion estimates will lead to better detection of high-risk profiles, early detection of plaques, and assist the clinician in the vulnerability assessment of the plaque to decide if a surgical treatment if appropriate. Depending on the benefits, closer collaborations with clinicians must be established to evaluate the feasibility of a potential application of this technique in clinical routine.

Conclusions, Challenges, and Perspectives for Routine Clinical Use

The heart and the arteries are a complex system that can be subject to pathologies such as an aneurysm or a plaque; being able to detect and assess the severity of those pathologies is a crucial medical need. Indeed, they can strongly affect the patient's health and cause death in critical cases. The earlier the detection, the better the patient can be treated, and the less the consequences will be. If the disease is declared and visible, it is important to know if a clinical intervention should be performed, then quantification is necessary. For cardiovascular imaging, ultrasound is frequently used and permits to visualize the organs, and extract both qualitative and quantitative information. Pathological markers can be extracted based on the aspect of the images and velocity estimates. Often, Doppler techniques are used in clinics to access the velocity of the tissue and/or flow. However, other approaches have been proposed and used, such as speckle tracking or optical flow. Since pathological markers can be extracted from both tissue and flow, being able to simultaneously extract both flow and tissue velocity in a clinical environment seemed highly relevant. Moreover, a good temporal resolution is also needed to access advanced parameters such as pulse wave velocity and capture fast and complex phenomena that can occur in arteries. In this thesis, I have decided to bring a solution to this problem by developing and validating, in a clinical environment, a technique able to provide high frame rate ultrasound imaging with both vectorial flow and wall motion estimates.

This thesis is broken down into five chapters. First, the medical context has been described and showed the interest and need to have a technique able to simultaneous detect both flow and wall motion at a high frame rate. Secondly, an overview of different motion estimation techniques was carried out. Even if in the literature, no method was developed for simultaneous flow and wall motion estimation in a clinical environment, transverse oscillation has been developed for flow imaging then adapted for tissue motion estimation. Therefore, this technique was chosen as a foundation for the development of the technique. Then, transverse oscillation has been fully described in chapter 3, and a Fourier based approach, permitting to introduce transverse oscillation at an inexpensive cost, has been described. A 2D phase-based estimator dedicated to transverse oscillation has been described and validated *in vitro* for both vectorial flow and wall motion estimation. To make further progress towards the clinic, adaptive approaches have been developed for clutter filtering based on the tissue estimates that the technique can extract at high frame rates. Finally, clinical proof of concept was conducted in St. Olavs hospital (Trondheim, Norway) with both volunteers and patients on carotids.

To achieve the goal of the thesis, validation of the technique was developed on an *in vitro* and in-house phantom developed for the project. During validation, estimates were accurate and coherent with low standard deviations and error for both flow and tissue motion estimated. After validating the technique, the adaptive approaches for clutter filtering showed on *in vivo* carotid encouraging results showing the interest of having tissue information in addition to the flow. Indeed, those adaptive approaches were compared against standard techniques and showed better flow estimated especially close to the wall and during diastole. The clinical proof of concept was also conclusive with the feasibility of 90 %, mainly due to strong clutter and out-of-plane acquisition. Most of the patients have a more complex flow and wall motion pattern than volunteers. Also, patients showed significant differences compared to the volunteers for several pathological markers. Given those results and developments, the ultrasound imaging is now fully developed and validated for extensive use in a clinical environment.

Like any research work, this thesis has certain limitations and points that could be further developed. First, during this work, only the transverse oscillation technique was used, and no comparison with other estimation techniques was performed. The choice of the transverse oscillation technique was guided by the laboratory's past work and the fact that the method had already been validated for tissue and flow. Moreover, it seemed a relatively inexpensive and straightforward approach compared to others. However, it does not mean that other methods could not have similar or even better results. Validation was performed on two different phantoms for wall and flow estimation without the use of simulation before. This is a modeling problem, flow-wall interactions are complex, and no available methods seemed to be available. Concerning the phantoms, no device on the market met our expectations to validate both aspects, so two phantoms were used for each feature. During the *in vivo* acquisitions, for the development of the clutter filtering and the clinical proof of concept, the number of volunteers and patients was relatively low, which makes it difficult to extract strong statistical values with good confidence. It is a time issue, it is difficult to get, especially in a clinical environment, as many volunteers/patients as desired before the end of the thesis. Another limitation is the inconsistency in the placement or misplacement of the probe during acquisitions at this hospital; this is still an issue even for a trained practitioner or cardiologist. At the moment, there is no proper solution to this issue, especially since patients may have difficulty remaining still during acquisitions.

Perspectives include a more extensive study that can fully qualify as a clinical study. Coupled with statistical tests, it will make it possible to accurately measure the interest and contribution of the method for the detection of pathologies. Also, the modification of the method to another geometry is an important future work. If used with abdominal probes, it will be possible to use the technique in the aorta for a potential application on aneurysms, which mainly occur in that artery. Regarding applications to new probe geometry, the use of a matrix probe for 3D ultrasound imaging will permit to get rid of placement issues and out-of-plane motion. However, the size of the elements makes it difficult to get a good signal-to-noise ratio and the high number of elements gives a high computation cost for signal and image processing. For image quality, because of the use of plane waves, it remains quite low compared to focused ultrasound modes that are available on medical scanners. A possible solution is to work on beamforming algorithms to get a better image quality with plane wave without sacrificing the frame rate; a good initiative was the PICMUS challenge [155] where the ultrasound community was able to compare their different beamforming methods. A second idea is to use more a complex transmit signal that can, after post-processing, yield higher contrast and resolution; such methods include for instance the use in transmission of chirp signals [156], [157] having a high autocorrelation, or Golay codes [158] which are orthogonal. Deep learning is also a key for better image quality and can be used to increase image quality at a very low-cost [159]. Nevertheless, all those advances approaches are not well studied in the literature with Doppler estimations, since they can modify the signal properties itself and create speckle decorrelation. All those perspectives, including new geometry, probe technologies, advanced signal processing techniques, and deep learning leads us to believe that there is still room for improvement to extend the method more widely to other organs and make it more attractive in clinics.

Personal Contribution

Published articles

- **V. Perrot**, S. Salles, D. Vray, and H. Liebgott, “Video magnification applied in ultrasound,” *IEEE Transactions on Biomedical Engineering*, vol. 66, no. 1, pp. 283–288, Jan. 2019.
- **V. Perrot**, S. Meier, A. Bel-Brunon, H. W.-L. Berre, B. Bou-Saïd, P. Chaudet, V. Detti, D. Vray, and H. Liebgott, “Biofidelic abdominal aorta phantom: Cross-over preliminary study using UltraSound and Digital Image Stereo-Correlation,” *IRBM*, vol. 38, no. 4, pp. 238–244, Aug. 2017.

Submitted article

- **V. Perrot**, I. K. Ekroll, J. Avdal, L. M. Saxhaug, H. Dalen, D. Vray, L. Løvstakken, and H. Liebgott, “Simultaneous vectorial blood flow and wall motion imaging in the carotid artery: A clinical proof of concept,” *IEEE Transactions on Ultrasonics, Ferroelectrics, and Frequency Control*, 2019.

International oral presentations with proceedings

- **V. Perrot** and D. Garcia, “Back to basics in ultrasound velocimetry: Tracking speckles by using a standard PIV algorithm,” in *2018 IEEE International Ultrasonics Symposium (IUS)*, IEEE, Oct. 2018.
- M. Polichetti, **V. Perrot**, H. Liebgott, B. Nicolas, and F. Varray, “Influence of beamforming methods on velocity estimation: In vitro experiments,” in *2018 IEEE International Ultrasonics Symposium (IUS)*, IEEE, Oct. 2018.
- S. Salles, A. Long, L. Petrusca, **V. Perrot**, D. Vray, and H. Liebgott, “Estimation of arterial wall motion using ultrafast imaging and transverse oscillations: In vivo study,” in *2016 IEEE International Ultrasonics Symposium (IUS)*, IEEE, Sep. 2016.

International poster presentations with proceedings

- **V. Perrot**, J. Avdal, H. Liebgott, and I. K. Ekroll, "Comparison of adaptive clutter filters for vector velocity estimation: Realistic simulations and in vivo examples," in *2019 IEEE International Ultrasonics Symposium (IUS)*, IEEE, Oct. 2019.
- N. Ghigo, **V. Perrot**, B. Harbaoui, A. Long, S. Ricci, P. Tortoli, D. Vray, and H. Liebgott, "High frame rate vector flow imaging with a convex array in a simulated vessel phantom," in *2019 IEEE International Ultrasonics Symposium (IUS)*, IEEE, Oct. 2019.
- Y. M. Benane, **V. Perrot**, L. Petrusca, and O. Basset, "3D fast ultrasound imaging through pulse compression: An experimental study," in *2019 IEEE International Ultrasonics Symposium (IUS)*, IEEE, Oct. 2019.
- **V. Perrot**, H. Liebgott, A. Long, and D. Vray, "Simultaneous tissue and flow estimation at high frame rate using plane wave and transverse oscillation on in vivo carotid," in *2018 IEEE International Ultrasonics Symposium (IUS)*, IEEE, Oct. 2018.
- **V. Perrot**, J. Avdal, L. Løvstakken, S. Salles, D. Vray, H. Liebgott, and I. K. Ekroll, "Spatial and temporal adaptive FIR clutter filtering," in *2018 IEEE International Ultrasonics Symposium (IUS)*, IEEE, Oct. 2018.
- **V. Perrot**, L. Petrusca, A. Bernard, D. Vray, and H. Liebgott, "Simultaneous pulse wave and flow estimation at high-framerate using plane wave and transverse oscillation on carotid phantom," in *2017 IEEE International Ultrasonics Symposium (IUS)*, IEEE, Sep. 2017.

International oral presentations without proceedings

- S. Salles, **V. Perrot**, B. Nicolas, A. Støylen, L. Løvstakken, D. Vray, H. Torp, and H. Liebgott, "Natural mechanical wave detection using ultrafast ultrasound and velocity clutter filter wave imaging," in *2019 hot TOPIcs in IMaging (TOPIM)*, Jan. 2019.
- **V. Perrot**, Y. M. Benane, E. Badescu, H. Liebgott, and D. Garcia, "Dual-frequency alias-free color Doppler using chirping and pulse compression," in *2018 IEEE International Ultrasonics Symposium (IUS)*, Oct. 2018.

International poster presentation without proceedings

- Y. M. Benane, **V. Perrot**, M. Pasovic, and O. Basset, “Ultrafast second harmonic inversion for ultrasound contrast harmonic imaging,” in *2019 IEEE International Ultrasonics Symposium (IUS)*, Oct. 2019.

International invited talk without proceeding

- H. Liebgott, **V. Perrot**, N. Ghigo, S. Salles, I. K. Ekroll, A. Ramalli, J. Avdal, E. Boni, F. Varray, L. Petrusca, A. Bernard, A. Long, B. Harbaoui, P. Tortoli, L. Løvstakken, and D. Vray, “High frame rate ultrasound imaging of the arteries,” in *2019 International Congress on Ultrasonics (ICU)*, Sep. 2019.

National oral presentations without proceedings

- **V. Perrot**, N. Ghigo, L. Petrusca, A. Bernard, S. Salles, A. Long, B. Harbaoui, F. Varray, D. Vray, and H. Liebgott, “Imagerie ultrasonore ultra-rapide de l’artère carotide,” in *2019 Recherche en Imagerie et Technologies pour la Santé (RITS)*, Oct. 2019.
- **V. Perrot**, S. Meier, A. Bel-Brunon, H. W.-L. Berre, B. Bousaïd, P. Chaudet, V. Detti, D. Vray, and H. Liebgott, “Montage expérimental biofidèle d’aorte abdominale,” in *2017 Recherche en Imagerie et Technologies pour la Santé (RITS)*, Oct. 2017.

Bibliography

[1] K. A. Young, J. A. Wise, P. DeSaix, D. H. Kruse, B. Poe, E. Johnson, J. E. Johnson, O. Korol, J. G. Betts, and M. Womble, *Anatomy & physiology*. OpenStax College, 2013.

[2] J. E. Hall, *Guyton and hall textbook of medical physiology, 12e*. Saunders, 2010.

[3] P. Reymond, F. Merenda, F. Perren, D. Rüfenacht, and N. Stergiopulos, "Validation of a one-dimensional model of the systemic arterial tree," *American Journal of Physiology-Heart and Circulatory Physiology*, vol. 297, no. 1, H208–H222, Jul. 2009.

[4] T. C. Gasser, R. W. Ogden, and G. A. Holzapfel, "Hyperelastic modelling of arterial layers with distributed collagen fibre orientations," *Journal of The Royal Society Interface*, vol. 3, no. 6, pp. 15–35, Feb. 2006.

[5] W. Nichols, M. O'Rourke, and C. Vlachopoulos, "The nature of flow of a liquid," in *McDonald's Blood Flow in Arteries 6th Edition: Theoretical, Experimental and Clinical Principles*, R. Reneman, Ed., CRC Press, Jul. 2011, pp. 13–54.

[6] W. Nichols, M. O'Rourke, and C. Vlachopoulos, "Atherosclerosis," in *McDonald's Blood Flow in Arteries 6th Edition: Theoretical, Experimental and Clinical Principles*, R. Reneman, Ed., CRC Press, Jul. 2011, pp. 499–506.

[7] Y. M. Hong, "Atherosclerotic cardiovascular disease beginning in childhood," *Korean Circulation Journal*, vol. 40, no. 1, p. 1, 2010.

[8] S. C. Cramer, G. Nelles, R. R. Benson, J. D. Kaplan, R. A. Parker, K. K. Kwong, D. N. Kennedy, S. P. Finklestein, and B. R. Rosen, "A functional MRI study of subjects recovered from hemiparetic stroke," *Stroke*, vol. 28, no. 12, pp. 2518–2527, Dec. 1997.

[9] T. Ingall, "Stroke-incidence, mortality, morbidity and risk," *Journal of insurance medicine-New York then Denver*, vol. 36, pp. 143–152, 2004.

[10] Intercollegiate Stroke Working Party, "Acute phase care," in *National clinical guideline for stroke*, Citeseer, 2012, pp. 37–60.

[11] S. J. Lewis, "Prevention and treatment of atherosclerosis: A practitioner's guide for 2008," *The American Journal of Medicine*, vol. 122, no. 1, S38–S50, Jan. 2009.

[12] S. Satomura, “Ultrasonic Doppler method for the inspection of cardiac functions,” *The Journal of the Acoustical Society of America*, vol. 29, no. 11, pp. 1181–1185, Nov. 1957.

[13] B. Sigel, “A brief history of Doppler ultrasound in the diagnosis of peripheral vascular disease,” *Ultrasound in Medicine & Biology*, vol. 24, no. 2, pp. 169–176, Feb. 1998.

[14] J. A. Jensen, “A model for the propagation and scattering of ultrasound in tissue,” *The Journal of the Acoustical Society of America*, vol. 89, no. 1, pp. 182–190, Jan. 1991.

[15] P. M. Morse, K. U. Ingard, and R. T. Beyer, “Theoretical acoustics,” *Journal of Applied Mechanics*, vol. 36, no. 2, p. 382, 1969.

[16] B. Angelsen, “Principles of medical ultrasound imaging and measurements,” in *Ultrasound Imaging: Waves, Signals, and Signal Processing*, vol. 1, Emantec, 2001, pp. 3–100.

[17] F. A. Duck, “Acoustic properties of tissue at ultrasonic frequencies,” in *Physical Properties of Tissues*, Elsevier, 1990, pp. 73–135.

[18] F. A. Duck, “The propagation of ultrasound through tissue,” in *The safe use of ultrasound in medical diagnosis*, The British Institute of Radiology, 2001, pp. 4–17.

[19] J. Jensen, M. B. Stuart, and J. A. Jensen, “Optimized plane wave imaging for fast and high-quality ultrasound imaging,” *IEEE Transactions on Ultrasonics, Ferroelectrics, and Frequency Control*, vol. 63, no. 11, pp. 1922–1934, Nov. 2016.

[20] T. L. Szabo, “Imaging systems and applications,” in *Diagnostic Ultrasound Imaging: Inside Out (Biomedical Engineering)*, Academic Press, 2013, pp. 365–430.

[21] J. A. Jensen, “Field: A program for simulating ultrasound systems,” *Medical and Biological Engineering and Computing*, vol. 34, pp. 351–352, Jan. 1996.

[22] J. Jensen and N. Svendsen, “Calculation of pressure fields from arbitrarily shaped, apodized, and excited ultrasound transducers,” *IEEE Transactions on Ultrasonics, Ferroelectrics and Frequency Control*, vol. 39, no. 2, pp. 262–267, Mar. 1992.

[23] M. Tanter, J. Bercoff, L. Sandrin, and M. Fink, “Ultrafast compound imaging for 2-D motion vector estimation: Application to transient elastography,” *IEEE Transactions on Ultrasonics, Ferroelectrics and Frequency Control*, vol. 49, no. 10, pp. 1363–1374, Oct. 2002.

[24] J. Udesen, F. Gran, K. Hansen, J. A. Jensen, C. Thomsen, and M. Nielsen, “High frame-rate blood vector velocity imaging using plane waves: Simulations and preliminary experiments,” *IEEE Transactions on Ultrasonics, Ferroelectrics and Frequency Control*, vol. 55, no. 8, pp. 1729–1743, Aug. 2008.

[25] G. Montaldo, M. Tanter, J. Bercoff, N. Benech, and M. Fink, “Coherent plane-wave compounding for very high frame rate ultrasonography and transient elastography,” *IEEE Transactions on Ultrasonics, Ferroelectrics and Frequency Control*, vol. 56, no. 3, pp. 489–506, 2009.

[26] M. Tanter and M. Fink, "Ultrafast imaging in biomedical ultrasound," *IEEE Transactions on Ultrasonics, Ferroelectrics and Frequency Control*, vol. 61, no. 1, pp. 102–119, 2014.

[27] J. A. Jensen, S. I. Nikolov, K. L. Gammelmark, and M. H. Pedersen, "Synthetic aperture ultrasound imaging," *Ultrasonics*, vol. 44, e5–e15, Dec. 2006.

[28] H. Takahashi, H. Hasegawa, and H. Kanai, "Echo speckle imaging of blood particles with high-frame-rate echocardiography," *Japanese Journal of Applied Physics*, vol. 53, no. 7S, 07KF08, Jun. 2014.

[29] L. Tong, A. Ramalli, R. Jasaityte, P. Tortoli, and J. D'hooge, "Multi-transmit beam forming for fast cardiac imaging—experimental validation and in vivo application," *IEEE Transactions on Medical Imaging*, vol. 33, no. 6, pp. 1205–1219, Jun. 2014.

[30] D. H. Johnson and D. E. Dudgeon, "Beamforming," in *Array signal processing: Concepts and techniques*, Prentice Hall, 1993, pp. 111–198.

[31] W. Nichols, M. O'Rourke, and C. Vlachopoulos, "Ultrasound: Applications," in *McDonald's Blood Flow in Arteries 6th Edition: Theoretical, Experimental and Clinical Principles*, R. Reneman, Ed., CRC Press, Jul. 2011, pp. 189–194.

[32] M. R. Ward, G. Pasterkamp, A. C. Yeung, and C. Borst, "Arterial remodeling," *Circulation*, vol. 102, no. 10, pp. 1186–1191, 2000.

[33] G. G. Ferguson, M. Eliasziw, H. W. K. Barr, G. P. Clagett, R. W. Barnes, M. C. Wallace, D. W. Taylor, R. B. Haynes, J. W. Finan, V. C. Hachinski, and H. J. M. Barnett, "The north american symptomatic carotid endarterectomy trial," *Stroke*, vol. 30, no. 9, pp. 1751–1758, 1999.

[34] C. Schmitt, G. Soulez, R. L. Maurice, M.-F. Giroux, and G. Cloutier, "Noninvasive vascular elastography: Toward a complementary characterization tool of atherosclerosis in carotid arteries," *Ultrasound in Medicine & Biology*, vol. 33, no. 12, pp. 1841–1858, Dec. 2007.

[35] A. P. G. Hoeks, P. Brands, F. Smeets, and R. Reneman, "Assessment of the distensibility of superficial arteries," *Ultrasound in Medicine & Biology*, vol. 16, no. 2, pp. 121–128, Jan. 1990.

[36] W. Nichols, M. O'Rourke, and C. Vlachopoulos, "Aging," in *McDonald's Blood Flow in Arteries 6th Edition: Theoretical, Experimental and Clinical Principles*, R. Reneman, Ed., CRC Press, Jul. 2011, pp. 411–446.

[37] O. Frank, "Der puls in den arterien," *Zeitschrift für Biologie*, vol. 45, pp. 441–553, 1905.

[38] W. W. Nichols and D. A. McDonald, "Wave-velocity in the proximal aorta," *Medical & Biological Engineering*, vol. 10, no. 3, pp. 327–335, May 1972.

[39] M. Benthin, P. Dahl, R. Ruzicka, and K. Lindström, "Calculation of pulse-wave velocity using cross correlation: Effects of reflexes in the arterial tree," *Ultrasound in Medicine & Biology*, vol. 17, no. 5, pp. 461–469, Jan. 1991.

[40] J. Luo, R. X. Li, and E. E. Konofagou, “Pulse wave imaging of the human carotid artery: An in vivo feasibility study,” *IEEE Transactions on Ultrasonics, Ferroelectrics and Frequency Control*, vol. 59, no. 1, pp. 174–181, Jan. 2012.

[41] A. I. Moens, *Die pulscurve*. Leiden: E.J. Brill, 1878.

[42] D. H. Bergel, “The dynamic elastic properties of the arterial wall,” *The Journal of Physiology*, vol. 156, no. 3, pp. 458–469, May 1961.

[43] K. Fujikura, J. Luo, V. Gamarnik, M. Pernot, R. Fukumoto, M. D. Tilson, and E. E. Konofagou, “A novel noninvasive technique for pulse-wave imaging and characterization of clinically-significant vascular mechanical properties in vivo,” *Ultrasonic Imaging*, vol. 29, no. 3, pp. 137–154, Jul. 2007.

[44] J. Vappou, J. Luo, and E. E. Konofagou, “Pulse wave imaging for noninvasive and quantitative measurement of arterial stiffness in vivo,” *American Journal of Hypertension*, vol. 23, no. 4, pp. 393–398, Apr. 2010.

[45] P. Kruizinga, F. Mastik, S. C. van den Oord, A. F. Schinkel, J. G. Bosch, N. de Jong, G. van Soest, and A. F. van der Steen, “High-definition imaging of carotid artery wall dynamics,” *Ultrasound in Medicine & Biology*, vol. 40, no. 10, pp. 2392–2403, Oct. 2014.

[46] K. J. Taylor, P. N. Burns, and P. Well, *Clinical applications of Doppler ultrasound*. Raven Press, 1988.

[47] W. Nichols, M. O’Rourke, and C. Vlachopoulos, “Contours of pressure and flow waves in arteries: The pulse in disease,” in *McDonald’s Blood Flow in Arteries 6th Edition: Theoretical, Experimental and Clinical Principles*, R. Reneman, Ed., CRC Press, Jul. 2011, pp. 246–248.

[48] J. F. Polak, R. L. Bajakian, D. H. O’Leary, M. R. Anderson, M. C. Donaldson, and F. A. Jolesz, “Detection of internal carotid artery stenosis: Comparison of MR angiography, color Doppler sonography, and arteriography.,” *Radiology*, vol. 182, no. 1, pp. 35–40, Jan. 1992.

[49] G. Maurer, “Aortic regurgitation,” *Heart*, vol. 92, no. 7, pp. 994–1000, May 2006.

[50] M. E. Tublin, R. O. Bude, and J. F. Platt, “The resistive index in renal Doppler sonography: Where do we stand?” *American Journal of Roentgenology*, vol. 180, no. 4, pp. 885–892, Apr. 2003.

[51] W. Nichols, M. O’Rourke, and C. Vlachopoulos, “Contours of pressure and flow waves in arteries: Arterial stenosis,” in *McDonald’s Blood Flow in Arteries 6th Edition: Theoretical, Experimental and Clinical Principles*, R. Reneman, Ed., CRC Press, Jul. 2011, pp. 246–248.

[52] P. J. Brands, A. P. G. Hoeks, L. Hofstra, and R. S. Reneman, “A noninvasive method to estimate wall shear rate using ultrasound,” *Ultrasound in Medicine & Biology*, vol. 21, no. 2, pp. 171–185, Jan. 1995.

[53] D. L. Franklin, W. Schlegel, and R. F. Rushmer, “Blood flow measured by Doppler frequency shift of back-scattered ultrasound,” *Science*, vol. 134, no. 3478, pp. 564–565, Aug. 1961.

[54] W. Wright and R. Meyerdirk, “Electronic doctor being made by longmont engineering firm,” *Daily Times-Call*, 1963.

[55] S. F. Stewart, “Effects of transducer, velocity, Doppler angle, and instrument settings on the accuracy of color Doppler ultrasound,” *Ultrasound in Medicine & Biology*, vol. 27, no. 4, pp. 551–564, Apr. 2001.

[56] K. Fahrbach, *Apparatus for measuring the speed of flowing media*, US 3766517 A, 1973.

[57] P. Hansen, G. Cross, and L. Light, “Beam-angle independent Doppler velocity measurement in superficial vessels,” *Clinical blood flow measurement*, pp. 28–32, Jan. 1974.

[58] S. Uematsu, “Determination of volume of arterial blood flow by an ultrasonic device,” *Journal of Clinical Ultrasound*, vol. 9, no. 5, pp. 209–216, Jun. 1981.

[59] L. Pourcelot, “Real-time blood flow imaging,” in *Echocardiology*, Springer, 1979, pp. 421–428.

[60] W. Clark and H. Hatten, “Noninvasive screening of extracranial carotid disease: Duplex sonography with angiographic correlation.,” *American Journal of Neuroradiology*, vol. 2, no. 5, pp. 443–447, 1981.

[61] ECSTCG, “MRC european carotid surgery trial: Interim results for symptomatic patients with severe (70-99%) or with mild (0-29%) carotid stenosis,” *The Lancet*, vol. 337, no. 8752, pp. 1235–1243, May 1991.

[62] NASCETC, “Beneficial effect of carotid endarterectomy in symptomatic patients with high-grade carotid stenosis,” *New England Journal of Medicine*, vol. 325, no. 7, pp. 445–453, Aug. 1991.

[63] W. S. Moore, H. Barnett, H. G. Beebe, E. F. Bernstein, B. J. Brener, T. Brott, L. R. Caplan, A. Day, J. Goldstone, R. W. Hobson, R. F. Kempczinski, D. B. Matchar, M. R. Mayberg, A. N. Nicolaides, J. W. Norris, J. J. Ricotta, J. T. Robertson, R. B. Rutherford, D. Thomas, J. F. Toole, H. H. Trout, and D. O. Wiebers, “Guidelines for carotid endarterectomy : A multidisciplinary consensus statement from the ad hoc committee, american heart association,” *Circulation*, vol. 91, no. 2, pp. 566–579, Jan. 1995.

[64] J. P. Laissy, A. Cinqualbre, A. Loshkajian, M. C. Henry-Feugeas, B. Crestani, C. Riquelme, and E. Schouman-Claeys, “Assessment of deep venous thrombosis in the lower limbs and pelvis: MR venography versus duplex Doppler sonography.,” *American Journal of Roentgenology*, vol. 167, no. 4, pp. 971–975, Oct. 1996.

[65] J. A. Jensen, “Continuous wave systems,” in *Estimation of blood velocities using ultrasound: A signal processing approach*, Cambridge University Press, 1996, pp. 111–154.

[66] C. Kasai, K. Namekawa, A. Koyano, and R. Omoto, “Real-time two-dimensional blood flow imaging using an autocorrelation technique,” *IEEE Transactions on Sonics and Ultrasonics*, vol. 32, no. 3, pp. 458–464, May 1985.

[67] J. Kirkhorn, “Introduction to IQ-demodulation of RF-data,” *IFBT, NTNU*, vol. 15, 1999.

[68] O. Bonnefous, “Time domain formulation of pulse-Doppler ultrasound and blood velocity estimation by cross correlation,” *Ultrasonic Imaging*, vol. 8, no. 2, pp. 73–85, Apr. 1986.

[69] S. Foster, P. Embree, and W. O’Brien, “Flow velocity profile via time-domain correlation: Error analysis and computer simulation,” *IEEE Transactions on Ultrasonics, Ferroelectrics and Frequency Control*, vol. 37, no. 3, pp. 164–175, May 1990.

[70] T. Loupas, J. Powers, and R. Gill, “An axial velocity estimator for ultrasound blood flow imaging, based on a full evaluation of the Doppler equation by means of a two-dimensional autocorrelation approach,” *IEEE Transactions on Ultrasonics, Ferroelectrics and Frequency Control*, vol. 42, no. 4, pp. 672–688, Jul. 1995.

[71] I. Hein and W. O’Brien, “Current time-domain methods for assessing tissue motion by analysis from reflected ultrasound echoes-a review,” *IEEE Transactions on Ultrasonics, Ferroelectrics and Frequency Control*, vol. 40, no. 2, pp. 84–102, Mar. 1993.

[72] F. Yeung, S. F. Levinson, and K. J. Parker, “Multilevel and motion model-based ultrasonic speckle tracking algorithms,” *Ultrasound in Medicine & Biology*, vol. 24, no. 3, pp. 427–441, Mar. 1998.

[73] C. E. Willert and M. Gharib, “Digital particle image velocimetry,” *Experiments in Fluids*, vol. 10, no. 4, pp. 181–193, Jan. 1991.

[74] G. E. Trahey, J. W. Allison, and O. T. Von Ramm, “Angle independent ultrasonic detection of blood flow,” *IEEE Transactions on Biomedical Engineering*, no. 12, pp. 965–967, 1987.

[75] G. Trahey, S. Hubbard, and O. von Ramm, “Angle independent ultrasonic blood flow detection by frame-to-frame correlation of b-mode images,” *Ultrasonics*, vol. 26, no. 5, pp. 271–276, Sep. 1988.

[76] H. B. Kim, J. R. Hertzberg, and R. Shandas, “Development and validation of echo PIV,” *Experiments in Fluids*, vol. 36, no. 3, pp. 455–462, Mar. 2004.

[77] S. Fadnes, S. A. Nyrnes, H. Torp, and L. Løvstakken, “Shunt flow evaluation in congenital heart disease based on two-dimensional speckle tracking,” *Ultrasound in Medicine & Biology*, vol. 40, no. 10, pp. 2379–2391, Oct. 2014.

[78] G.-R. Hong, G. Pedrizzetti, G. Tonti, P. Li, Z. Wei, J. K. Kim, A. Baweja, S. Liu, N. Chung, H. Houle, J. Narula, and M. A. Vannan, “Characterization and quantification of vortex flow in the human left ventricle by contrast echocardiography using vector particle image velocimetry,” *JACC: Cardiovascular Imaging*, vol. 1, no. 6, pp. 705–717, Nov. 2008.

[79] M. Raffel, C. E. Willert, S. T. Wereley, and J. Kompenhans, “Image evaluation methods for PIV,” in *Experimental Fluid Mechanics*, Springer Berlin Heidelberg, 2007, pp. 123–176.

[80] D. Garcia, P. Lantelme, and E. Saloux, “Introduction to speckle tracking in cardiac ultrasound imaging,” in *Handbook of Speckle Filtering and Tracking in Cardiovascular Ultrasound Imaging and Video*, Institution of Engineering and Technology, 2018, pp. 571–598.

[81] D. Garcia, “Robust smoothing of gridded data in one and higher dimensions with missing values,” *Computational Statistics & Data Analysis*, vol. 54, no. 4, pp. 1167–1178, Apr. 2010.

[82] D. Garcia, “A fast all-in-one method for automated post-processing of PIV data,” *Experiments in Fluids*, vol. 50, no. 5, pp. 1247–1259, Oct. 2010. [Online]. Available: `http://www.biomecardio.com`.

[83] J. A. Jensen, H. Liebgott, F. Cervenansky, and C. A. V. Hoyos, “SA-VFI: The IEEE IUS challenge on synthetic aperture vector flow imaging,” in *2018 IEEE International Ultrasonics Symposium (IUS)*, IEEE, Oct. 2018.

[84] V. Perrot and D. Garcia, “Back to basics in ultrasound velocimetry: Tracking speckles by using a standard PIV algorithm,” in *2018 IEEE International Ultrasonics Symposium (IUS)*, IEEE, Oct. 2018.

[85] J. J. Gibson, *The perception of the visual world*. Houghton Mifflin, 1950.

[86] B. K. Horn and B. G. Schunck, “Determining optical flow,” *Artificial intelligence*, vol. 17, no. 1-3, pp. 185–203, 1981.

[87] B. D. Lucas and T. Kanade, “An iterative image registration technique with an application to stereo vision,” in *Proceedings of the 7th International Joint Conference on Artificial Intelligence - Volume 2*, ser. IJCAI’81, Vancouver, BC, Canada: Morgan Kaufmann Publishers Inc., 1981, pp. 674–679.

[88] G. Mailloux, F. Langlois, P. Simard, and M. Bertrand, “Restoration of the velocity field of the heart from two-dimensional echocardiograms,” *IEEE Transactions on Medical Imaging*, vol. 8, no. 2, pp. 143–153, Jun. 1989.

[89] P. Baraldi, A. Sarti, C. Lamberti, A. Prandini, and F. Sgallari, “Evaluation of differential optical flow techniques on synthesized echo images,” *IEEE Transactions on Biomedical Engineering*, vol. 43, no. 3, pp. 259–272, Mar. 1996.

[90] M. Suhling, M. Arigovindan, C. Jansen, P. Hunziker, and M. Unser, “Myocardial motion analysis from B-mode echocardiograms,” *IEEE Transactions on Image Processing*, vol. 14, no. 4, pp. 525–536, Apr. 2005.

[91] P. Joos, J. Poreé, H. Liebgott, D. Vray, M. Baudet, J. Faurie, F. Tournoux, G. Cloutier, B. Nicolas, and D. Garcia, “High-frame-rate speckle-tracking echocardiography,” *IEEE Transactions on Ultrasonics, Ferroelectrics, and Frequency Control*, vol. 65, no. 5, pp. 720–728, May 2018.

[92] M. Black and A. Jepson, “Estimating optical flow in segmented images using variable-order parametric models with local deformations,” *IEEE Transactions on Pattern Analysis and Machine Intelligence*, vol. 18, no. 10, pp. 972–986, 1996.

[93] X. Pan, K. Liu, J. Shao, J. Gao, L. Huang, J. Bai, and J. Luo, “Performance comparison of rigid and affine models for motion estimation using ultrasound radio-frequency signals,” *IEEE Transactions on Ultrasonics, Ferroelectrics, and Frequency Control*, vol. 62, no. 11, pp. 1928–1943, Nov. 2015.

[94] Z. Liu and J. Luo, “Performance comparison of optical flow and block matching methods in shearing and rotating models,” in *Medical Imaging 2017: Ultrasonic Imaging and Tomography*, N. Duric and B. Heyde, Eds., SPIE, Mar. 2017.

[95] C. Huang, X. Pan, Q. He, M. Huang, L. Huang, X. Zhao, C. Yuan, J. Bai, and J. Luo, "Ultrasound-based carotid elastography for detection of vulnerable atherosclerotic plaques validated by magnetic resonance imaging," *Ultrasound in Medicine & Biology*, vol. 42, no. 2, pp. 365–377, Feb. 2016.

[96] E. G. Grant, C. B. Benson, G. L. Moneta, A. V. Alexandrov, J. D. Baker, E. I. Bluth, B. A. Carroll, M. Eliasziw, J. Gocke, B. S. Hertzberg, S. Katanick, L. Needleman, J. Pellerito, J. F. Polak, K. S. Rholl, D. L. Wooster, and R. E. Zierler, "Carotid artery stenosis: Gray-scale and Doppler US diagnosis–society of radiologists in ultrasound consensus conference," *Radiology*, vol. 229, no. 2, pp. 340–346, Nov. 2003.

[97] C. Wittens, A. Davies, N. Bækgaard, R. Broholm, A. Cavezzi, S. Chastanet, M. de Wolf, C. Eggen, A. Giannoukas, M. Gohel, S. Kakkos, J. Lawson, T. Noppeney, S. Onida, P. Pittaluga, S. Thomis, I. Toonder, M. Vuylsteke, E. G. Committee, P. Kolh, G. de Borst, N. Chakfé, S. Debus, R. Hinchliffe, I. Koncar, J. Lindholt, M. de Ceniga, F. Vermassen, F. Verzini, D. Reviewers, M. D. Maeseneer, L. Blomgren, O. Hartung, E. Kalodiki, E. Korten, M. Lugli, R. Naylor, P. Nicolini, and A. Rosales, "Editor's choice – management of chronic venous disease," *European Journal of Vascular and Endovascular Surgery*, vol. 49, no. 6, pp. 678–737, Jun. 2015.

[98] F. Mehregan, F. Tournoux, S. Muth, P. Pibarot, R. Rieu, G. Cloutier, and D. Garcia, "Doppler vortography: A color Doppler approach to quantification of intraventricular blood flow vortices," *Ultrasound in Medicine & Biology*, vol. 40, no. 1, pp. 210–221, Jan. 2014.

[99] J. Jensen and P. Munk, "A new method for estimation of velocity vectors," *IEEE Transactions on Ultrasonics, Ferroelectrics and Frequency Control*, vol. 45, no. 3, pp. 837–851, May 1998.

[100] P. Haugaard and G. Seerup, *Vector flow ultrasound imaging*, US20130261456A1, 2012.

[101] H. Liebgott, A. Basarab, P. Gueth, D. Friboulet, and P. Delachartre, "Transverse oscillations for tissue motion estimation," *Ultrasonics*, vol. 50, no. 6, pp. 548–555, May 2010.

[102] G. Bambi, T. Morganti, S. Ricci, E. Boni, F. Guidi, C. Palombo, and P. Tortoli, "A novel ultrasound instrument for investigation of arterial mechanics," *Ultrasonics*, vol. 42, no. 1-9, pp. 731–737, Apr. 2004.

[103] P. Tortoli, T. Morganti, G. Bambi, C. Palombo, and K. V. Ramnarine, "Noninvasive simultaneous assessment of wall shear rate and wall distension in carotid arteries," *Ultrasound in Medicine & Biology*, vol. 32, no. 11, pp. 1661–1670, Nov. 2006.

[104] H. Hasegawa and H. Kanai, "Simultaneous imaging of artery-wall strain and blood flow by high frame rate acquisition of RF signals," *IEEE Transactions on Ultrasonics, Ferroelectrics and Frequency Control*, vol. 55, no. 12, pp. 2626–2639, Dec. 2008.

[105] S. Balocco, O. Basset, G. Courbebaisse, E. Boni, A. F. Frangi, P. Tortoli, and C. Cachard, “Estimation of the viscoelastic properties of vessel walls using a computational model and Doppler ultrasound,” *Physics in Medicine and Biology*, vol. 55, no. 12, pp. 3557–3575, May 2010.

[106] Y. Wan, D. Liu, and E. S. Ebbini, “Imaging vascular mechanics using ultrasound: Phantom and in vivo results,” in *2010 IEEE International Symposium on Biomedical Imaging: From Nano to Macro*, IEEE, 2010.

[107] J. Luo and E. E. Konofagou, “Imaging of wall motion coupled with blood flow velocity in the heart and vessels in vivo: A feasibility study,” *Ultrasound in Medicine & Biology*, vol. 37, no. 6, pp. 980–995, Jun. 2011.

[108] I. K. Ekroll, A. Swillens, P. Segers, T. Dahl, H. Torp, and L. Løvstakken, “Simultaneous quantification of flow and tissue velocities based on multi-angle plane wave imaging,” *IEEE Transactions on Ultrasonics, Ferroelectrics and Frequency Control*, vol. 60, no. 4, pp. 727–738, Apr. 2013.

[109] C. Papadacci, V. Finel, O. Villemain, G. Goudot, J. Provost, E. Messas, M. Tanter, and M. Pernot, “4D simultaneous tissue and blood flow Doppler imaging: Revisiting cardiac Doppler index with single heart beat 4D ultrafast echocardiography,” *Physics in Medicine & Biology*, vol. 64, no. 8, p. 085 013, Apr. 2019.

[110] J. A. Jensen, “A new estimator for vector velocity estimation,” *IEEE Transactions on Ultrasonics, Ferroelectrics and Frequency Control*, vol. 48, no. 4, pp. 886–894, Jul. 2001.

[111] M. Anderson, “Multi-dimensional velocity estimation with ultrasound using spatial quadrature,” *IEEE Transactions on Ultrasonics, Ferroelectrics and Frequency Control*, vol. 45, no. 3, pp. 852–861, May 1998.

[112] J. W. Goodman, *Introduction to fourier optics*. New York: McGraw-Hill, Apr. 1968.

[113] P. Tortoli, L. Bassi, E. Boni, A. Dallai, F. Guidi, and S. Ricci, “ULA-OP: An advanced open platform for ultrasound research,” *IEEE Transactions on Ultrasonics, Ferroelectrics and Frequency Control*, vol. 56, no. 10, pp. 2207–2216, Oct. 2009.

[114] E. Boni, L. Bassi, A. Dallai, F. Guidi, V. Meacci, A. Ramalli, S. Ricci, and P. Tortoli, “ULA-OP 256: A 256-channel open scanner for development and real-time implementation of new ultrasound methods,” *IEEE Transactions on Ultrasonics, Ferroelectrics, and Frequency Control*, vol. 63, no. 10, pp. 1488–1495, Oct. 2016.

[115] J. Udesen and J. A. Jensen, “Experimental investigation of transverse flow estimation using transverse oscillation,” in *IEEE Symposium on Ultrasonics, 2003*, IEEE.

[116] J. Udesen and J. A. Jensen, “Investigation of transverse oscillation method,” *IEEE Transactions on Ultrasonics, Ferroelectrics and Frequency Control*, vol. 53, no. 5, pp. 959–971, May 2006.

[117] H. Liebgott, J. Fromageau, J. E. Wilhjelm, D. Vray, and P. Delachartre, "Beamforming scheme for 2D displacement estimation in ultrasound imaging," *EURASIP Journal on Advances in Signal Processing*, vol. 2005, no. 8, May 2005.

[118] H. Liebgott, J. Wilhjelm, J. A. Jensen, D. Vray, and P. Delachartre, "PSF dedicated to estimation of displacement vectors for tissue elasticity imaging with ultrasound," *IEEE Transactions on Ultrasonics, Ferroelectrics and Frequency Control*, vol. 54, no. 4, pp. 746–756, Apr. 2007.

[119] J. Udesen, M. B. Nielsen, K. R. Nielsen, and J. A. Jensen, "Examples of in vivo blood vector velocity estimation," *Ultrasound in Medicine & Biology*, vol. 33, no. 4, pp. 541–548, Apr. 2007.

[120] M. Lenge, A. Ramalli, P. Tortoli, C. Cachard, and H. Liebgott, "Plane-wave transverse oscillation for high-frame-rate 2-D vector flow imaging," *IEEE Transactions on Ultrasonics, Ferroelectrics, and Frequency Control*, vol. 62, no. 12, pp. 2126–2137, Dec. 2015.

[121] F. Varray and H. Liebgott, "An alternative method to classical beamforming for transverse oscillation images: Application to elastography," in *2013 IEEE 10th International Symposium on Biomedical Imaging*, IEEE, Apr. 2013.

[122] G. Zahnd, S. Salles, H. Liebgott, D. Vray, A. Sérusclat, and P. Moulin, "Real-time ultrasound-tagging to track the 2D motion of the common carotid artery wall in vivo," *Medical Physics*, vol. 42, no. 2, pp. 820–830, Jan. 2015.

[123] S. Salles, A. J. Y. Chee, D. Garcia, A. C. H. Yu, D. Vray, and H. Liebgott, "2-D arterial wall motion imaging using ultrafast ultrasound and transverse oscillations," *IEEE Transactions on Ultrasonics, Ferroelectrics, and Frequency Control*, vol. 62, no. 6, pp. 1047–1058, Jun. 2015.

[124] S. Salles, A. Long, L. Petrusca, V. Perrot, D. Vray, and H. Liebgott, "Estimation of arterial wall motion using ultrafast imaging and transverse oscillations: In vivo study," in *2016 IEEE International Ultrasonics Symposium (IUS)*, IEEE, Sep. 2016.

[125] H. Liebgott, "Fourier domain beamforming for transverse-oscillations," in *2010 IEEE International Ultrasonics Symposium*, IEEE, Oct. 2010.

[126] S. Salles, D. Garcia, B. Bou-Saïd, F. Savary, A. Sérusclat, D. Vray, and H. Liebgott, "Plane wave transverse oscillation (PWTO): An ultra-fast transverse oscillation imaging mode performed in the fourier domain for 2d motion estimation of the carotid artery," in *2014 IEEE 11th International Symposium on Biomedical Imaging (ISBI)*, IEEE, Apr. 2014.

[127] J. Jensen, M. B. Stuart, and J. A. Jensen, "High frame rate vector velocity estimation using plane waves and transverse oscillation," in *2015 IEEE International Ultrasonics Symposium (IUS)*, IEEE, Oct. 2015.

[128] C. Sumi, "Fine elasticity imaging utilizing the iterative RF-echo phase matching method," *IEEE Transactions on Ultrasonics, Ferroelectrics and Frequency Control*, vol. 46, no. 1, pp. 158–166, Jan. 1999.

[129] E. Ebbini, "Phase-coupled two-dimensional speckle tracking algorithm," *IEEE Transactions on Ultrasonics, Ferroelectrics and Frequency Control*, vol. 53, no. 5, pp. 972–990, May 2006.

[130] C. Sumi, “Displacement vector measurement using instantaneous ultrasound signal phase-multidimensional autocorrelation and Doppler methods,” *IEEE Transactions on Ultrasonics, Ferroelectrics and Frequency Control*, vol. 55, no. 1, pp. 24–43, Jan. 2008.

[131] A. Basarab, P. Gueth, H. Liebgott, and P. Delachartre, “Phase-based block matching applied to motion estimation with unconventional beamforming strategies,” *IEEE Transactions on Ultrasonics, Ferroelectrics and Frequency Control*, vol. 56, no. 5, pp. 945–957, May 2009.

[132] S. L. Hahn, *Hilbert transforms in signal processing.* Boston (Mass.): Artech house, 1996.

[133] T. Bülow and G. Sommer, “Hypercomplex signals-a novel extension of the analytic signal to the multidimensional case,” *IEEE Transactions on Signal Processing*, vol. 49, no. 11, pp. 2844–2852, 2001.

[134] A. R. Selfridge, G. S. Kino, and B. T. Khuri-Yakub, “A theory for the radiation pattern of a narrow-strip acoustic transducer,” *Applied Physics Letters*, vol. 37, no. 1, pp. 35–36, Jul. 1980.

[135] H. Torp, “Clutter rejection filters in color flow imaging: A theoretical approach,” *IEEE Transactions on Ultrasonics, Ferroelectrics and Frequency Control*, vol. 44, no. 2, pp. 417–424, Mar. 1997.

[136] S. Bjærum, H. Torp, and K. Kristoffersen, “Clutter filter design for ultrasound color flow imaging,” *IEEE Transactions on Ultrasonics, Ferroelectrics and Frequency Control*, vol. 49, no. 2, pp. 204–216, Feb. 2002.

[137] J. Vappou, J. Luo, K. Okajima, M. D. Tullio, and E. E. Konofagou, “Aortic pulse wave velocity measured by pulse wave imaging (PWI): A comparison with applanation tonometry,” *Artery Research*, vol. 5, no. 2, pp. 65–71, Jun. 2011.

[138] K. V. Ramnarine, D. K. Nassiri, P. R. Hoskins, and J. Lubbers, “Validation of a new blood-mimicking fluid for use in Doppler flow test objects,” *Ultrasound in Medicine & Biology*, vol. 24, no. 3, pp. 451–459, Mar. 1998.

[139] J. Fromageau, J.-L. Gennisson, C. Schmitt, R. Maurice, R. Mongrain, and G. Cloutier, “Estimation of polyvinyl alcohol cryogel mechanical properties with four ultrasound elastography methods and comparison with gold standard testings,” *IEEE Transactions on Ultrasonics, Ferroelectrics and Frequency Control*, vol. 54, no. 3, pp. 498–509, Mar. 2007.

[140] J. A. Jensen, “Stationary echo canceling in velocity estimation by time-domain cross-correlation,” *IEEE Transactions on Medical Imaging*, vol. 12, no. 3, pp. 471–477, 1993.

[141] A. P. G. Hoeks, “An efficient algorithm to remove low frequency Doppler signals in digital Doppler systems,” *Ultrasonic Imaging*, vol. 13, no. 2, pp. 135–144, Apr. 1991.

[142] M. Allam, R. Kinnick, and J. Greenleaf, “Isomorphism between pulsed-wave Doppler ultrasound and direction-of-arrival estimation. II. experimental results,” *IEEE Transactions on Ultrasonics, Ferroelectrics and Frequency Control*, vol. 43, no. 5, pp. 923–935, Sep. 1996.

[143] L. A. Ledoux, P. J. Brands, and A. P. G. Hoeks, “Reduction of the clutter component in Doppler ultrasound signals based on singular value decomposition: A simulation study,” *Ultrasonic Imaging*, vol. 19, no. 1, pp. 1–18, Jan. 1997.

[144] A. C. H. Yu and L. Løvstakken, “Eigen-based clutter filter design for ultrasound color flow imaging: A review,” *IEEE Transactions on Ultrasonics, Ferroelectrics and Frequency Control*, vol. 57, no. 5, pp. 1096–1111, May 2010.

[145] L. Løvstakken, S. Bjærum, K. Kristoffersen, R. Haaverstad, and H. Torp, “Real-time adaptive clutter rejection filtering in color flow imaging using power method iterations,” *IEEE Transactions on Ultrasonics, Ferroelectrics and Frequency Control*, vol. 53, no. 9, pp. 1597–1608, Sep. 2006.

[146] K. P. Burnham and D. R. Anderson, “Multimodel inference. understanding AIC and BIC in model selection,” *Sociological Methods & Research*, vol. 33, no. 2, pp. 261–304, Nov. 2004.

[147] C. M. Hurvich and C.-L. Tsai, “Regression and time series model selection in small samples,” *Biometrika*, vol. 76, no. 2, pp. 297–307, 1989.

[148] D. Posada, J. Poreé, A. Pellissier, B. Chayer, F. Tournoux, G. Cloutier, and D. Garcia, “Staggered multiple-PRF ultrafast color Doppler,” *IEEE Transactions on Medical Imaging*, vol. 35, no. 6, pp. 1510–1521, Jun. 2016.

[149] C. Demeé, T. Deffieux, M. Pernot, B.-F. Osmanski, V. Biran, J.-L. Gennisson, L.-A. Sieu, A. Bergel, S. Franqui, J.-M. Correas, I. Cohen, O. Baud, and M. Tanter, “Spatiotemporal clutter filtering of ultrafast ultrasound data highly increases Doppler and fUltrasound sensitivity,” *IEEE Transactions on Medical Imaging*, vol. 34, no. 11, pp. 2271–2285, Nov. 2015.

[150] B. Arnal, J. Baranger, C. Demeé, M. Tanter, and M. Pernot, “In vivo real-time cavitation imaging in moving organs,” *Physics in Medicine and Biology*, vol. 62, no. 3, pp. 843–857, Jan. 2017.

[151] I. K. Ekroll and J. Avdal, “Adaptive clutter filtering based on tissue vector velocities,” in *2017 IEEE International Ultrasonics Symposium (IUS)*, IEEE, Sep. 2017.

[152] W. Nichols, M. O’Rourke, and C. Vlachopoulos, “Properties of the arterial wall: Practice,” in *McDonald’s Blood Flow in Arteries 6th Edition: Theoretical, Experimental and Clinical Principles*, R. Reneman, Ed., CRC Press, Jul. 2011, pp. 13–54.

[153] R. T. Lee, A. J. Grodzinsky, E. H. Frank, R. D. Kamm, and F. J. Schoen, “Structure-dependent dynamic mechanical behavior of fibrous caps from human atherosclerotic plaques.,” *Circulation*, vol. 83, no. 5, pp. 1764–1770, May 1991.

[154] *IEC 60601-2-37:2004 Medical electrical equipment - Part2-37: Particular requirements for the safety of ultrasonic medical diagnostic and monitoring equipment, Edition 1:2001 consolidated with amendment 1:2004. 1.1. International Electrotechnical Commission, 2004.*

[155] H. Liebgott, A. Rodriguez-Molares, F. Cervenansky, J. Jensen, and O. Bernard, “Plane-wave imaging challenge in medical ultrasound,” in *2016 IEEE International Ultrasonics Symposium (IUS)*, IEEE, Sep. 2016.

[156] B. Lashkari, K. Zhang, and A. Mandelis, “High-frame-rate synthetic aperture ultrasound imaging using mismatched coded excitation waveform engineering: A feasibility study,” *IEEE Transactions on Ultrasonics, Ferroelectrics, and Frequency Control*, vol. 63, no. 6, pp. 828–841, Jun. 2016.

[157] Y. M. Benane, D. Bujoreanu, R. J. Lavarello, F. Varray, J.-M. Escoffre, A. Novell, C. Cachard, and O. Basset, “Experimental implementation of a pulse compression technique using coherent plane-wave compounding,” *IEEE Transactions on Ultrasonics, Ferroelectrics, and Frequency Control*, vol. 65, no. 6, pp. 1025–1036, Jun. 2018.

[158] I. Trots, “Mutually orthogonal golay complementary sequences in synthetic aperture imaging systems,” *Archives of Acoustics*, vol. 40, no. 2, pp. 283–289, Jun. 2015.

[159] M. Gasse, F. Millioz, E. Roux, D. Garcia, H. Liebgott, and D. Friboulet, “High-quality plane wave compounding using convolutional neural networks,” *IEEE Transactions on Ultrasonics, Ferroelectrics, and Frequency Control*, vol. 64, no. 10, pp. 1637–1639, Oct. 2017.

[160] R. Maurice, J. Ohayon, Y. Fretigny, M. Bertrand, G. Soulez, and G. Cloutier, “Noninvasive vascular elastography: Theoretical framework,” *IEEE Transactions on Medical Imaging*, vol. 23, no. 2, pp. 164–180, Feb. 2004.

[161] H.-Y. Wu, M. Rubinstein, E. Shih, J. Guttag, F. Durand, and W. Freeman, “Eulerian video magnification for revealing subtle changes in the world,” *ACM Transactions on Graphics*, vol. 31, no. 4, pp. 1–8, Jul. 2012.

[162] M. Rubinstein, N. Wadhwa, F. Durand, W. T. Freeman, and H.-Y. Wu, “Revealing invisible changes in the world,” *Science*, vol. 339, pp. 519–519, Feb. 2013.

[163] M. A. Elgharib, M. Hefeeda, F. Durand, and W. T. Freeman, “Video magnification in presence of large motions,” in *2015 IEEE Conference on Computer Vision and Pattern Recognition (CVPR)*, IEEE, Jun. 2015.

Appendices

A Related Projects

Video magnification applied in ultrasound

Carotid arteries are subject to fast and complex phenomena closely linked with the medium properties (stiffness and geometry) [17], [160]. The pulse wave is one of these phenomena, and its velocity is related to the stiffness of the artery [43]. Different approaches exist to visualize this wave, like vector or color representation superimposed onto B-mode images. However, these methods have several weaknesses. First, they can mask anatomical information. Moreover, motion is converted into a new representation that needs to be explained and interpreted by the examiner. Lastly, if the motion is so small that it cannot be captured with the naked eye (if the medium is imaged at high frame rate), the anatomical images seem motionless while color maps/vectors seem to be animated over an immobile medium; this effect might be confusing and gives the impression that anatomical and motion information are dissociated. To deal with these issues, the video magnification technique is proposed for pulse wave visualization.

Video magnification has been developed for vision applications [161]–[163]. It consists of amplifying estimated motion and recalculate a new set of anatomical images where tissue motion is significantly increased compared to the scale of the image. This method has the privilege to avoid all of the issues outlined above. Carotid arteries from healthy volunteers were imaged with a Verasonics Vantage$^{\text{TM}}$ 256 system (Verasonics, Redmond, Washington, United States) with the L7-4 (ATL Philips, Bothell, Washington, United States) probe. An ultrafast sequence was used based on only one horizontal plane wave transmission. After beamforming, the motion was extracted with a 2D phase-based estimator working on the RF ultrasound data. Displacement was amplified and reapplied in B-mode ultrasound carotid sequences.

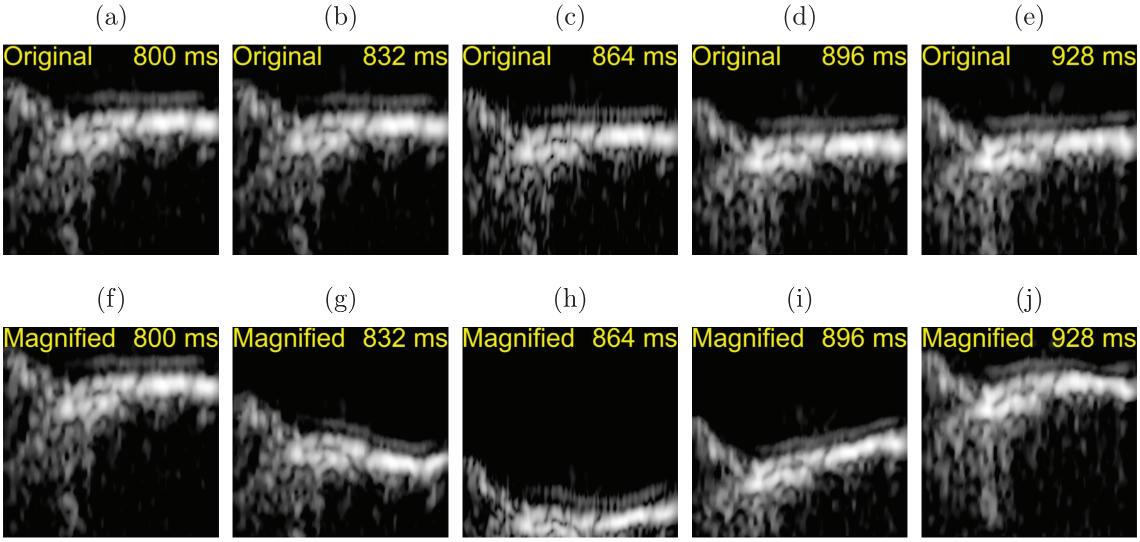

Figure A.1: Video magnification applied for pulse wave visualization: (a-e) pulse wave crossing without video magnification, and (f-j) pulse wave crossing with video magnification; the magnification factor is 750.

Result shows (Fig. A.1) that the pulse wave can be directly visualized in the magnified (Figs. A.1a to A.1e) B-mode images using the video magnification technique while it is almost not visible in the initial B-mode images (Figs. A.1f to A.1j). This method can be used for educational purposes because it makes it possible to understand tissue motion behavior easily. Another promising application is a qualitative inspection for detecting a region having abnormal behaviors due to, for instance, different stiffness linked to tissue necrosis or a plaque. It could serve as a tool for physicians to highlight new pathology indicators or for long-term disease monitoring.

There is one article published in *Transactions on BioMedical Engineering* as evidence of the scientific contribution: "Video magnification applied in ultrasound" (2019).

Alias-free color Doppler using chirping

Color Doppler is one of the most popular non-invasive techniques for blood flow analysis and visualization. Plane wave ultrasound can be used to yield high frame rates and broaden the clinical perspectives of color flow imaging. As with conventional ultrasound, however, aliasing may occur if the flow information is insufficiently time-sampled. The Nyquist velocity limit depends upon PRF (pulse repetition frequency) and center frequency. One approach for extending this Nyquist limit is to transmit signals using a dual-PRF scheme [148] and combine the two aliased estimates to recover alias-free velocities. Instead of transmitting at dual-PRF, it is similarly possible to use a dual-frequency approach to increase Nyquist velocity. The objective was to increase the Nyquist limit while increasing range resolution. Chirp signals and matched filtering were used to obtain a spread spectrum for dual-frequency dealiasing.

A 3 cm rotating disk was scanned with a ULA-OP 256 system (MSDLab, Florence, Italy) [114] with the 9LMQ (Humanscan, Danwon-gu, Ansan-si, Kyunggi-do, South Korea) probe. Rotating velocities from 45 $^\circ/s$ to 720 $^\circ/s$. Linear chirps were transmitted with plane wave transmissions in the 2.7 MHz to 13.4 MHz -20 dB band. The received signals were matched-filtered through pulse compression to recover a wide frequency band. The delayed-and-summed signals were then band-pass filtered at 6.4 MHz and 9.6 MHz, respectively, to provide two signals at different center frequencies. Two series of Doppler velocities were finally obtained by using the complex autocorrelation proposed by Kasai *et al.* [66]. These Doppler velocity fields were combined to extend the Nyquist velocity and return alias-free color Doppler images.

The results show (Fig. A.2) that aliasing was present in the Doppler estimates with a classic 2.5-cycle pulse transmission at the center frequency (Fig. A.2a), and in the two bands of the chirp transmission (Figs. A.2c and A.2d). After the dual-frequency combination, an alias-free velocity map is extracted (Fig. A.2b). These findings demonstrate that the dual-frequency method with pulse compression allows extending the Nyquist velocity limit with a good range resolution. Further improvements are expected with the use of CMUT probes and wider frequency bands.

This project is still ongoing, other experiments were conducted with flow phantoms, *in vivo* carotid, and simulations.

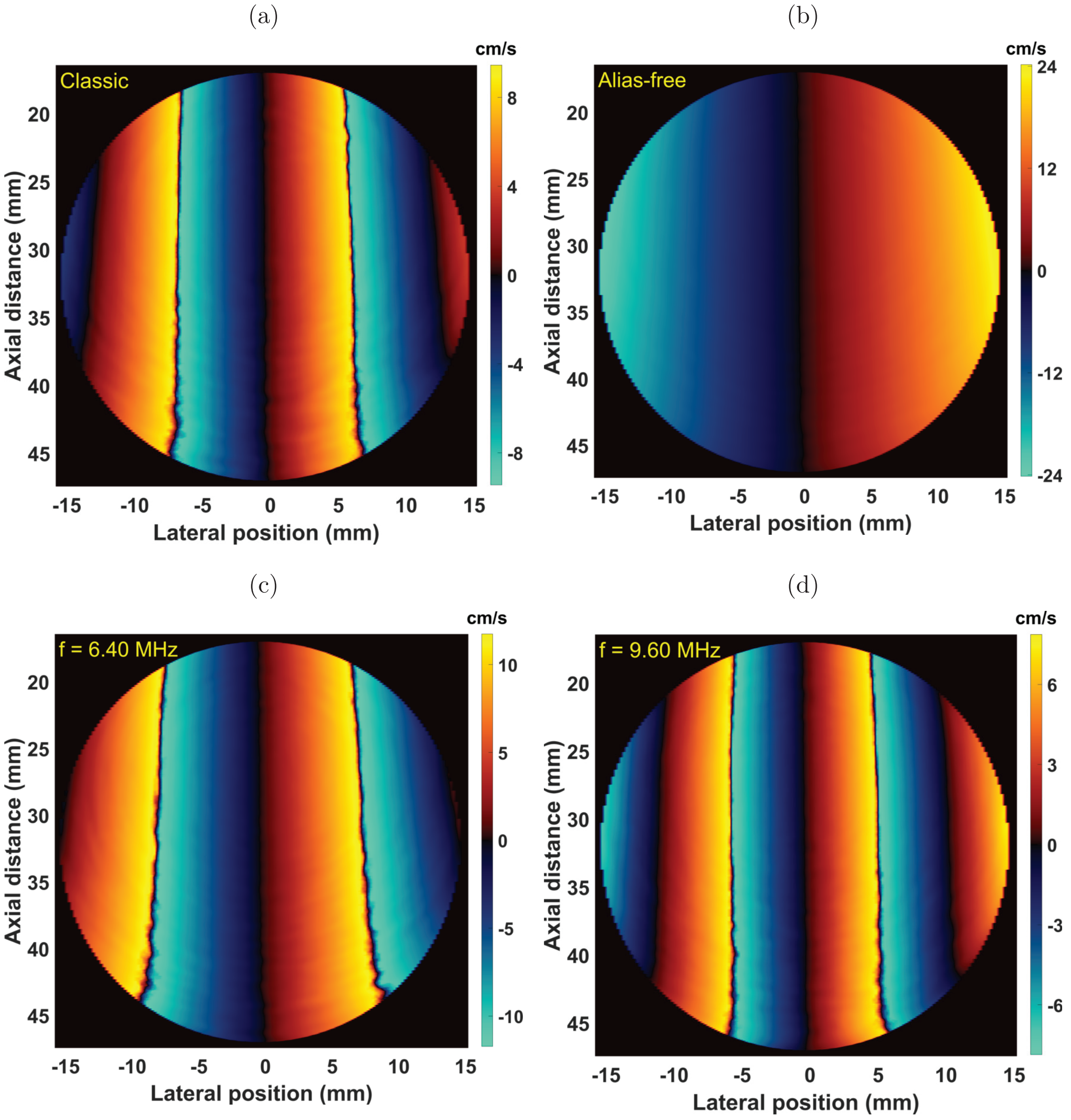

(a) (b) (c) (d)

Figure A.2: Alias-free color Doppler using chirping: (a) color Doppler map with a classic transmission, and (b) alias-free color Doppler map obtained with the two color Doppler maps (c) and (d) at different center frequencies.

B Book Recommendations

During my thesis, several books helped and guided me through three years of research. Here I wanted to pay tribute to these contributions, and I would recommend them to those who, like me a few years ago, could be in great need of them.

For signal processing, great help was the classic “Estimation of blood velocities using ultrasound: A signal processing approach” (1996) by Jørgen Arendt Jensen at Cambridge University Press. This book is cited many times throughout my manuscript, and most of the equations and concepts presented in chapter 2 are described in this book. This reference is extraordinarily complete and describes the classic methods and algorithms in velocity estimation while remaining straightforward in explanations and equations.

Another book for blood velocity estimation is “Ultrasound Imaging: Waves, Signals, and Signal Processing” (2000), volume I (“Basic principles, wave generation, propagation, and beamforming in homogeneous tissue”), and volume II (“Propagation and scattering in heterogeneous, nonlinear tissue with contrast agent imaging and Doppler measurements”) by Bjørn Atle Johan Angelsen at Emantec. This book is less approachable than the first one but explores in detail wave propagation and Doppler principles. I would not recommend this reference to a general audience but to those who are looking for an equation or detailed description of a precise and advanced concept in Doppler imaging.

On the medical side, and more on the cardiovascular aspect, a great reference is “McDonald’s blood flow in arteries 6th edition: Theoretical, experimental and clinical principles” (2011) by Wilmer W. Nichols, Michael F. O’Rourke, and Charalambos Vlachopoulos at CRC Press. The sixth edition of this book, first released in 1960, covers all the medical aspects of the overall arterial system with many supporting references. I would recommend this book to anyone working on the cardiovascular system in general who can extract a great deal of knowledge from it.

C Résumé étendu en français

Introduction

Cette thèse présente un ensemble de travaux qui s'inscrivent en imagerie ultrasonore pour des applications cliniques. L'objectif principal de ce travail intitulé "Imagerie ultrasonore rapide pour l'extraction simultanée du flux et du mouvement pariétal en géométrie linéaire" ("Ultrafast ultrasound imaging for simultaneous extraction of flow and arterial wall motion with linear array probe") est de fournir aux cliniciens un mode d'imagerie ultrasonore pour extraire simultanément la vitesse du flux et le mouvement de la paroi à des cadences d'imagerie élevées dans les artères.

Trois contributions scientiques principales sont présentées dans cette thèse: *i*) la conception de la séquence ultrasonore avec un estimateur de mouvement 2D, *ii*) une nouvelle approche adaptative de filtrage de paroi, et *iii*) une preuve de concept clinique.

Ce manuscript est divisé en cinq chapitres. Le premier chapitre "Contexte général" ("General background") introduit le contexte médical, l'imagerie ultrasonore, les pathologies artérielles et présente les raisons des travaux de thèse. Le second chapitre "Aperçu des techniques d'estimation classiques en échographie vasculaire" ("Overview of standard motion estimation techniques in vascular ultrasound") décrit les méthodes d'estimations Doppler et non Doppler, présente les travaux précédent de la littérature sur la mesure simultanée du mouvement tissulaire et du flux et expose les buts et objectifs de la thèse. Le troisième chapitre "Estimation du flux et du mouvement tissulaire à haute cadence d'imagerie" ("Flow and tissue motion estimation at high frame rates") décrit une méthode d'estimation 2D de mouvement dites par "oscillations transverses", puis la chaîne de traitement est présentée avec les expériences pour les validations *in vitro* avant de conclure sur les limites de la validation *in vitro* et les difficultés *in vivo*. Le quatrième chapitre "Filtrage de paroi adaptatif basé sur les vitesses tissulaires estimées : volontaires *in vivo*" ("Adaptive clutter filtering based on tissue velocity estimates: *in vivo* volunteers") introduit la notion de filtrage de paroi, décrit le filtrage de paroi adaptatif développé, puis présente les expériences *in vivo* pour la validation par comparaison avec les méthodes conventionnelles et l'intérêt de cette approche pour la clinique. Le dernier chapitre "Vers la routine clinique : preuve de concept" ("Toward clinical routine: proof of concept") décrit la méthode et le matériel, présente les résultats d'une étude clinique et conclut sur cette étude avec ses limites et opportunités.

Chapitre 1

Ce premier chapitre décrit : le contexte médical, l'imagerie ultrasonore, les pathologies artérielles et les raisons des travaux de thèse.

Le cœur est l'organe au centre du système cardiovasculaire ; il est responsable d'assurer le pompage et la circulation du sang vers les autres organes. Cette fonction est assurée grâce au système artériel transportant physiquement le sang, le retour étant assuré par le système veineux. Le système artériel est donc primordial, apportant oxygène et nutriments vers les organes et évacuant les déchets de l'organisme. Certaines pathologies peuvent se développer au sein de ce système : plaques d'athérome, anévrismes, ou encore sténoses pour en lister quelques-unes. Malheureusement, les maladies cardiovasculaires restent la première cause de mortalité de par le monde. De plus, elles sont pour la plupart silencieuses et souvent indétectables jusqu'à des stades avancés. Bien que, les causes de la formation de ces maladies sont encore mal connues et mal comprises, la prévention reste l'approche préconisée ; l'autre possibilité étant l'intervention chirurgicale dans les cas très avancés. Donc, il est essentiel de pouvoir détecter ces pathologies le plus tôt possible et quantifier leur niveau de gravité. Une méthode d'imagerie médicale permettant d'étudier et de quantifier les maladies cardiovasculaires est donc cruciale.

L'imagerie ultrasonore se prête particulièrement bien à l'étude du système cardiovasculaire et à la prévention des maladies du fait, entre autres, de sa rapidité d'acquisition, son faible cout et de sa transportabilité. Le système artériel est sujet à des phénomènes physiques complexes et rapides. Par conséquent, pour son étude, une méthode d'imagerie à haute cadence (au-delà de 500 images par seconde) est nécessaire. Une telle méthode d'imagerie ultrasonore, dite par "ondes planes", a été développée dans les années 2000 et permet, en insonifiant l'organe étudié avec un front d'onde ultrasonore plan, d'obtenir des cadences d'imagerie dépassant 10 000 images par seconde dans les vaisseaux superficiels. L'utilisation de l'imagerie ultrasonore par ondes planes est donc tout indiquée pour l'étude du système artériel afin d'avoir une bonne résolution temporelle.

Pour le système artériel, un certain nombres de marqueurs pathologiques ont déjà été développés et sont utilisés en clinique. En ce qui concerne les tissus, le diamètre artériel est par example mesuré lors des examens cliniques. Dans le cas d'une sténose, la mesure de ce paramètre permet d'obtenir le niveau d'occlusion du vaisseau pour caractériser l'avancement de la pathologie. Le flux quant à lui est utilisé pour délimiter précisément les limites et la position des parois artérielles. De plus, la vitesse du sang est utilisée pour caractériser les sténoses ou encore pour détecter d'éventuels reflux. D'autres marqueurs, plus avancés, ont été développés en recherche mais restent peu utilisés dans la pratique clinique. Par exemple, la rigidité artérielle peut être quantifiée via la mesure de la vitesse de l'onde de pouls. Cette onde mécanique se propage au cours des cycles cardiaques le long des parois artérielles et sa vitesse de propagation est liée à l'élasticité du milieu. Elle permet donc de quantifier la rigidité de la paroi qui est souvent considérée comme un des premiers signes du développement de l'athérosclérose. Un autre marqueur, concernant le flux, est la mesure du cisaillement le long de la paroi. Il s'agit d'évaluer les forces de cisaillement appliquées sur la paroi artérielle par le flux ; ces forces pouvant favoriser l'apparition de pathologies ou créer un risque de rupture de plaque d'athérome. Etant donné les différents paramètres et marqueurs pathologiques existants sur le flux et le tissu, une technique permettant l'extraction simultanée des marqueurs de ces deux milieux est pertinente pour la caractérisation des pathologies artérielles.

En conclusion de ce chapitre, les maladies cardiovasculaires sont un fléau mondial. L'imagerie ultrasonore se prête particulièrement bien à l'étude du système cardiovasculaire et permet d'obtenir, via des modes d'imagerie par ondes planes, une haute résolution temporelle. L'utilisation de l'imagerie ultrasonore à haute cadence est donc pertinente pour l'étude du flux et du mouvement tissulaire pour la détection et caractérisation des pathologies artérielles.

Chapitre 2

Ce deuxième chapitre décrit : les méthodes d'estimation Doppler et non Doppler, les travaux précédents de la littérature sur la mesure simultanée du mouvement tissulaire et du flux et les objectifs de la thèse.

Certaines méthodes d'estimation de mouvement peuvent être caractérisées de techniques dites “Doppler”. Ces techniques sont utilisées depuis les années 1970 en clinique pour accéder à la vitesse du flux sanguin. De nombreuses innovations, autant technologiques que méthodologiques, et des accords ont eu lieu jusque dans les années 2000 conduisant à l'utilisation des modes Doppler dans la pratique clinique. Ces modes sont basés sur la mesure de la phase des signaux ultrasonores ou de leurs fréquences. Si un diffuseur se déplace dans la direction de propagation des ultrasons, son déplacement va se traduire par une modification locale de la phase et de la fréquence. Cependant, si le mouvement est perpendiculaire à l'axe de propagation des ultrasons, aucun décalage ne sera mesuré. La vitesse mesurée le long de l'axe ultrasonore est un projeté, sur cet axe, de la vitesse réelle.

D'autres méthodes d'estimation de mouvement existent, parfois inspirées du monde de la vision industrielle, et permettent de trouver un déplacement 2D mais sont quasi inexistantes en clinique ou peu utilisées en pratique. Une méthode classique est l'appariement de blocs et consiste à diviser chaque image ultrasonore en sous-images pour chercher chaque bloc correspondant dans l'image suivante. Ces méthodes sont souvent basées sur l'utilisation de la corrélation pour trouver le bloc correspondant et donc le déplacement. Une autre approche classique est l'utilisation du flux optique, supposant que la luminosité d'un objet est constante au cours du temps et de son déplacement, il est possible d'utiliser cette contrainte pour calculer le déplacer entre deux images ; le problème peut être résolu par méthode différentielle.

Dans la littérature, plusieurs études ont été effectuées sur la mesure du flux vectoriel et du mouvement tissulaire depuis le début des années 2000. Beaucoup d'améliorations et de progrès ont été réalisés, au cours des dernières années, en recherche sans pour autant aller jusqu'à l'application clinique. Malgré l'intérêt clinique, aucune de ces études n'a été en mesure de fournir à la fois de l'information sur l'écoulement vectoriel et sur le mouvement des parois pour extraire des marqueurs pathologiques potentiels dans le système cardiovasculaire à des cadences d'imagerie élevées. Cependant, il y a plusieurs années, une technique capable de produire un flux vectoriel 2D, dites des "oscillations transverses", a été développée. Plus récemment, cette méthode a été étendue à l'estimation du mouvement des tissus mais n'a pas été utilisée pour la mesure simultanée.

En conclusion de ce chapitre, la méthode des oscillations transverses a été développée pour le flux vectoriel et adaptée à l'estimation du mouvement des tissus. Il semble donc approprié d'utiliser cette technique pour la mesure simultanée. Pour atteindre une fréquence d'imagerie élevée, cette méthode est couplée avec l'imagerie ultrasonore par ondes planes pour dépasser un millier d'images par seconde dans les vaisseaux superficiels. Les objectifs de la thèse sont de : concevoir la séquence ultrasonore ultra-rapide, mettre en oeuvre la chaîne de traitement permettant l'extraction simultanée du flux et du tissue par oscillations transverses avec un estimateur de mouvement 2D et valider cliniquement la technique.

Chapitre 3

Ce troisième chapitre décrit : la méthode d'estimation 2D de mouvement dites par "oscillations transverses", la chaîne de traitement, les validations *in vitro* avant de conclure sur les limites de la validation *in vitro* et les difficultés *in vivo*. Nous avons présenté l'avancement de nos travaux dans ce domaine par trois actes publiés dans *IEEE International Ultrasonics Symposium* : "Estimation of arterial wall motion using ultrafast imaging and transverse oscillations: in vivo study" (2016), "Simultaneous pulse wave and flow estimation at high-framerate using plane wave and transverse oscillation on carotid phantom" (2017), et "Simultaneous tissue and flow estimation at high frame rate using plane wave and transverse oscillation on in vivo carotid" (2018).

La méthode des oscillations transverses consiste à introduire virtuellement une oscillation latérale dans les images ultrasonores afin de pouvoir estimer une phase 2D là où, naturellement, une oscillation existe uniquement dans la direction de propagation des ultrasons. Sous l'hypothèse d'être suffisamment loin de la sonde et que l'onde soit monochromatique, la réponse impulsionnelle latérale du système d'imagerie est la transformée de Fourier de l'ouverture active. Par conséquent, une oscillation latérale peut être introduite avec une pondération spécifique sur les éléments de la sonde. Une solution consiste à pondérer les éléments (émission ou réception) avec une fonction double Gaussienne sur les éléments créant une oscillation latérale dans le milieu. Une autre approche, adoptée dans la thèse, consiste à effectuer la transformée de Fourier 2D de l'image et à isoler, avec un masque Gaussien, des fréquences latérales spécifiques. Ensuite, un estimateur de phase 2D est décrit, les oscillations 2D sont séparées (dans le domaine de Fourier) en deux signaux analytiques avec une oscillation purement 1D. La variation de phase de chacun de ces signaux est estimée en utilisant l'autocorrélation complexe des signaux ; cette approche est similaire aux techniques Doppler 1D déjà existantes. Puis, ces deux informations 1D sont recombinées pour obtenir le déplacement 2D du milieu. L'estimateur fonctionne donc principalement dans le domaine de Fourier, les paramètres d'estimation sont facilement flexibles dans le domaine fréquentiel et l'approche est peu couteuse en temps et puissance de calcul.

La chaîne de traitement mise en place se décompose en quatre étapes : formation des images ultrasonores, estimation du mouvement tissulaire, rehaussement du signal du sang et estimation du flux vectoriel. Le rehaussement du signal du sang par le filtre de paroi est abordé en détail dans le quatrième chapitre comme contribution à part entière avec une approche adaptative basée sur l'estimation du mouvement tissulaire. Une fois les déplacements estimés obtenues, les vitesses caractéristiques du flux et du tissu sont extraites et des mesures avancées telles que la vitesse de l'onde de pouls et les contraintes de cisaillement sont effectuées comme potentiels marqueurs des pathologies vasculaires.

La validation expérimentale a été effectuée sur deux fantômes. Un premier fantôme commercial de flux a permis de valider l'estimation des vitesses du flux dans différents régimes de vitesses avec une bonne reproductibilité et des erreurs typiquement inférieures à 10% sur la magnitude et moins de 10 degrés d'erreurs sur les angles estimés. Un second montage, reproduisant une artère, a été développé pour l'expérience. Ce montage permet d'avoir différentes élasticités de tissu qui ont été quantifiées grâce à la vitesse de l'onde de pouls. Une bonne reproductibilité a été observée avec des observations de vitesses d'ondes de pouls suivant la loi d'évolution attendues.

En conclusion de ce chapitre, une méthode d'introduction de phase 2D flexible et rapide a été validée *in vitro* avec un estimateur de mouvement 2D. Cette validation a été effectuée sur un fantôme commercial pour le flux et sur un montage créé pour l'expérience pour le mouvement tissulaire, via la mesure de l'onde de pouls.

Chapitre 4

Ce quatrième chapitre décrit : la notion de filtrage de paroi, le filtrage de paroi adaptatif basé sur les vitesses tissulaires, les expériences *in vivo* validation de cette nouvelle approche contre des méthodes plus conventionnelles et l'intérêt de cette approche pour la clinique. Nous avons présenté l'avancement de nos travaux dans ce domaine par deux actes publiés dans *IEEE International Ultrasonics Symposium* : "Spatial and temporal adaptive FIR clutter filtering" (2018), and "Comparison of adaptive clutter filters for vector velocity estimation: realistic simulations and in vivo examples" (2019). La contribution présentée dans ce chapitre a été en partie effectuée durant un séjour doctoral de six semaines au département de circulation d'imagerie médicale de l'université norvégienne de sciences et de technologie à Trondheim en Norvège.

Le filtrage de paroi consiste à rehausser le signal du sang par rapport aux tissus environnants. En effet, la puissance du signal venant du sang est inférieure d'environ 40 dB au signal tissulaire. Supposant que le tissu se déplace lentement par rapport au sang, il est possible de filtrer les composantes fréquentielles basse fréquence au cours du temps par filtrage fréquentiel. Une approche similaire consiste à effectuer une régression polynomiale d'un ordre relativement faible sur les signaux au cours des tirs. Une approche plus récente, consiste à effectuer la décomposition en valeurs singulières et à supprimer les valeurs propres ayant le plus d'énergie qui doit correspondre au signal du tissu.

Cependant, la paroi peut être sujette à de fortes vitesses tissulaires au cours du cycle cardiaque qui crée un recouvrement entre les vitesses tissulaires et celles du sang. Un filtrage adaptatif est proposé ici où, le filtre de paroi, est réglé sur la vitesse tissulaire estimée avec une fréquence de coupure qui est modifiée au cours du temps. Cette fréquence de coupure adaptative permet d'atténuer au plus juste les vitesses tissulaires dans chaque phase du cycle cardiaque, en perdant le moins de signal possible du sang. Une seconde approche prend en compte la réponse impulsionnelle du système d'imagerie pour connaitre quelles sont les vitesses tissulaires qui ont pu contribuer en chaque point du lumen. Cette approche, bien que plus couteuse, permet d'avoir une fréquence de coupure adaptative en temps et en espace.

Ces deux approches adaptatives ont été comparées avec des méthodes de filtrage de paroi plus classiques, y compris la décomposition en valeurs singulières. Elles ont permis, sur volontaires sains, d'extraire des profils de vitesse plus proches des parois des vaisseaux que les méthodes conventionnelles. De plus, les fréquences de coupure sont directement liées aux vitesses tissulaires ce qui réduit le nombre de paramètres ajustables.

En conclusion de ce chapitre, deux approches de filtres de paroi ont été développées et appliquées sur des carotides *in vivo* de volontaires sains. Ces approches, basées sur les vitesses tissulaires, permettentde rejeter au plus juste le signal du tissu. Elle permet même d'obtenir des résultats d'un meilleur rendu que des filtrages plus conventionnels et que des approches par décomposition en valeurs singulières. Appliqués en clinique, de tels filtres pourraient conduire à une estimation plus précise dans les cas pathologiques avec des plaques, ou d'autres maladies qui conduisent à un mouvement anormal de la paroi avec de grandes variations de vitesses au cours du cycle cardiaque.

Chapitre 5

Ce cinquième chapitre décrit : la méthode et le matériel, les résultats d'une étude clinique et ses limites et perspectives. Nous avons soumis un article dans *Physics in Medicine & Biology* :“Simultaneous vectorial blood flow and wall motion imaging in the carotid artery: a clinical proof of concept” (2019). L'étude clinique été conduite à l'hôpital St. Olavs pendant un séjour doctoral de deux mois au département de circulation d'imagerie médicale de l'université norvégienne de sciences et de technologie à Trondheim en Norvège.

Un total de treize patients a accepté de participer à cette étude et chacune de leurs carotides ont été acquises après un examen de routine clinique prévu, dans les mêmes conditions que celle de l'examen clinique, mais à l'aide d'un système de recherche. L'examen a permis de déterminer si chaque carotide pouvait être classée comme pathologique ou non. Un second groupe de douze volontaires sains a participé aux examens. Un jeu de données additionnel d'une sténose de carotide interne a aussi été acquis sur un des patients. La chaîne de traitement présenté dans le chapitre précédent a été utilisée avec le filtre de paroi adaptatif en temps pour réduire la charge de calcul. Basé sur ces estimés, un ensemble de marqueurs potentiels a été extraits dont la vitesse de l'onde de pouls et le cisaillement le long de la paroi.

Les résultats ont montré que la technique permet l'extraction du mouvement de la paroi et du flux vectoriel pour 90% des patients et pour la totalité des volontaires sains. L'inspection qualitative du flux rend compte d'un profil parabolique et un mouvement uniforme dans la paroi chez les volontaires. Chez les patients, les cartes de vitesse montrent des écoulements plus complexes, des tourbillons dans le flux et des déplacements non uniformes de la paroi. La sténose présente également une accélération du flux et un fort cisaillement sur la partie haute de l'artère. En fonction des paramètres et marqueurs mesurés, les groupes peuvent être séparés.

En conclusion de ce chapitre, une étude clinique a été conduite sur une cohorte de patients et de volontaires sains. La faisabilité d'une mesure simultanée de la paroi des vaisseaux et de la vitesse du flux sanguin a été validée dans un contexte clinique à une cadence d'imagerie élevée de 6 000 images par seconde. En effet, le flux et le mouvement de la paroi ont été extraits pour tous les volontaires. Pour les patients, la faisabilité est d'environ 90%, 10% des carotides étaient hors du champ de vue ou les images étaient d'une qualité trop faible pour traitement. Le flux vectoriel permet d'analyser avec plus de précision le flux par rapport à l'imagerie Doppler conventionnelle où une seule composante de la vitesse peut être extraite à faible cadence d'imagerie. Cette technique pourrait être utilisée pour détecter les mouvements inhabituels de la paroi. En effet, la méthode a permis de mettre en évidence des parties de la paroi artérielle avec un mouvement non homogène. Des mesures dérivées de la vitesse ont pu être extraites avec succès à la fois chez des volontaires sains et dans une population pertinente de patients, y compris des géométries complexes avec sténoses et remodelage artériel.

Conclusion

Le but de cette thèse était de développer une séquence d'imagerie ultrasonore ultra-rapide permettant d'extraire simultanément les vitesses du flux et de la paroi avec des marqueurs pathologiques vasculaires en clinique. Pour cela, une méthode d'imagerie simultanée du mouvement tissulaire et du flux vectoriel a été développée et validée. La validation a été effectuée sur un fantôme *in vitro* et un fantôme spécialement développé pour le projet. Au cours de la validation, les estimations étaient précises et cohérentes, avec de faibles écarts-types et erreurs dans les estimations. Ces erreurs sont de moins de 10% sur les magnitudes des vitesses, moins de 10 degrés d'erreurs sur les angles estimés et les mesures d'évolution de l'élasticité des tissus correspondent à la loi théorique. Après validation de la technique, des approches adaptatives pour le filtrage de paroi ont été développés puis validés sur volontaires sains. Ces approches adaptatives ont été comparées aux techniques classiques et ont montré un meilleur flux estimé surtout près de la paroi et pendant la diastole. La preuve de concept clinique a également été concluant avec une extraction de marqueurs sur 90% des données de patients. La plupart des patients ont un schéma d'écoulement et de mouvement tissulaire plus complexe que les volontaires. De plus, les patients ont montré des différences significatives par rapport aux volontaires pour plusieurs marqueurs pathologiques. Compte tenu de ces résultats et de ces développements, la séquence ultrasonore permettant l'extraction simultanée du flux, des vitesses tissulaires et des marqueurs pathologiques est entièrement développée et validée. Cette séquence avec sa technique d'estimation de mouvement peut donc passer à une étude plus poussée afin de quantifier son apport dans la caractérisation de pathologies précises avec un recrutement plus stricte des type de pathologies.

Comme tout travail de recherche, cette thèse a certaines limites et certains points qui pourraient être développés d'avantage. Tout d'abord, au cours de ces travaux, seule la technique des oscillations transverses a été utilisée et aucune comparaison avec d'autres techniques d'estimation n'a été effectuée. Le choix de la technique des oscillations transverses a été guidé par les travaux antérieurs du laboratoire et par le fait que la méthode avait déjà été validée séparément pour une utilisation sur le tissu et le flux. De plus, cette approche semblait relativement peu coûteuse et simple par rapport à d'autres de la littérature. Cependant, cela ne veut pas dire que d'autres méthodes ne pourraient pas avoir des résultats similaires ou même meilleurs. La validation a été effectuée sur deux fantômes différents pour l'estimation du mouvement tissulaire et du flux sans simulation préalable. Il s'agit d'un problème de modélisation, les interactions flux/paroi sont complexes et aucune méthode ne semblait être disponible. En ce qui concerne les fantômes, aucun appareil sur le marché ne répondait à nos attentes pour valider les deux aspects, deux fantômes ont donc été utilisés pour chaque aspect. Lors des acquisitions *in vivo*, pour le filtrage de paroi et la preuve de concept clinique, le nombre de volontaires et de patients était relativement faible, ce qui rend difficile l'extraction de valeurs statistiques solides avec une bonne confiance. En effet, il est difficile d'obtenir, surtout dans un environnement clinique, autant de volontaires/patients que souhaité dans un temps imparti relativement faible. Une autre limite est l'incohérence dans le placement ou le mauvais placement de la sonde lors des acquisitions en clinique ; il s'agit d'un problème existant même pour un praticien formé ou un cardiologue. A ce jour, il n'existe pas de solution miracle à ce problème, d'autant plus que les patients peuvent avoir des difficultés à rester immobiles lors des acquisitions.

Les perspectives comprennent une étude plus approfondie qui pourrait pleinement être qualifiée d'étude clinique avec un grand nombre de patients. Couplé à des tests statistiques, cela permettrait de mesurer avec précision l'intérêt et la contribution de la méthode pour la détection des pathologies. De plus, l'adaptation de la méthode à une autre géométrie de sonde est un travail futur important. Si elle est utilisée avec des sondes sectorielles, il sera possible d'utiliser la technique dans l'aorte abdominale pour une application potentielle sur les anévrismes qui se développent fréquemment dans cette artère. Une perspective à plus long terme est l'utilisation de la technique avec une sonde matricielle permettant de se débarrasser des problèmes de placement et d'acquisition hors plan grâce à la 3D. Une dernière perspective sur laquelle de nombreux groupes travaillent est l'amélioration de la qualité de l'image sans compromettre la cadence d'imagerie. En effet, en raison de l'utilisation d'ondes planes, la qualité de l'image reste limitée par rapport aux modes d'échographie focalisée qui sont disponibles sur les systèmes cliniques.